Indirect Search for Dark Matter with the ANTARES Telescope

M. C. Charif

CPPM-T-2012-004

UNIVERSITÉ DE LA MÉDITERRANÉE
AIX-MARSEILLE II
FACULTÉ DES SCIENCES DE LUMINY
163 avenue de Luminy
13288 MARSEILLE Cedex 09

THÈSE DE DOCTORAT

Spécialité : *Physique et Sciences de la Matière*

Mention : *Physique des Particules et Astroparticules*

présentée par

Mohamad-Ziad Charif

en vue d'obtenir le grade de docteur de l'Université de la Méditerranée

Indirect Search for Dark Matter with the ANTARES Telescope

Soutenue le 27 Septembre 2012 devant le jury composé de

Dr.	Eric Kajfasz	President de Jury
Prof.	Lee Thompson	Rapporteur
Dr.	Carlos Pérez De Los Heros	Rapporteur
Dr.	Vincent Bertin	Directeur de thèse
Dr.	Paschal Coyle	Directeur de thèse
Prof.	Antonio Capone	Examinateur
Prof.	Pascal Gay	Examinateur
Dr.	Emmanuel Nezri	Examinateur

Région
Provence-Alpes-Côte d'Azur

"The most exciting phrase to hear in science, the one that heralds new discoveries, is not ‘Eureka‘ but ‘That’s funny...‘ "- Isaac Asimov (1920 - 1992)

Contents

Chapter 1

Introduction

The early history of modern physics have been full of problems fixed with unorthodox yet brilliant solutions. From the Hydrogen electron orbit, black body radiation and the ultraviolet catastrophe, to the perihelion precession of Mercury. Quantum Mechanics and General Relativity not only solved these problems but they opened the path to new observations and predictions about the Universe we live in and the introduction of new problems to be solved.
One of the more modern problems we are facing today in physics is the large discrepancy among measurements of the visible mass in the Universe and the predictions of laws of gravity. An indisputable mass of evidence from different parts of observational cosmology is showing again and again that the observed luminous mass in the Universe constitutes a tiny fraction of the matter that actually exists. The proposed solutions of this problem comes in two completely different flavors. One proposed solution is that the laws of gravity are not the same in the limit of tiny accelerations. Theories of modified gravitational dynamics propose a non-linear term in Newton law of gravity that becomes relevant at small accelerations which in turn can explains the missing matter. The other solution to the missing matter is the introduction of new type of matter that does not interact with light, making it invisible yet inferred to exist by its gravitational effect. The new matter becomes a new elementary particle to be added to list of already known elementary particles. While there are many candidates to this new elementary particle the favored one is called a WIMP or Weakly Interacting Massive Particle. This WIMP can also naturally arise in many extensions to the Standard Model of particle physics making a very attractive subject of study. One of these extensions which will be covered in this thesis is Supersymmetry.
The detection of WIMPs can be done via several ways, from direct detection by collisions with nucleons in detectors, to indirect detections via annihilation of WIMPS in the Universe. One attractive method of detecting them is when they accumulate in the Sun and annihilate producing neutrinos. These neutrinos can

then be detected with Neutrino telescopes like ANTARES which is the topic of this thesis.

We will start in Chapter 2 with an introduction to the evidence of dark matter, then introduce Supersymmetry as a possible framework that incorporates a WIMP candidate. In addition, we will talk about direct and indirect detection of dark matter. Then we finish with describing how dark matter annihilation in the Sun can produce neutrinos which could be detected. Later in Chapter 3 we will introduce neutrino interactions with matter and how a neutrino can be detected in a Cherenkov detector, followed by a description of the ANTARES detector. In Chapter 4, a discussion on the data acquisition and simulation of ANTARES background is done. Then in Chapter 5 we will present an analysis of the 2007-2008 data accumulated by ANTARES for dark matter in the direction of the Sun and the limits obtained. Then in Chapter 6 we present sensitivties obtained with a new improved analysis method with more data (2007-2010) for dark matter in the direction of the Sun. Finally we end with Chapter 7 where we will present the conclusions.

Chapter 2

Dark Matter

In this chapter we will discuss the indirect evidence for dark matter, then move to the foundation of dark matter in theoretical physics and end with methods of detection.

2.1 Indirect evidence

The evidence of dark matter come generally from observational cosmology. Its existence is mainly inferred from the effect of its gravity on the surrounding visible matter (section 2.1.1) and from gravitational lensing (section 2.1.3). The existence of dark matter is required in order to account for discrepancies between calculations of the mass of galaxies and their visible mass as well as for galaxies clusters dynamics (sections 2.1.2 & 2.1.4).

2.1.1 Galactic rotation curves

One of the first indications on the existence of dark matter came from the study by Jan Hendrik Oort in 1932 on the velocity of stars in our solar neighborhood. The expected velocity of these stars was less than expected when based on the visible matter in the galaxy. Later in 1959 a study on the radial velocity of the spiral galaxy M33[1] showed that the rotation curve of the galaxy does not agree with the mass density of visible matter. Eleven years later in 1970, using more precise spectroscopy methods on the rotation of stars in Andromeda galaxy[2] it was shown that the rotation speed of the stars in spiral galaxies is roughly constant beyond the galactic bulge at the center instead of decreasing at large radius (figure 2.1), these results were replicated[3] few years later. Eventually a larger study on 21 spiral galaxies[4] showed that in order to explain the rotation curve of the stars the majority of the mass of the galaxy had to be in a form of an invisible matter

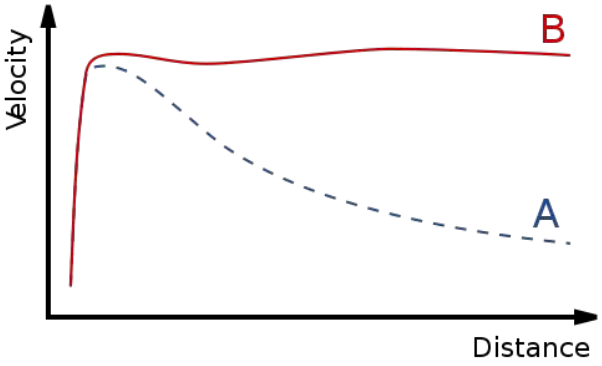

Figure 2.1: A comparison between of the rotation speed of stars for typical spiral galaxies (red curve) and what is expected from visible matter (blue curve).

in the galactic halo. Eventually more evidence started to pile up (figure 2.2) that supported the idea of the existence of a dark halo existing in galaxies.

2.1.2 Galaxy clusters

Galaxy clusters are the largest bounded structures in the known universe, they usually consists of a large number of galaxies (up to 1000) bound by their gravitational effect. The typical mass of these clusters is $10^{14}M_{\odot} \sim 10^{15}M_{\odot}$ where $M_{\odot}$ is the solar mass, and stretching from 2Mpc to 10Mpc (one parsec (pc) is about 3.10^{16}m or 3.2 light-years).
The study of galaxy clusters provides us with more proof on the existence of dark matter. Chandra X-ray Observatory study of the Abell 2029 cluster[6] showed that about $10^{14}M_{\odot}$ of the mass of the cluster is contained in a form of invisible matter exerting gravitational forces on the galaxies.

2.1.3 Gravitational lensing

Gravitational lensing is a phenomena where the light from a very distant souce is bent around a massive object (such as a black hole or a galaxy) between the source and the observer (figure 2.3). While this effect was first predicted in 1930's it was first observed in 1979 by studying the twin quasars[7] SBS 0957+561 A & SBS 0957+561 B.
The first evidence from gravitational lensing hinting at invisible mass came from the study of the galaxy cluster Abell 1689[8]. With the development of new detection techniques in gravitational lensing[9], stronger evidence for dark matter has been unveiled. In two studies[10, 11] of two galactic clusters merging while the

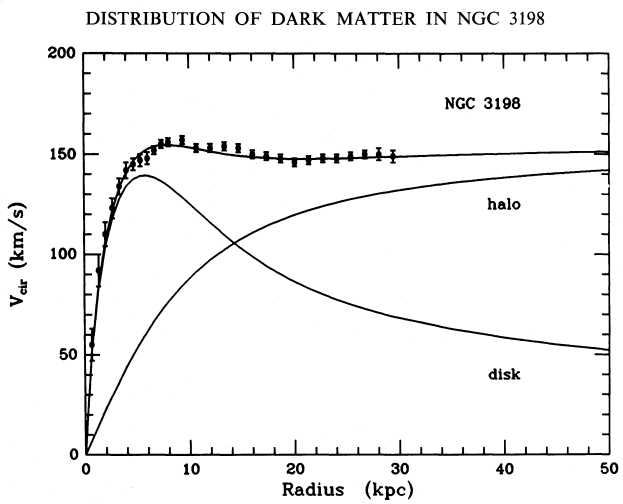

Figure 2.2: Comparison of the measured rotation curve of NGC-3198[5] as a function of the radial distance from its galactic center with the expected curve from visible matter, from a dark halo, and the sum of the two distributions.

baryonic matter still separated, it was shown that independently of any assumption on the laws of gravity that the gravitational potential of the cluster traced the overall shape of the merging clusters and not that of the baryonic component. This proved that the mass peak is not located with the baryonic mass but with a dark halo combining the two clusters. Additionally about 87.5% of the mass being invisible and the remaining 12.5% being baryonic. These two studies also heavily favors a particle component to dark matter as opposed to modified laws of gravity[12] as a solution to the missing mass.

2.1.4 Velocity Dispersions of galaxies & Mass to light ratio

The velocity dispersion σ, is the dispersion range(statistical) of velocities about the mean velocity for objects bound gravitationally such as stars in a galaxy or galaxies in a galaxies cluster. The mass to light ratio is the ratio between the mass of a specific volume and its luminosity denoted Υ. Υ is an extremely well known observable for objects such as stars and other astrophysical objects. One would expect when making measurements of entire galaxies to find a ratio that is the average of the ratio of the luminous objects located inside.
Measurements of velocity dispersion σ and Υ in spiral and elliptical galaxies[13] again showing a missing large mass component[13, 14]. These studies showed that the velocity dispersion can not be explained by means of the visible mass distribution found in galaxy clusters[14]. Thus indicating that more than 5 times

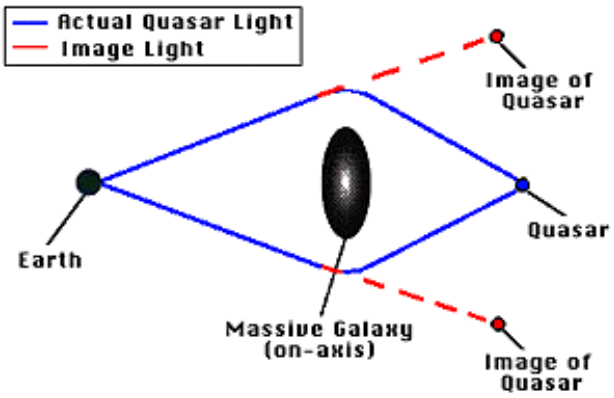

Figure 2.3: Diagram on the apparent and real path of light around a massive object.

that of the visible mass being located in a dark halo surrounding the clusters. Additionally the measurement of the mass to light ratio showed that the value is much larger than the average of the individual components indicating again that there is at least 3 times more invisible matter than visible.

2.1.5 Cosmic microwave background

The Cosmic Microwave Background (CMB) is thermal radiation ($\sim 2.725K$) that permeates with a high degree of uniformity the observable universe. The CMB was first theorized in 1948 as the thermal residual of the big bang and its detection was delayed until 1964. Since that several experiments were built to measure the CMB radiation such as COBE experiment[15], WMAP[16] (figure 2.4), and PLANCK[17].
While CMB is not in itself evidence for dark matter, it validates the ΛCDM model (section 2.1.6) which predicts the existence of dark matter. The model is further validated by other measurement such as the Baryon acoustic oscillations[18], distance measurements by type Ia supernovae[19], and the Lymann-alpha forest measurements[20] (Figure 2.5).

2.1.6 ΛCDM model

The ΛCDM model is referred to as the Standard Model of cosmology, the model is built on solutions to Einstein equation of General Relativity (eq 2.1)

$$R_{\mu\nu} - \frac{R}{2} g_{\mu\nu} - \Lambda g_{\mu\nu} = 8\pi T_{\mu\nu} \tag{2.1}$$

Where:

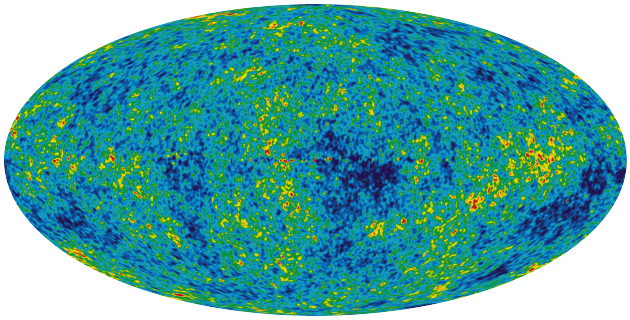

Figure 2.4: CMB anisotropy observed with WMAP spacecraft.

- $R_{\mu\nu}$ is the Ricci tensor.
- $g_{\mu\nu}$ is the metric tensor.
- $T_{\mu\nu}$ is the energy-momentum tensor.
- R is the Ricci scalar.
- Λ is the cosmological constant.

The theoretical foundation of the model comes from the Friedman-Lemaitre-Robertson-Walker metric which is an exact solution to equation 2.1 with the assumption that the universe is isotropic and homogeneous at the large scales which is heavily supported by observation of the Universe at the cosmological scale ($\sim$ 100Mpc). This metric can be written as following in equation 2.2.

$$-c^2 d\tau^2 = -c^2 dt^2 + a(t)^2 d\Sigma^2 \tag{2.2}$$

$$d\Sigma^2 = \frac{dr^2}{1-kr^2} + r^2 d\Omega^2 \tag{2.3}$$

$$d\Omega^2 = d\theta^2 + \sin^2(\theta) d\phi^2 \tag{2.4}$$

With $g_{\nu\mu} = diag(1, \frac{-a^2}{1-kr^2}, -a^2r^2, -a^2r^2sin^2(\theta))$ and $T_{\mu\nu} = diag(\rho_{tot}, p_{tot}g_{11}, p_{tot}g_{22}, p_{tot}g_{33})$. In addition the definition of the parameters are:

- k is the spatial curvature of space. It can take 3 values, +1 which corresponds to a closed universe -1 an open universe and 0 for a flat one.
- a(t) is the scale factor of the expansion of the universe as a function of time.
- ρ_{tot} is the total energy density of the Universe.
- p_{tot} is the pression of the Universe.

From these equations we can derive the Friedmann equation (eq 2.5 & 2.6) with $H(t) = \frac{\dot{a}(t)}{a(t)}$ and $\dot{\rho}_{tot}$ being the time derivative of ρ_{tot}.

$$H^2(t) = \frac{8\pi}{3}\rho_{tot} - \frac{k}{a^2} + \frac{\Lambda}{3} \quad (2.5)$$

$$\dot{\rho}_{tot} = -3H(\rho_{tot} + p_{tot}) \quad (2.6)$$

The Friedman equation can sometimes be written in the following form in equation 2.7 as function of the normalized densities of all ingredients of the universe, where Ω_R is the density of radiation in the universe, Ω_M is the density of all types of matter, Ω_K is the curvature of space. At our time now (a=1) the equation is reduced to 2.8.
Ω_M can also be written as the sum of $\Omega_c + \Omega_b$, where Ω_c is the density of dark matter and Ω_b as the density of baryonic matter.

$$\frac{H^2}{H_0^2} = \Omega_R a^{-4} + \Omega_M a^{-3} + \Omega_k a^{-2} + \Omega_\Lambda \quad (2.7)$$

$$1 = \Omega_R + \Omega_M + \Omega_k + \Omega_\Lambda \quad (2.8)$$

The best measured value for these parameters above come from the combination of WMAP survey[21], baryon acoustic oscillations[18].$\Omega_b = 0.0456 \pm 0.00015$ (fig 2.5) the density of baryonic matter which is in agreement with predictions from primordial nucleosynthesis[22], $\Omega_c = 0.227 \pm 0.014$ the density of dark matter, $\Omega_\Lambda = 0.728^{+0.015}_{-0.016}$ the cosmological constant (fig 2.5) , $\Omega_R = 4.97 \cdot 10^{-5}$ the density of radiation. The results indicate that we have about 50 times more dark matter in the Universe than baryonic matter (consistent with observations).

2.1.6.1 Dark matter in ΛCDM

Dark matter can either be explained as actual matter (baryonic or not) or as laws of gravity being different at the large scales[12] such as the MOND (MOdified Newtonian Dynamcics) model. With major models for modified laws of gravity being disfavored in face of matter models [10, 11], the remaining part is to see whether this matter is baryonic or not. The major candidate for baryonic dark matter is MACHOs or Massive Compact Halo Objects. MACHOs mainly consists of large and condensed objected such black holes, neutron stars, and other that have from barely to non-existing electromagnetic signatures. The contribution of these objects has already been constrained and ruled out as a dark matter candidate[23, 24, 25].
What remains are the non-baryonic candidates, which can be divided into three categories:

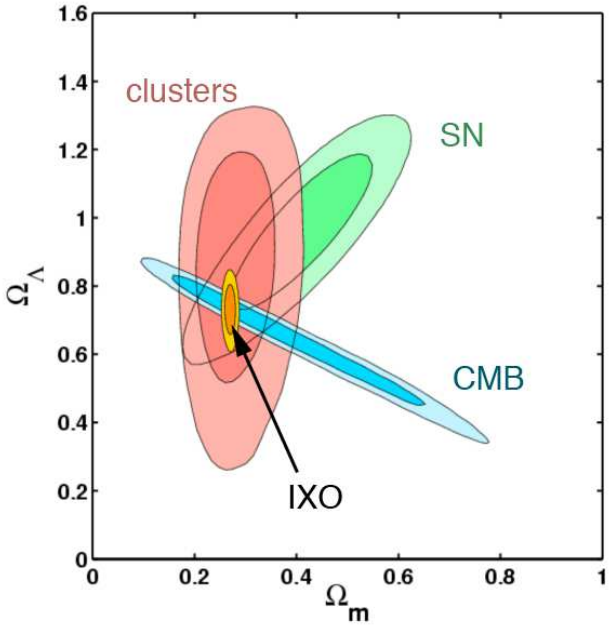

Figure 2.5: Combination of the WMAP, type Ia supernova, X-ray band, and cluster measurement for Ω_Λ and Ω_m.

- Hot dark matter, which has relativistic velocities. One candidate for hot dark matter are neutrinos. However, neutrinos are already disfavored as a candidate[21] as their contribution to the matter density is bound to be $\Omega_{neutrino} < 0.014$ much smaller than the expected density of matter in the Universe. In addition simulations of the large scale structures formation of the universe does not favor hot dark matter[26].

- Warm dark matter, with the mass being from 300 eV to 3000 eV. However, with extensive searches in colliders (proton and electron) no particle has ever been found in this mass range. Main candidate for warm dark matter is a sterile neutrino.

- Cold dark matter, which has non-relativistic velocities (< 1000 km/s) is favored by simulations of the large scale structures formation of the universe[26]. The lower bound mass of cold dark matter is above 1 GeV. The main candidates for CDM are the WIMP or Weakly Interacting Massive Particle, and axions which are theoretical solutions to the strong CP problem in QCD.

The most favored model of dark matter is the Weakly Interacting Massive Particle, which we will discuss in the next section.

2.2 WIMPs

2.2.1 Standard Scenario

The standard view of WIMPs is that it is an electrically neutral particle that its existence can not be inferred by direct electromagnetic radiations, and since we already established it can not be a baryonic then it should be colorless (no strong interaction). In addition, this particle has to be stable or at least if it is not then its half-life should be extremely long (at least the current age of the Universe). Unfortunately these characteristics do not apply to any known particle in the Standard Model of particle physics. Several extensions of this model offer candidates to WIMPs such as the lightest SuperSymmetric particle (LSP) in Supersymmetry (section 2.2.2), in addition to the lightest Kaluza-Klein particle (LKP) in Universal Extra Dimension[27, 28] models.
The main attraction for WIMPs as a candidate for cold dark matter comes from the fact that if we try to calculate the WIMPs annihilation cross-section in order to get the same order of magnitude of the density we have now $\Omega_c(t_0) = 0.227$ we would get a cross section similar to that of the weak force (eq 2.9), the order of magnitude of a weak cross-section $10^{-9}GeV^{-2}$ ($\sim (\frac{g}{M_W})^4$) where g coupling constant of the weak interaction and M_W is the W boson mass. M_{WIMP} is the mass of the WIMP, $N_{WIMP}(t_0)$ is the number of WIMP particles at the present time.

$$\Omega_{WIMP}(t_0) = \frac{M_{WIMP}.N_{WIMP}(t_0)}{\rho_c(t_o)} \tag{2.9}$$

$$\simeq \frac{10^{-10}GeV^{-2}}{<\sigma v>} \tag{2.10}$$

Equation 2.9 is obtained by first deriving the number of WIMP particles as a function of time. Standard scenario of WIMPs puts them in thermal equilibrium with other particles, after their creation in the early Universe. After the Universe cools down by expanding, the temperature drops below the WIMP mass halting their creation and resulting in an rapid decrease of their abundance. Eventually the thermal equilibrium of WIMPs can not be maintained as the expansion of the Universe reaches a point where it is larger than the WIMP rate of annihilation, consequently this results in a relic WIMP density that can account for the value we have now. This evolution can be described using Boltzmann equation shown in equation 2.11, where H is the Hubble parameter, N_{WIMP} is the number of WIMPs as a function of time and N^{eq}_{WIMP} is the number of WIMPs at thermal equilibrium, and $<\sigma v>$ is the thermally averaged annihilation cross-section of WIMPs multiplied by its velocity.

$$\frac{dN_{WIMP}}{dt} + 3H.N_{WIMP} = <\sigma v>[(N^{eq}_{WIMP})^2 - N^2_{WIMP}] \tag{2.11}$$

The number of WIMPs at thermal equilibrium N^{eq}_{WIMP} is derived using Maxwell-Boltzmann statistics in equations 2.12 (for $T \ll M_{WIMP}$) & 2.13 (for $T \gg M_{WIMP}$). E_{WIMP} is the energy of the WIMP particle, p_{WIMP} its momentum, and M_{WIMP} its mass.

$$N^{eq}_{WIMP} \propto \int (M_{WIMP}.T)^{\frac{3}{2}}.e^{\frac{-M_{WIMP}}{T}}.\frac{e^{\frac{-E_{WIMP}}{T}}}{(2.\pi)^3}\frac{d^3p_{WIMP}}{(2.\pi)^3} \tag{2.12}$$

$$N^{eq}_{WIMP} \propto \int T^3.\frac{e^{\frac{-E_{WIMP}}{T}}}{(2.\pi)^3}\frac{d^3p_{WIMP}}{(2.\pi)^3} \tag{2.13}$$

Moreover, it is interesting to write the equation 2.11 as function of the WIMP density co-moving with the expansion of the Universe. The new definition becomes $\bar{N}_{WIMP} = N_{WIMP} \cdot a^3$, additionally if we define the time variable as $x = \frac{M_{WIMP}}{T}$ which is allowed by the fact that during era dominated by radiation the temperature is related to the age of the Universe $T \propto t^{-\frac{1}{2}}$. Figure 2.6 shows us when the annihilation cross-section increases then the WIMP number density follows the equilibrium value for a longer time leading to lower relic density after decoupling.

Going back to equation 2.9, it would seem that the standard scenario of WIMPs predicts the particle to interact via the weak force in addition to gravity.

2.2.2 WIMPs in Supersymmetry

Symmetries are the fundamental feature of particle physics. Two types of symmetries govern our Universe, global symmetries govern the behavior we observe in nature while local symmetries govern the interaction between the different constituents of matter. In quantum mechanics local symmetries (or gauge) facilitate the study of field theories and their different behavior. In this regard Supersymmetry unifies space-time symmetries with local ones, or more precisely bosons with fermions. In essence, Supersymmetry links each known boson to a fermionic super-partner and vice-versa to each fermion that exists in the Standard Model of particle physics.

To this moment there is no experimental evidence that establishes Supersymmetry as a theory of nature. In addition to the attraction of Supersymmetry on the theoretical level, the theory can solve many problems with the Standard Model of particle physics. One of these problems is the hierarchy problem, in field theory scalar particles (like the Higgs) have their mass unprotected from quantum effects, so even if the particle have a small mass to begin with, due to loop corrections the mass can grow as high as the energy cut-off scale of the theory. Supersymmetry solves this problem by linking the loop corrections to its super-particle which cancel out and eliminates the divergence.

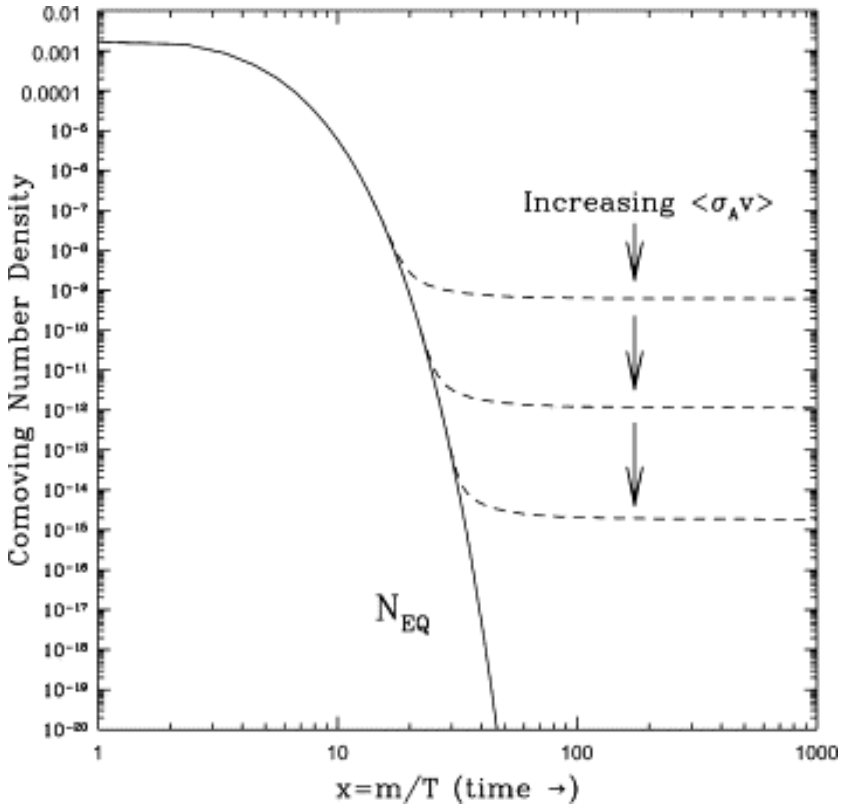

Figure 2.6: Temporal evolution of the co-moving WIMP number density.

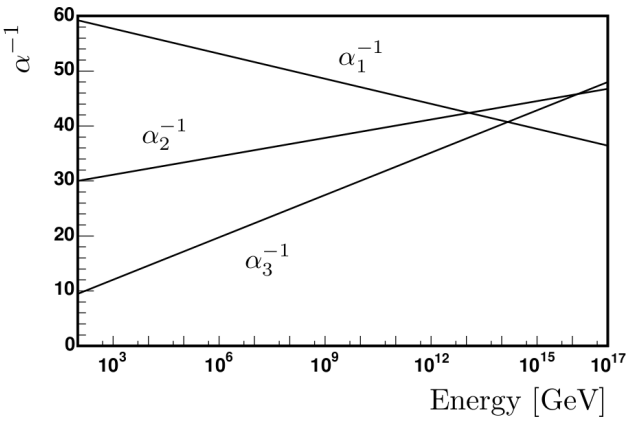

Figure 2.7: Energy dependence of the inverse coupling coefficient of the three forces (strong, weak, and electromagnetic) in Standard Model of particle physics[29].

Another problem solved by Supersymmetry is the unification of the forces: strong, weak, and electromagnetic. The energy dependence of the couplings coefficients as it is now in the Standard Model does not converge when interpolated into higher energies (figure 2.7). In the framework of Supersymmetry they seem to converge around the energy scale of $10^{16} GeV$ (figure 2.8). This is also called the Grand Unification Theory scale (GUT).

Finally, one other problem solved by Supersymmetry is the candidate for the WIMP dark matter particle. We can define in Supersymmetry a new quantum number that we refer to as R-parity, which is defined as $R = (-1)^{2S+3(B-L)}$, where S is the spin, B is the baryon number and L is the lepton number. All particles of the Standard Model are R-even (R=1), while their super-partners would be R-odd (R=-1). If this quantum number is conserved then when a super-particle is decaying there is always a super-particle in the decay product, effectively making the lightest super-partner (LSP) a stable particle. If this particle is as well neutral and colorless then by definition it is a dark matter candidate. In most of the parameter space of the Minimal Supersymmetric extension of the Standard Model (MSSM), the LSP is a neutralino, the super-partner of the neutral Higgs and gauge bosons.

2.2.2.1 MSSM

The MSSM[30] is the Minimal Supe rsymmetric extension of the Standard Model with the energy scale of this theory being the weak scale. This model contains the minimal number of supermultiplets needed to fully explain the interactions in the Standard Model. Additionally if we assume we have only one Higgs field than we would get a single Higgsino (superpartner of the Higgs) which would lead

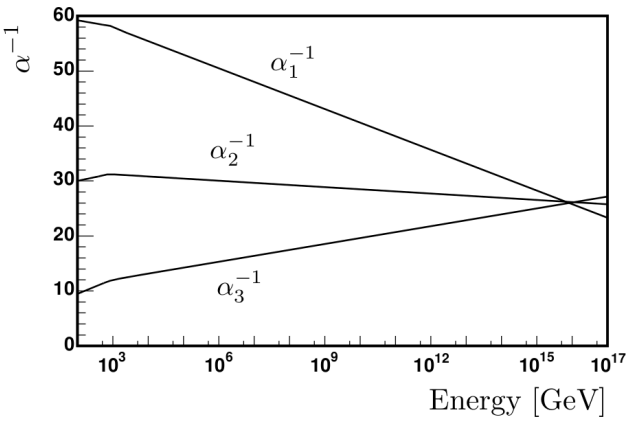

Figure 2.8: Energy dependence of the inverse coupling coefficient of the three forces (strong, weak, and electromagnetic) in Supersymmetry[29].

to a gauge anomaly and would cause the theory to be inconsistent. However, if one more Higgsino is added, then there is no gauge anomaly, making the simplest theory is the one with two Higgsinos and therefore two scalar Higgs doublets. Additionally, this predicts that the lightest neutral Higgs to be lighter than 130 GeV. The Higgs particle candidate found at LHC[31] (mass $\sim$ 125 GeV) is in agreement with the prediction made in MSSM. However, working with MSSM is quite difficult as the theory has more than 100 free parameters (by contrast Standard Model have less than 20), making any prediction hindered by the large amount of simulation needed to search all of the parameter space. In response to this problem a set of assumption have been made in order to constrain the parameters. CMSSM or Constrained MSSM is one of these models that contain certain assumptions. These assumptions are as follows:

- Universality of gaugino masses at the GUT scale.
- Universality of scalar masses ot the GUT scale.
- Universality of the tri-linear scalar (Yukawa) couplings at the GUT scale.
- Symmetry breaking by means of Electro-Weak Symmetry Breaking driven by the renormalization group drives the mass of the H_u^0 to negative values (or at least extremely small when compared to H_d^0)

These assumptions lead us to a model where we only have 4(+1) parameters:

- Gaugino masses at the GUT : $m_{1/2}$
- Scalar masses at the GUT: m_0

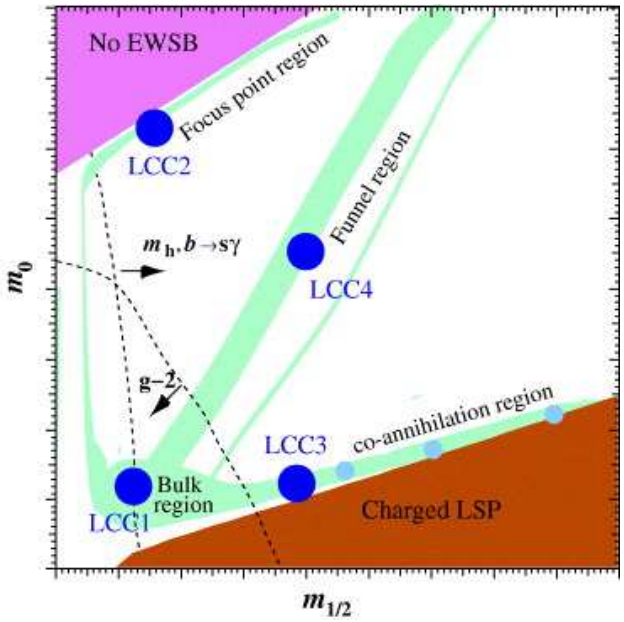

Figure 2.9: Parameter space of $m_{1/2}$ and m_0 plane with constrains on the LSP. Green region is where the predicted Ω_c is in agreement with WMAP.

- Tri-linear scalar couplings on the GUT scale: A_0
- The ratio of the vacuum expectation values of the neutral components of the two Higgs doublets $\langle H_u^0 \rangle$ and $\langle H_d^0 \rangle$ at the electro-weak scale: $\tan(\beta) = \frac{v2}{v1}$
- Sign of the higgsino mass parameter μ (+1 or -1)

Having four parameters (plus sign(μ)) is much easier to deal with, and constraining models is something now extremely easy to do.
The lightest supersymmetric particle in this model is usually the lightest of the neutralinos which are a mixing of the four superpatners ($\tilde{B}$, $\tilde{W}_3$, $\tilde{H}_u^0$ and $\tilde{H}_d^0$) of the neutral gauge bosons and higgs of the electro-weak section of Standard Model (B, W_3, H_u^0 and H_d^0). The neutralinos are neutral and colorless making the lightest of them a natural candidate for WIMPs. Additionally, inspection of various regions of the parameters space showed that many regions of the space produce the correct relic density Ω_c as we can see in figure 2.9.
Finally it is important to note that while LHC is constraining the parameter space ($m_{\tilde{q},\tilde{g}} > 1TeV$), there have not been any constraining on the neutralino mass so far in addition to those from the LEP, leaving a reduced parameter space that is still valid for consideration. In addition, CMSSM is used as a general benchmark, so it will be used during this thesis as a benchmark scenario for WIMP studies as well.

2.3 Methods of detection

2.3.1 Direct detection

Direct detection of dark matter refers to the detection of dark matter via its scattering off nucleus in a detector, causing transfer of momentum to the target nucleus and forcing it to recoil. Direct detection experiments use different techniques for detection (scintillation, phonon, and ionization) depending on the material of the detector (Ge, Si, NaI, and Xenon). The physics in dark matter nucleus interaction involves elastic scattering on nucleus, this scattering can be axial-vector giving rise to spin-dependent scattering or scalar giving rise to spin-independent scattering. Experiments using heavy nuclei such as the Iodine, Germanium or Xenon like DAMA[32], Edelweiss[33], SuperCDMS[34], XENON[35], and others are more sensitive to scalar interactions and their limits are mainly constraining the spin-independent WIMP-nucleon cross-section. On the other hands experiments using light nuclei are more sensitive to spin-dependent such as COUPP[36], SIMPLE[37] and NAIAD[38].
The spin-independent scattering amplitude can be written as follows[39] in equation 2.14 and the cross-section in equation 2.15, where N denotes the nucleon type, λ_N is WIMP nuclei coupling, m_χ and M_N are the WIMP and nucleon mass respectively, A is the atomic mass and Z the atomic number.

$$|A^{SI}|^2 = 64(m_\chi M_N)^2(\lambda_p Z + \lambda_n(A-Z))^2 \tag{2.14}$$

$$\sigma^{SI} = \frac{4m_\chi^2 M_N^2}{\pi(m_\chi + M_N)^2}.(\lambda_p Z + \lambda_n(A-Z))^2 \tag{2.15}$$

The spin-dependent scattering amplitude and cross section can be written as follows[39] in equations 2.16 & 2.17, where J is the angular momentum of the nuclei, and S is the spin of the nuclei where it takes the value of 0 for nuclei that have an even number of protons and neutrons and 0.5 for all other.

$$|A^{SD}|^2 = 192(m_\chi M_N)^2 \tag{2.16}$$

$$\sigma^{SD} = \frac{16m_\chi^2 M_N^2}{\pi(m_\chi + M_N)^2}.\frac{J_A+1}{J_A}(\sum_{i=p,n}\varepsilon_i S_i^A)^2 \tag{2.17}$$

Findings in direct detection has yielded some results that might indicate the presence of a light dark matter particle. DAMA experiment claims the observation of a dark matter signal[40]. This signal corresponds to annual modulation in their data that is related to Earth's rotation around the Sun. However, while these results are with an extremely high statistical significance (above 6σ), these results are in

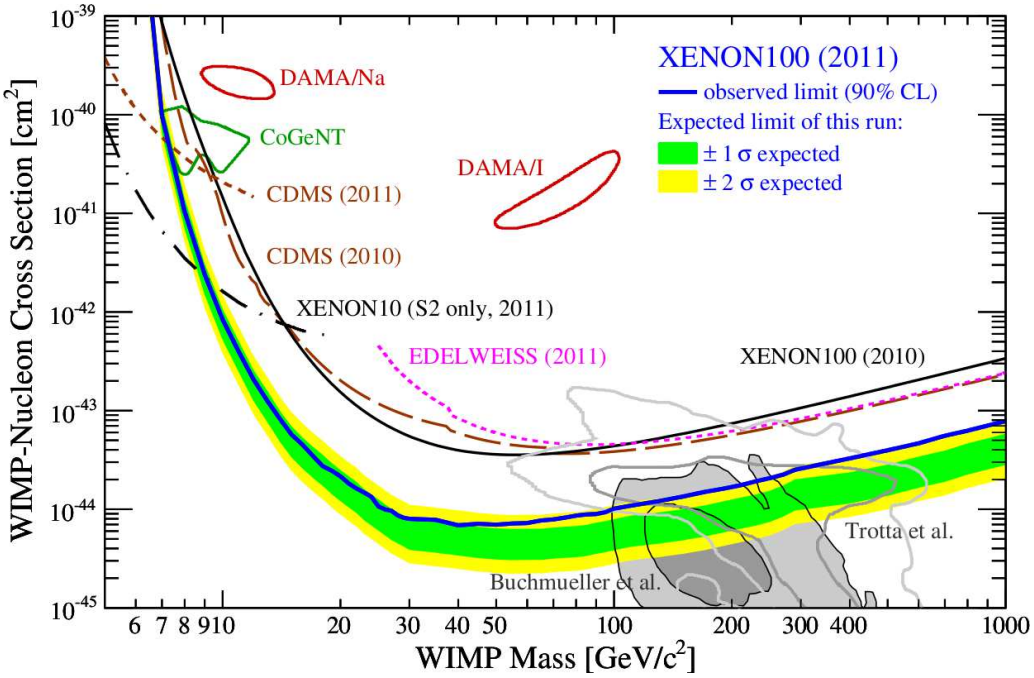

Figure 2.10: Limits on spin-independent elastic WIMP-nucleon cross-section σ as function of WIMP mass from XENON experiment[41].

conflict with limits set by other experiments such XENON[41] (figure 2.10) and COUPP[36] (figure 2.11) .

It is clear from equation 2.15 that the spin-independent cross-section is sensitive to mass of the nuclei while the spin-dependent does not have this feature. Figure 2.12 shows us the WIMPs-proton spin-independent cross-section [pb] as a function of the WIMP mass [GeV] in the CMSSM framework, and figure 2.13 the spin-dependent cross-section. As we saw in equation 2.15 we saw that spin-independent cross section is proportional to the atomic number and that the spin-dependent (eq 2.17) does not, and if we compare figures 2.12 and 2.13 we see that the spin-dependent is greater than independent. This is normal, as our neutralino is fermion with a spin, and spin-dependent cross-sections are always higher than independent cross-sections for fermions.

2.3.2 Indirect detection

The principle of indirect detection of dark matter is based on the idea that dark matter due to their gravitational effect can be trapped inside heavy objects, such as galaxies, galactic centers, and stars such as our own. Now as stated in the direct detection section, WIMPs can elastically scatter off nuclei. It is possible that even

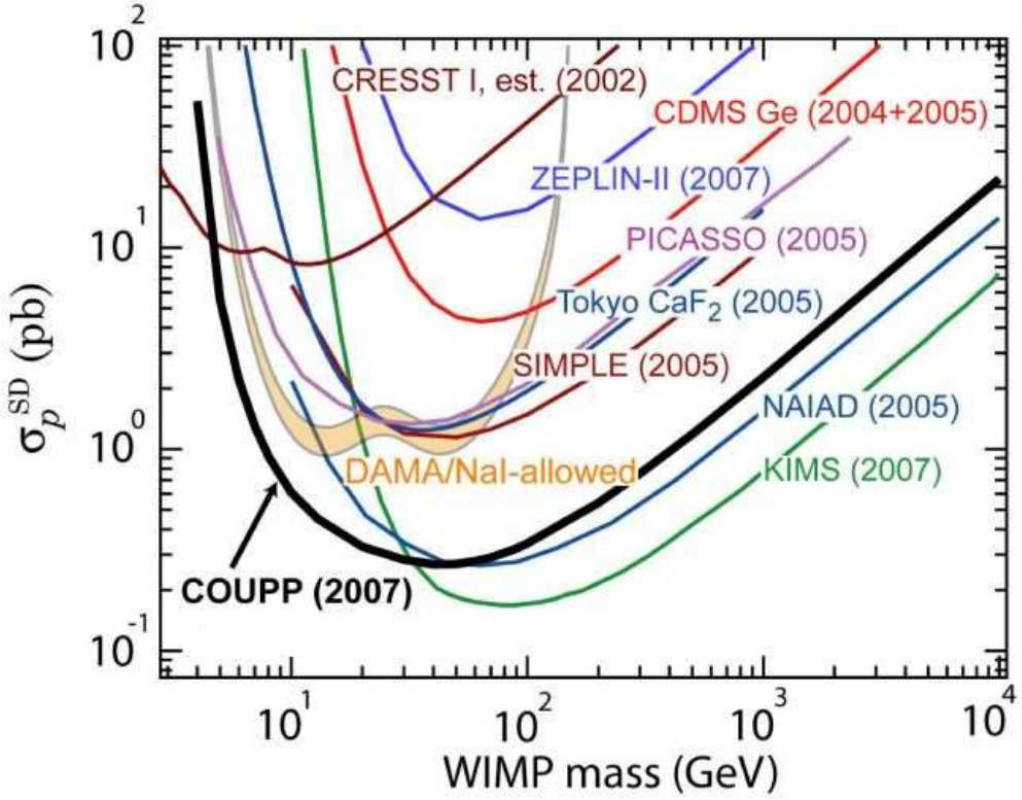

Figure 2.11: Limits on spin-dependent elastic WIMP-nucleon cross-section σ as function of WIMP mass from COUPP experiment[36].

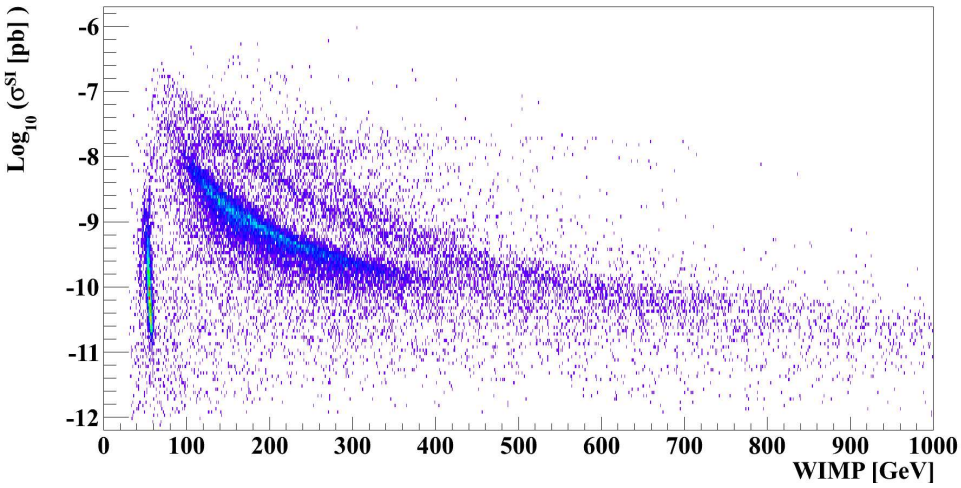

Figure 2.12: Log_{10} of the spin-independent cross-section of dark matter-proton as a function of WIMP mass. This simulation was done for CMSSM using SuperBayes[42, 43, 44, 45, 46, 47, 48, 48, 49, 50, 51, 52, 53]

.

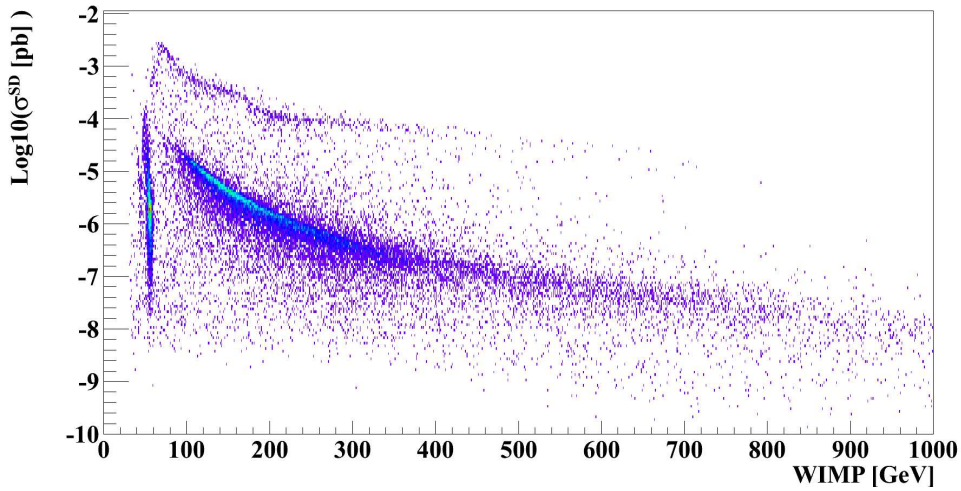

Figure 2.13: Log_{10} of the spin-dependent cross-section of dark matter-proton as a function of WIMP mass. This simulation was done for CMSSM using SuperBayes

.

if these WIMPS are not gravitationally bound by these objects, by scattering off the nuclei they can lose energy and speed. Now if this object has a large enough escape velocity these WIMPs can be trapped by this object. After being bound, the chance of auto-annihilation is increased (much higher local WIMPs density). This annihilation can produce the particles of the Standard Model (quarks, leptons and bosons). Some of the products of this annihilation are stable such as electrons, photons, protons and neutrinos. Others are not, and through their decay channels they will end up producing the aforementioned particles. So the focus of indirect detection is to measure fluxes of these particles as a signature of dark matter annihilating inside heavy celestial objects.
Experiments such as PAMELA[54], HEAT[55], AMS01[56], FERMI[57], and ATIC[58] have studied galactic positron fluxes, with varying results indicating an excess which could indicate the existence of dark matter if astrophysical sources are eliminated. Other experiments such as FERMI[59, 60, 61], HESS[62], MAGIC[63], and VERITAS[64, 65] are studying gamma rays fluxes. The main emphasis in gamma ray searches is on the galactic center, dwarf galaxies and galaxy clusters that have a high mass to light ratio.
Recent findings with FERMI[59, 60, 61] are indicating a possible dark matter signal (4.5 σ) for a WIMP with a mass of 130 GeV shown in figure 2.14, confirmation of these results is ongoing as there is a possible astrophysical[66] and instrumental explanation for the signal.

In addition to e^+/e^-, gamma rays, other experiments such as ANTARES[67], ICECUBE[68, 69], and Super-Kamiokande[70] search for dark matter via its neutrino signal. These searches focus usually on the Sun, Earth, Galactic-Center, Galactic-Halo[71] (figure 2.15), and dwarf galaxies. Best limits from these experiments are usually on dark matter nuclei spin-dependent cross-section in the Sun, there are yet any signal detected as to indicate a possible dark matter particle. It is important to note here that only dark matter searches in the Sun put limits on WIMP-nucleon elastic cross-section (otherwise it is annihilation cross-section) from the capture process. The reason to put limits on the spin-dependent (limits can be put on indepent cross-sections but they are much weaker) is because the Sun is made of light nuclei such as Hydrogen and Helium this renders the search more sensitive to the spin-dependent elastic cross-sections (equations 2.17 & 2.15).

2.4 Dark matter in the Sun

The average local dark matter density is 0.3 GeV/cm^3[72] and its velocity has a Maxwell distribution with an average speed of 270km/s[72]. The Sun's speed in our galaxy is about 220km/s[73] and the escape velocity of our solar system is

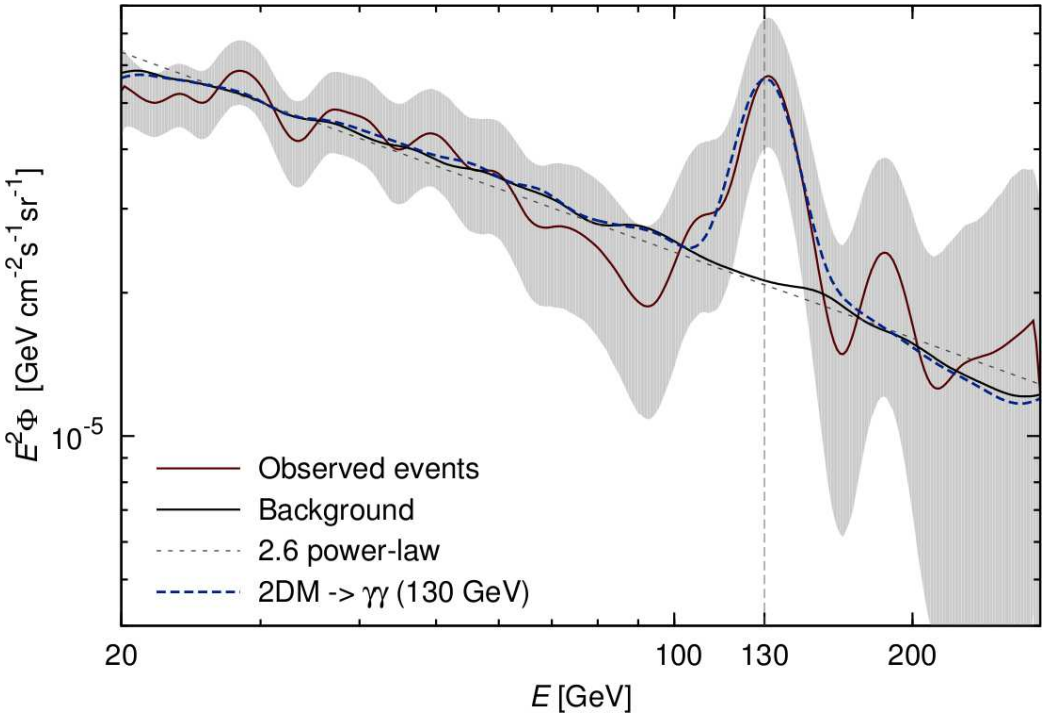

Figure 2.14: Detected gamma ray flux with FERMI as a function of photon energy. A comparison is also shown between the expected background (power-law 2.6), observed events and a spectrum from a 130 GeV dark matter annihilation into two photons. Plot obtained from [61].

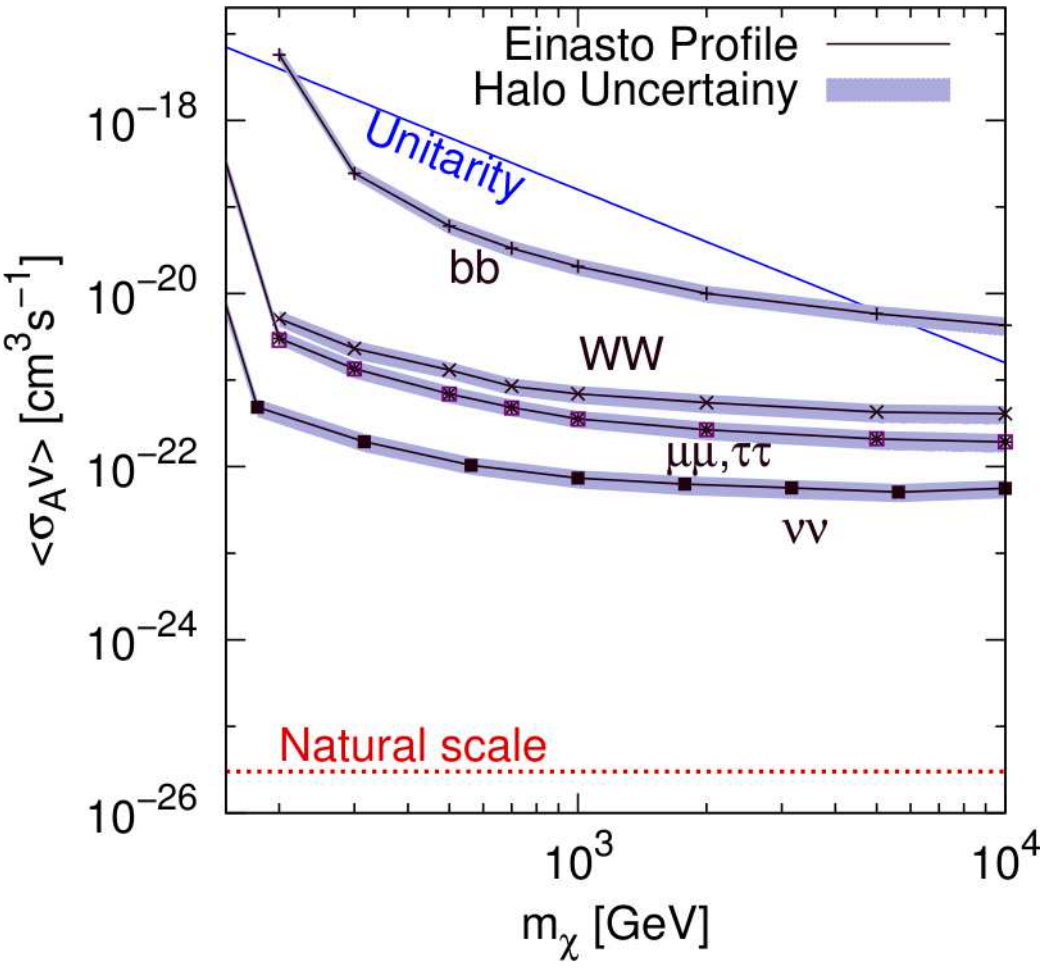

Figure 2.15: Upper limit on the dark matter self annihilation cross section for five different annihilation channels. Also shown are the natural scale (red dotted line), for which the WIMP is a thermal relic, and unitarity bound (blue line). For the limit curves, the central line is for the Einasto and NFW profiles, while the shaded width identifies the extrema results from the Moore and Kravtsov profiles. Plot from ICECUBE galactic halo analysis[71].

600km/s. If we assume the worst case scenario where dark matter is uniformly rotating in the opposite direction of the Sun, it would still put dark matter relative speed below the Sun's escape velocity ensuring that any dark matter particle that falls under the Sun's gravitation well will get trapped. Additionally as we saw earlier, dark matter by interacting with nuclei can lose kinetic energy and get trapped inside heavy celestial objects. The scenario where WIMPs get trapped inside the Sun and get by repeated (over a long time) elastic collisions with the nuclei sink to the core and annihilate, seems to be an extremely plausible scenario.
Additionally the Sun is an attractive search place for dark matter for several reasons, the first one is minimal astrophysical uncertainty as searches for dark matter in the galactic center and galactic halo are very sensitive to the form of the halo (cusped or cored). Searching for dark matter in the Sun does not depend on the halo shape but on the local density which is independent from the halo shape. The second reason is that the astrophysical background for dark matter search in the Sun is cosmic-rays hitting the Sun and via p-p interaction creating neutrinos that will come from the direction of the Sun. This effect has been studied[74] and the expected number of events in a detector such as ANTARES is about 10^{-3} events per year. The final reason is Solar physics that concern us are quite known and have minimal uncertainties.
After WIMPs annihilate, and through different various channels, we will end up with neutrinos (unless the channel was via photons or electrons). In order to have information on this neutrino flux and its eventual detection in ANTARES, several processes need to be known and calculated, presented as follows:

- Number of WIMPs in the Sun as a function of capture rate and annihilation.
- Interaction of the resulting particles from annihilation: τ regeneration, hadronization of quarks, etc.
- Neutrino oscillation and interaction from creation point to the detector.

Annihilation rate in the Sun

The number of WIMPs in the Sun can be described through the following equation[75]:

$$\frac{dN}{dt} = C_C - C_A.N^2 \tag{2.18}$$

The term C_C is the WIMPs capture rate by the Sun this factor is mainly determined by the spin-dependent cross-section of WIMPs on protons. The term C_A is the annihilation term, which is dependent on the annihilation cross-section of WIMPS. Now if we want to calculate the WIMPs annihilation rate Γ_A (eq 2.19 &

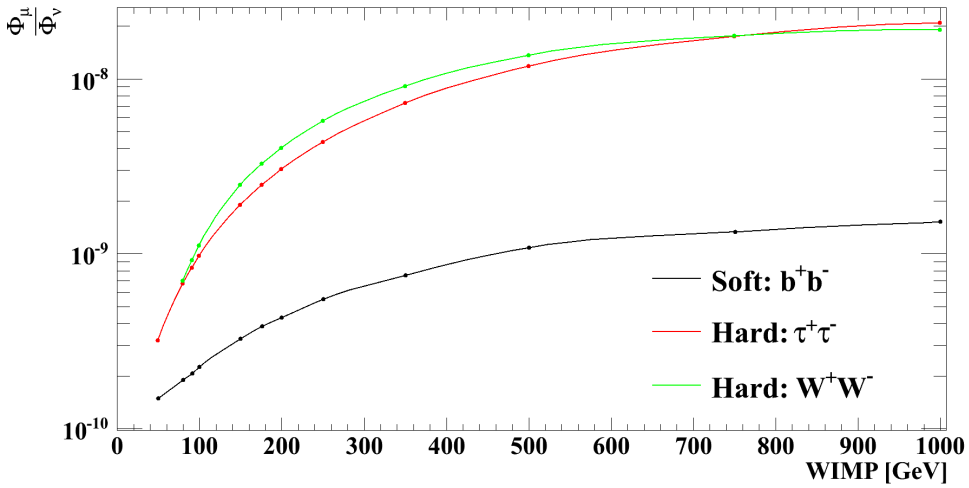

Figure 2.16: Conversion factor from neutrino flux to muon flux as a function of the annihilation channel and WIMP mass.

2.20)

$$\Gamma_A = \frac{1}{2} C_A N^2 \tag{2.19}$$

$$\Gamma_A = \frac{1}{2} C_C \tanh^2(\frac{t}{\tau}) \tag{2.20}$$

$$\tau = \frac{1}{\sqrt{C_C C_A}} \tag{2.21}$$

We find that if we calculate this rate at our present time (age of the Sun) where $t = t^{\odot} \equiv 4.5 \cdot 10^9$ years we would get $\frac{t^{\odot}}{\tau} \gg 1 \Rightarrow \tanh^2(\frac{t^{\odot}}{\tau}) \to 1$. This means that $\frac{dN}{dt} = 0$, and that annihilation and capture are in equilibrium. The consequences of this is that once equilibrium is achieved the annihilation rate is dependent on the capture rate C_C. This translates to having the annihilation rare depending solely on the scattering cross-section.

Additionally the two conversion factors that allow us to convert neutrino flux to muon flux (figure 2.16), and the muon flux to spin-dependent and spin-independent(figure 2.17) cross-section were obtained from [75], the calculation was done via the web-based application[76] presented in the same paper.

Neutrino production

If we assume that our WIMPs are neutralino then the annihilation of a pair of WIMPs can not directly produce neutrinos (but it can if the WIMP is a Kaluza-

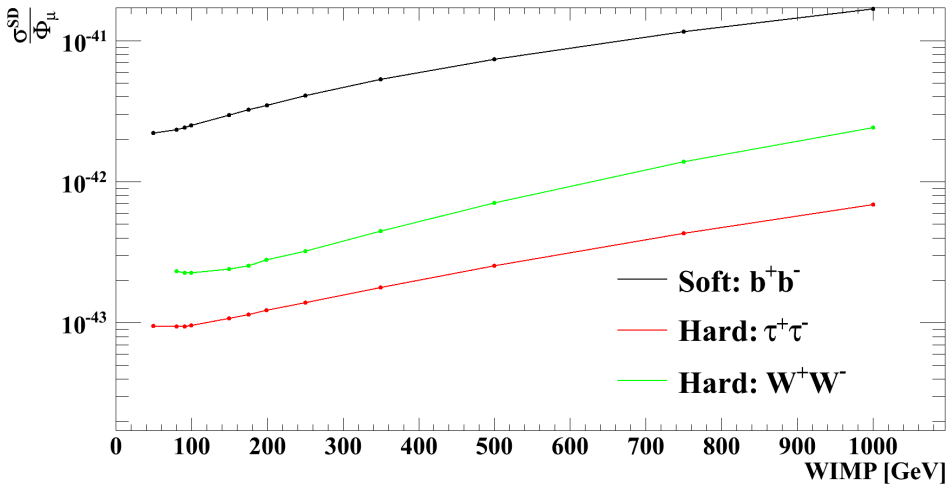

Figure 2.17: Conversion factor from muon flux $[km^{-2}][year^{-1}]$ to spin-dependent cross-section [pb] as a function of the annihilation channel and WIMP mass.

Klein particle). The generation of neutrinos is done via the decay of annihilation product. Lighter leptons such as electrons will not produce neutrinos, as they are stable and either they leave the Sun or get absorbed, and for muons they get absorbed before interacting. The important annihilation channels are: $b\bar{b}$, $c\bar{c}$, $t\bar{t}$, $\tau^+\tau^-$, W^+W^- , Z^0Z^0 , gg. The production of neutrinos is handled with PYTHIA[77], PYTHIA will propagate the particles, ensuring all possible interactions are taken into account and collects the (anti-)neutrino output. For example the b quark hadronize and produce B mesons where in the Sun they will interact before they decay, and this needs to be taken into consideration. Additionally, since the actual mass of the WIMP is not known then the neutrino production simulation is done for many masses: 10, 25, 50, 80.3, 91.2, 100, 150, 176, 200, 250, 350, 500, 750, 1000, 1500, 2000, 3000, 5000, and 10000 GeV. However, the ones we will use later in our analysis are: 50, 80.3, 91.2, 100, 150, 176, 200, 250, 350, 500, 750, and 1000 GeV. Finally not all channels are equal, some of them have a very soft spectrum such as the b channel, and some a quite hard such as the τ and W. The main emphasize later in the analysis part of this thesis is to focus on these three channels as we will not be looking at any model but try to be model-independent. These three channels will represent the extreme cases of dark matter annihilation. Any model in CMSSM will have varying branching ratio (but never 100%) to the different channels, making the whole parameter space of CMSSM located between the two limits set by the hard and soft channels.
In figure 2.18 we can see the neutrino yield after production for a WIMP mass of 200 GeV. We can see a comparison between the three favorite annihilation chan-

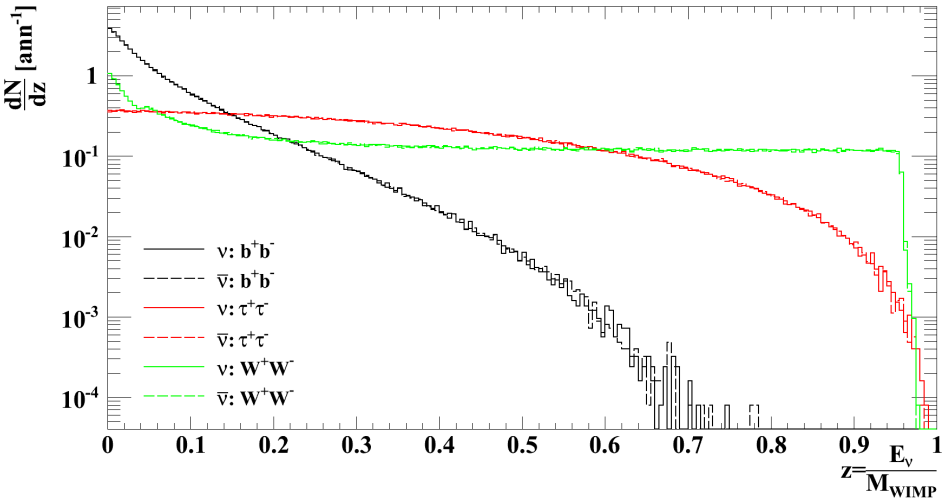

Figure 2.18: Flux of $\nu_\mu/\bar{\nu}_\mu$ at the Sun's center after production. The mass of the WIMP used here is 200 GeV. A comparison can be seen between the three channels $b\bar{b}$, $\tau^+\tau^-$, W^+W^- and between ν_μ and $\bar{\nu}_\mu$ flux.

nels $b\bar{b}$, $\tau^+\tau^-$, W^+W^-. It is immediately clear that the b channel is soft with the spectrum peaking at very small values of z ($z = \frac{E_\nu}{M_{WIMP}}$) and diminishing at larger values. The W channel on the other hand seem to be very hard as the spectrum is almost constant for all values of z. Finally the τ channel is hard as well but the spectrum starts to fall when the energy of the neutrino is 80% of the mass of the WIMP. However, for smaller values it is roughly constant.

Neutrino interaction

The neutrino interaction will be described in the next chapter. While the description is based for rock and sea water (Earth), the underlying physics is the same for neutrino interactions in the Sun.

Neutrino oscillations

The principle of neutrino oscillations scenario is related to the idea that the neutrino leptonic flavor eigenstates are not the same as the neutrino mass eigenstates. This leads to a mixing scenario where the flavor eigenstate becomes a linear combination of those of the mass. This oscillation scenario has been verified experimentally by several experiments such as Super-kamiokande[78, 79], SNO[80], K2K[81], and other.

The eigenstate mixing can be written as following:

$$|\nu_i\rangle = \sum_{n=1,2,3} U_{in}|\nu_n\rangle \quad (2.22)$$

$$|\nu_n\rangle = \sum_{i=1,2,3} U^*_{in}|\nu_i\rangle \quad (2.23)$$

The parameters i and U in equations 2.22 and 2.23 refers to leptonic flavors e μ and τ, and U being the leptonic mixing matrix[82].

$$U = \begin{pmatrix} c_{13}c_{12} & c_{13}s_{12} & s_{13}e^{-i\delta} \\ -s_{12}c_{23} - c_{12}s_{23}s_{13}e^{i\delta} & c_{12}c_{23} - s_{12}s_{23}s_{13}e^{i\delta} & s_{23}c_{13} \\ s_{12}s_{23} & -c_{12}s_{23} - s_{12}c_{23}s_{13}e^{i\delta} & c_{23}c_{13} \end{pmatrix}$$

The parameters in the U matrix are : $c_{ij} = \cos(\theta_{ij})$, $s_{ij} = \sin(\theta_{ij})$ where θ_{ij} being the mixing angle between two leptonic flavor, and finally δ being the CP violating phase.
The Hamiltonian of neutrino propagation in vacuum contains solely the oscillation matrix and can be written as following

$$H = \frac{1}{2E} \cdot U \cdot diag(0, \Delta m^2_{12}, \Delta m^2_{13}) \cdot U^\dagger \quad (2.24)$$

The Δm^2 terms in equation 2.24 are the neutrino squared mass differences. The temporal state of the neutrino can be written as $|\nu_i(t)\rangle = e^{-iHt}|\nu_i(0)\rangle$. While the neutrino oscillation does not depend whether it is in a vacuum or not, but when passing through matter $\nu_e/bar\nu_e$ interacts with electrons found orbiting the atoms and altering the Hamiltonian in equation 2.24 and causing additional oscillations, this is called Mikheyev-Smirnov-Wolfenstein (MSW) effect[83, 84]. The new Hamiltonian becomes:

$$H = \frac{1}{2E} \cdot U \cdot diag(0, \Delta m^2_{12}, \Delta m^2_{13}) \cdot U^\dagger \pm diag(\sqrt{2}G_F N_e, 0, 0) \quad (2.25)$$

The G_F parameters in the new Hamiltonian in equation 2.25 is the Fermi coupling constant and N_e being the electron density.
The value of the parameters θ_{ij}, δ and Δm^2 are obtained via global fits[85] from the different neutrino experiments. These values are :

- $\theta_{12} = 33.2^\circ \pm 4.9^\circ$
- $\theta_{13} < 12.5^\circ$
- $\theta_{23} = 45.0^\circ \pm 10.6^\circ$

- $\delta \in [0, 2\pi[$
- $\Delta m^2_{12} = (8.1^{+1.0}_{-0.9}) \cdot 10^{-5} eV^2$
- $\Delta m^2_{13} = (2.2^{+1.1}_{-0.8}) \cdot 10^{-3} eV^2$

Figure 2.19 shows us the neutrino flux at Sun's surface for a WIMP mass of 200 GeV. We can see a comparison between the annihilation channels $b\bar{b}$, $\tau^+\tau^-$, and W^+W^-. The first noticeable effect is the clear sign of neutrino oscillation on the flux as a function of the energy (z). The other effect is that while in figure 2.18 there was no difference between neutrinos and anti-neutrinos, now we see that we have more anti-neutrinos than neutrinos. This difference is due to the fact that neutrinos interacts with higher probability with matter when compared to anti-neutrinos making absorption of neutrinos in the Sun slightly higher (anti-neutrinos will interact slightly higher with anti-matter than neutrinos).
Additionally in figure 2.20 we can see the final neutrino flux at 1 AU from the Sun (1 AU is one astronomical unit which is the average distance from the Sun to Earth). In this figure we can see that the rough oscillation we saw in figure 2.19 have smoothed out. Additionally no more absorption of neutrinos is present as the space between the Sun and Earth is empty. This figure shows us the final expected neutrino (anti-neutrino) flux we get from a WIMP mass of 250 GeV. This flux presented here with addition of other WIMP masses will be used later in the analysis chapters to estimate a signal coming from dark matter annihilation in Sun.

Neutrino Flux simulation

The neutrino fluxes were obtained via WIMPSIM[86], an introduction on the software package is found in section 5.1.

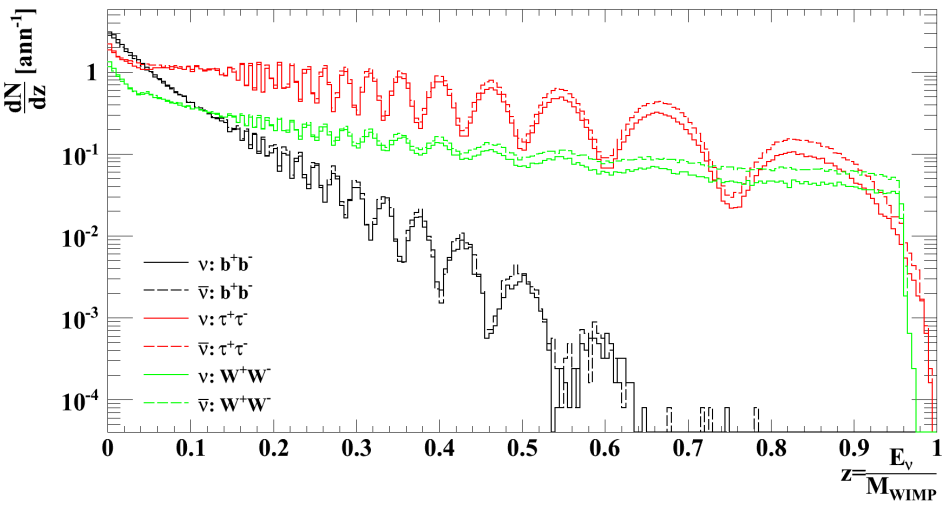

Figure 2.19: Flux of $\nu_\mu/\bar{\nu}_\mu$ at the Sun's Surface after production and propagation. The mass of the WIMP used here is 200 GeV. A comparison can be seen between the three channels $b\bar{b}$, $\tau^+\tau^-$, W^+W^- and between ν_μ and $\bar{\nu}_\mu$ flux.

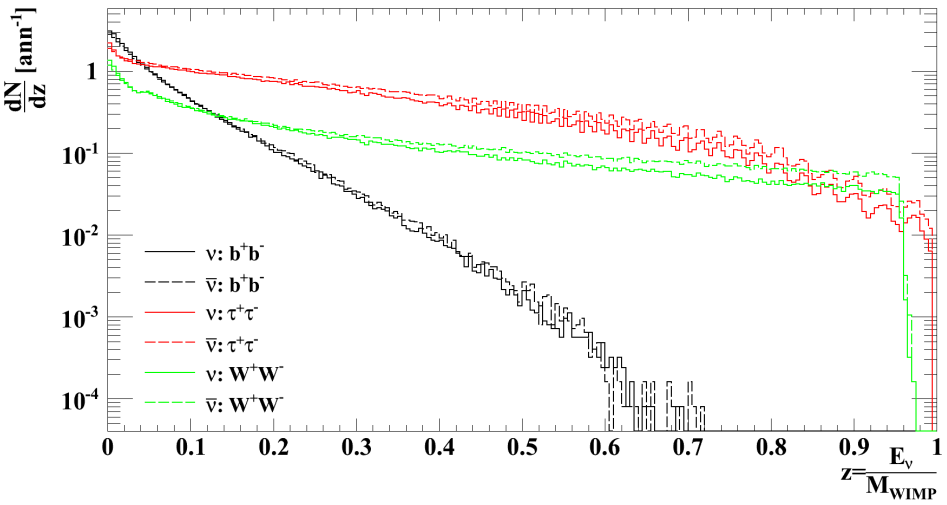

Figure 2.20: Flux of $\nu_\mu/\bar{\nu}_\mu$ at 1 AU (astronomical unit roughly the distance from the Sun to earth). The mass of the WIMP used here is 200 GeV. A comparison can be seen between the three channels $b\bar{b}$, $\tau^+\tau^-$, W^+W^- and between ν_μ and $\bar{\nu}_\mu$ flux.

Chapter 3

The ANTARES Neutrino Telescope

In this chapter the detection of neutrinos with the ANTARES neutrino telescope is discussed, followed by an overall review of the detector.

3.1 Neutrino interaction with matter

While neutrinos are abundant in the universe and are a frequent byproduct of any process that involves the weak force, their detection is plagued by the fact that the neutrino cross section is extremely small since the only interactions a neutrino experiences are the weak force and the gravitational force. However, the υ-matter cross section increases with the energy of the neutrino as seen in Figure 3.1. This provides us with the chance for the detection of high energy neutrinos interacting with matter.

Usually a neutrino interacting with matter, will either hit a neutron or a proton that exists inside the nucleus of an atom. However, the only important distinction is whether the interaction is via charged current (CC) or neutral current (NC) as seen in Figure 3.1. In a CC interaction the result is the corresponding lepton plus a hadronic shower, while the NC interaction results with the same flavor neutrino and a hadronic shower (eq 3.1 & 3.2).

$$\begin{array}{ccc} & CC & \\ \nu_e + N/P & \rightarrow & e + X \\ \nu_\mu + N/P & \rightarrow & \mu + X \\ \nu_\tau + N/P & \rightarrow & \tau + X \end{array} \tag{3.1}$$

$$\begin{array}{ccc} & NC & \\ \nu_e + N/P & \rightarrow & \nu_e + X \end{array} \tag{3.2}$$

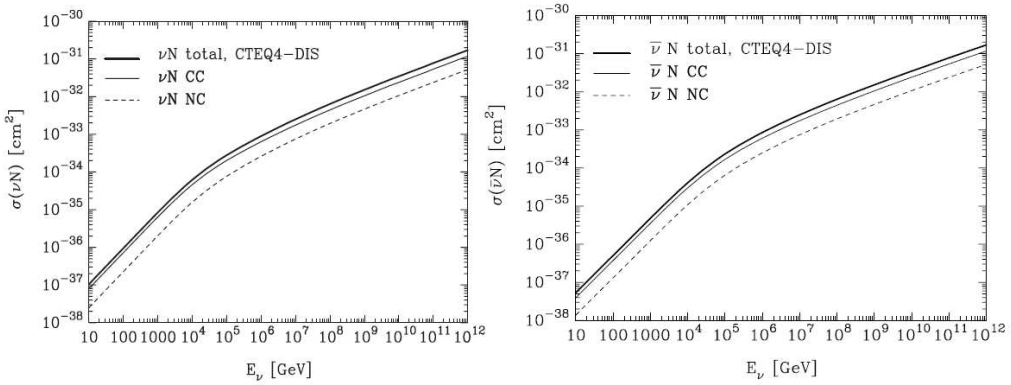

Figure 3.1: The neutral current (NC), charged current (CC) and total cross section of neutrinos (left) and anti-neutrinos (right), with matter as a function of the neutrino energy.

$$\begin{aligned} \nu_\mu + N/P &\rightarrow \nu_\mu + X \\ \nu_\tau + N/P &\rightarrow \nu_\tau + X \end{aligned}$$

However, since the NC cross-section is about an order of magnitude lower than the CC cross-section, the most significant signature of a neutrino comes from the latter. Since the nuclear interaction length is less than one meter, we would expect the hadronic shower signature to dissipate before having a chance to be detected if it was produced far from our apparatus, henceforth the accompanying lepton offers a higher chance for detection inside a medium such as water.

We would expect a charged particle (our corresponding lepton) with relativistic speeds to dissipate its energy in several ways:

3.1.1 Bremsstrahlung radiation

Bremsstrahlung radiation is an electromagnetic radiation emitted by a charged particle when it decelerates under the influence of the electrical field of another charged particle (Figure 3.2). In this case the first particle would be our lepton and the second the atomic nucleus of the matter of our environment (ex: water). However, its contribution to the total energy dissipated [87] depends on the mass of the lepton or implicitly on its flavor, it depends on γ^6 or γ^4 as seen in eq 3.3 & 3.4 (γ is the Lorentz factor) and we have $\gamma \sim m^{-1}$. So we can see that this radiation is more important for an electron than for a muon or a tau. $\frac{m_\mu}{m_e} \sim 200$ $\frac{m_\tau}{m_\mu} \sim 17$ so the Bremsstrahlung contribution to a muon who has the same energy as an electron would be between 9 and 13 orders of magnitude lower.

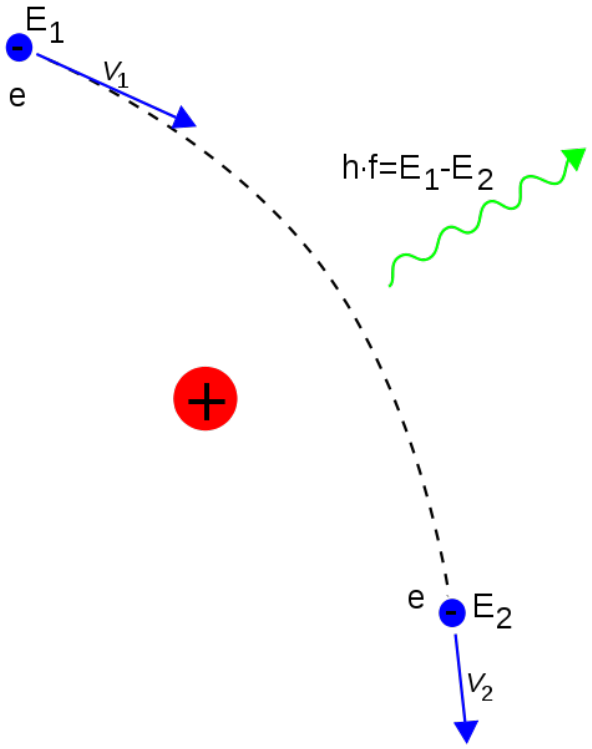

Figure 3.2: The process of production of a Bremsstrahlung radiation.

The total power P emitted depends on whether the charged particle is being accelerated (a) in the same direction of its velocity or perpendicular to it. But it also depends on the charge q of the particle as well.

$$P_{a||v} = \frac{q^2 a^2 \gamma^6}{6\pi\varepsilon_0 c^3} \tag{3.3}$$

$$P_{a\perp v} = \frac{q^2 a^2 \gamma^4}{6\pi\varepsilon_0 c^3} \tag{3.4}$$

3.1.2 Medium ionization

A charged particle traveling through matter would interacts with the electrons of the medium. This interaction if energetic enough can lead to the ionization of the atoms and henceforth a loss of energy (eq 3.5) of the traveling particle.

$$-\frac{dE}{dx} = \frac{4\pi}{m_e c^2}\frac{nz^2}{\beta^2}\left(\frac{e^2}{4\pi\varepsilon_0}\right)^2\left[log\left(\frac{2m_e c^2\beta^2}{I(1-\beta^2)}\right)-\beta^2\right] \tag{3.5}$$

Muon Energy (GeV)	$\frac{1}{p}\left\|\frac{dE}{dx}\right\|$ ($GeV.cm^2/g$)
1	0.0021
10	0.0025
100	0.003
1000	0.006
10000	0.036
100000	0.353

Table 3.1: Muon energy loss in water via ionization.

Where:
$-\frac{dE}{dx}$: is the energy loss of the lepton per distance unit [m].
z: is the charge of the particle.
n : Electron density of the medium.
I : mean excitation potential of the medium atoms.
A muon traveling through water would lose energy more or less as the log of it is energy (Table 3.1).

3.1.3 Pair production

If $E_{Particle} > 2m_l c^2$ where$m_l$is a mass of one of the three leptons, we would expect for some energy to be lost via a production of a lepton anti-lepton pair. However, this effect is more relevant at high energies as seen in eq 3.6

$$-\frac{dE}{dx} \sim E^4_{lepton} \tag{3.6}$$

3.1.4 Cherenkov radiation

The Cherenkov radiation is a special case, where the particle is not just energetic, but the velocity of the lepton is higher than the speed of light in the medium. The radiation is continuous , and is emitted at an angle (Figure 3.3) defined as following (eq 3.7) where $\beta = \frac{v}{c}$ and n is the refraction index of the medium.

$$cos(\theta) \quad = \quad \frac{1}{\beta n} \tag{3.7}$$

For example in the case of ANTARES, which is an underwater neutrino telescope, trying to detect ultra-relativistic particles ($\beta \simeq 1$) , and with water index $n = 1.35$, the emission angle would be at 42.2 degrees.

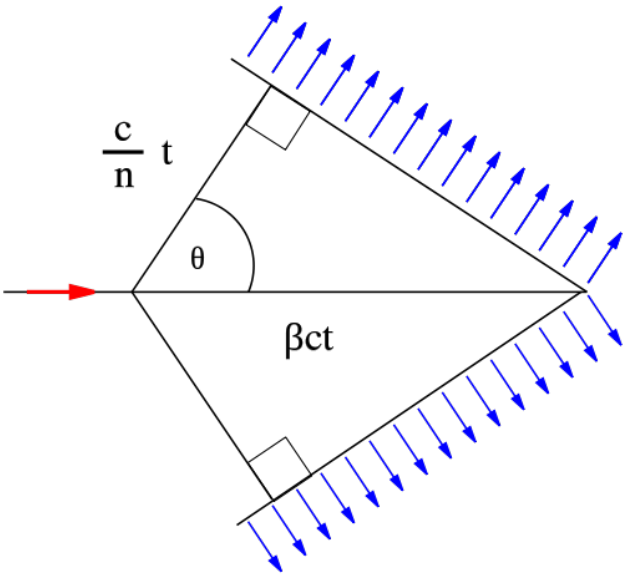

Figure 3.3: Diagram of a particle undergoing Cherenkov radiation

It is interesting to note that because of the muon's mass and lifetime, it is much more effective to detect a muon in a medium such as water than to detect an electron or a tau. An electron has a small mass, and would lose most of its energy via ionization or bremsstrahlung radiation at low and high energy respectively, and as for the tau and its extremely short lifetime 3.10^{-13}[s] it will decay very fast before deposing its light in the detector, unless its energy is high enough $\sim 10^6$ GeV which is well above the energies of dark matter research).

However, the amount of energy a muon would lose via Cherenkov radiation is negligible when compared to other processes. The number of photons a muon would generate is roughly 330 photon per cm in the visible part of the spectrum [400 - 700 nm] if the energy of the muon is well above the Cherenkov energy limit which is the case as we would be expecting high energy neutrinos (eq 3.8), but the total energy of these photons would be around $165 eV^{-1} cm^{-1}$(eq 3.9) which is almost three orders of magnitude smaller than the energy loss due to the ionization in water.

$$\begin{aligned} \frac{d^2N}{dxd\lambda} &= \frac{4\pi^2 z^2 e^2}{hc\lambda^2}\left(1-\frac{1}{\beta^2 n^2}\right) \\ \frac{d^2N}{dxd\lambda} &= \frac{2\pi\alpha}{\lambda^2}\sin^2(\theta) \end{aligned} \tag{3.8}$$

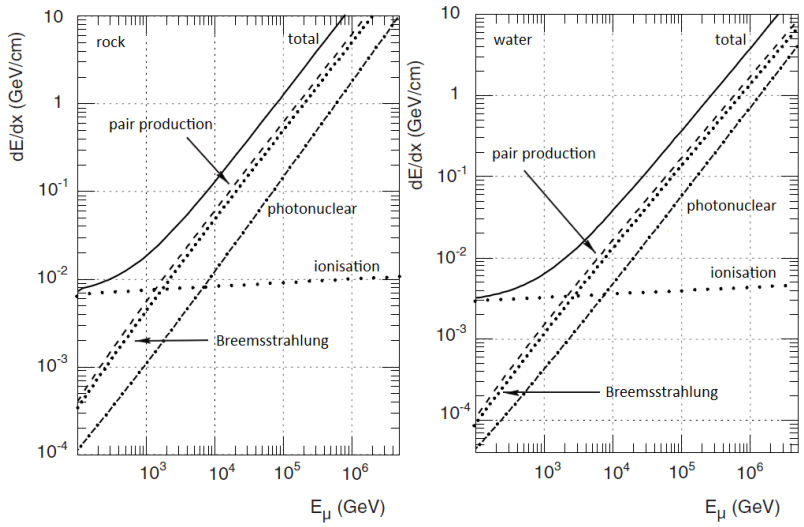

Figure 3.4: Energy loss of per distance as function of the energy of the muon in rock (on the left) and sea water (on the right).

$$\frac{d^2N}{dEdx} = \frac{\alpha}{\hbar c} sin^2(\theta) \tag{3.9}$$

At low muon energies the ionization process dominate, while at high energy (above 1 TeV) we would expect the Bremsstrahlung radiation and lepton pair production to dominate (Figure 3.4).

So while the Cherenkov radiation in itself does not contribute much in energy dissipation, its continuous nature can help in tracking the muon in water. The mean angle at which the muon is emitted after the neutrino interacts can be small enough to track the direction of the neutrino albeit with some amount of uncertainty (Figure 3.5).

3.2 Neutrino telescopes

As shown in the previous section neutrinos can be used to do astronomy. The concept revolves around a neutrino (more specifically a ν_μ) interacting in the vicinity of a dense and clear medium such ice or water and producing primarily a muon, this muon can then go on to produce a continuous ray of photons at a very specific angle and spectrum as it moves in the medium due to Cherenkov radiation (section 3.1.4). Now muons can propagate between few meters and few

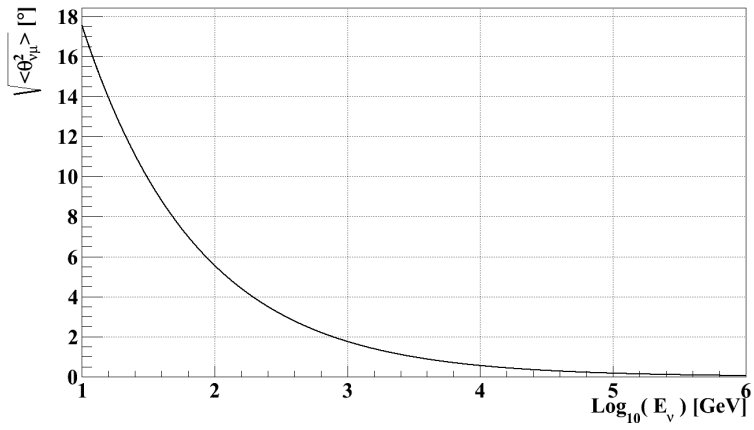

Figure 3.5: Mean kinematic angle between the neutrino and the muon as a function of energy of the neutrino.

kilometers depending on its energy (Figure 3.6), so the photons generated by the radiation would be distributed over a large volume. The detector thus has to be large enough in order to track a fair portion of the emissions as it passes through the detector. Since the ν-matter cross section is very small, we would need the interacting medium to have primarily two proprieties, to be dense and extremely large, the solution is to use the Earth itself as the interacting medium. This is achieved by looking at upward going neutrinos passing through from the other side of the Earth and interacting below the detector. The reason for this has to do with the detection principle: we want to detect neutrinos induced muons, but the fact is that since the Earth is bombarded constantly and heavily by cosmic rays, and its interaction with our atmosphere produce many particles (Figure 3.7) including muons. And as we saw earlier muons can travel large distance and certainly the distance between the atmosphere to the surface of the Earth if they are energetic enough. So the detection will be contaminated by muons (Figure 3.8) coming from above the detector as a result from cosmic rays interactions, so by selecting muons that are traveling upward in the detector apparatus, we can eliminate this contamination[1].

3.2.1 ANTARES

ANTARES[67] (Astronomy with a Neutrino Telescope and Abyss environmental RESearch) is a neutrino Cherenkov telescope located 40 km off the city of Toulon,

[1] Of course cosmic rays create neutrinos as well, and they can travel through the Earth, but this will be discussed later.

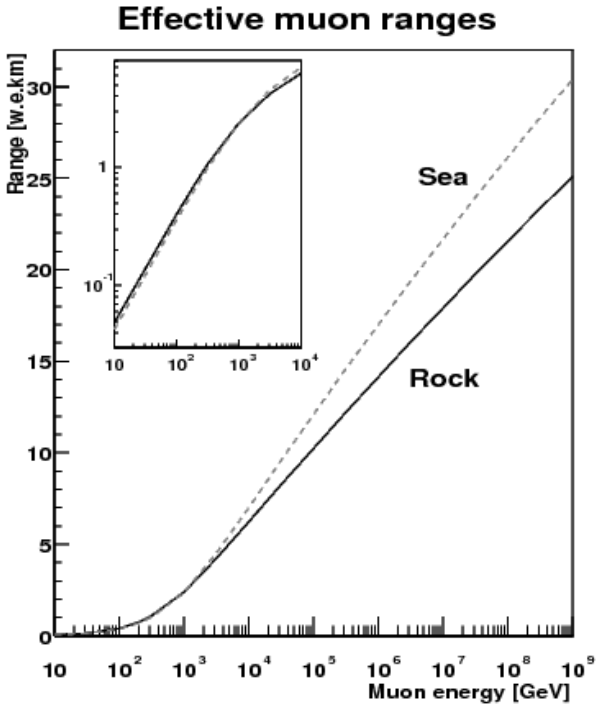

Figure 3.6: Effective muon range as function of its energy[88]

France in the Mediterranean sea (Figure 3.9) which happens to be the first fully operational under sea water neutrino telescope.

The detector is located at a depth of 2.5 km in sea water, the telescope stands at a height of 500 m and consists of 12 lines, each line consists of 25 stories. Each storey is made up of three optical module and the electronics, each OM contains a PMT (PhotoMultiplier Tube), tilted downward at an angle of 45° to maximize upward going Cherenkov tracks. totaling up in 885 OMs (Figure 3.10). Each line is connected to the sea floor via an anchor, and all are connected via electro-optical cable to the junction box which itself is connected to the offshore station by an identical electro-optical cable. All these different components will be described in the next section.

The muon detection principle is based on while knowing the precise position of each OM the track can be reconstructed by knowing the the time difference between the different registered hits in the detector (Figure 3.11).

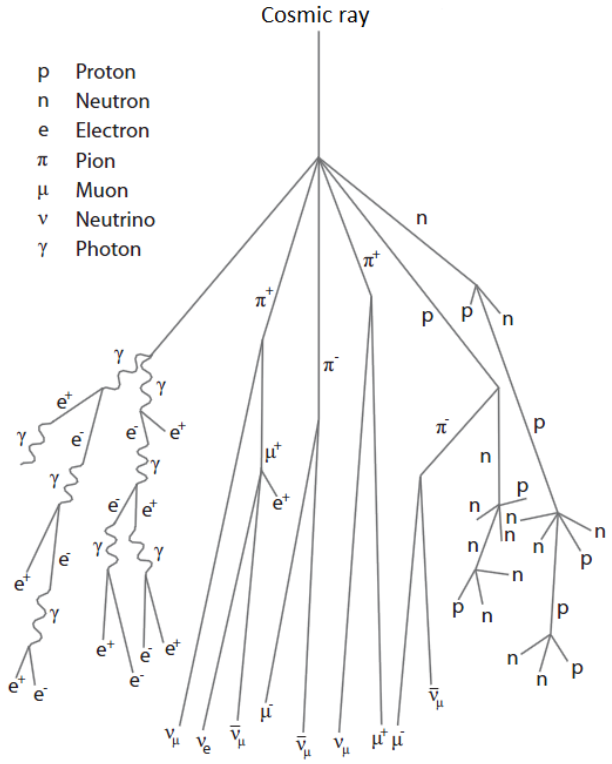

Figure 3.7: Particle shower that is the outcome of a cosmic ray particle interacting with Earth's atmosphere.

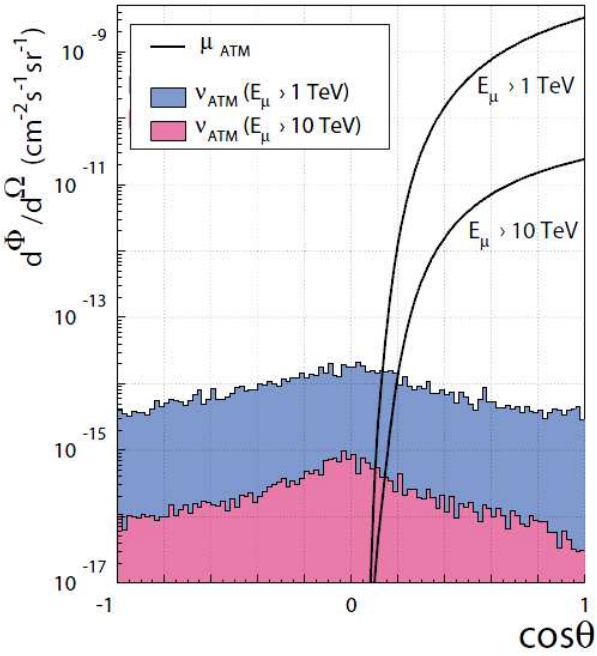

Figure 3.8: Differential flux of atmospheric neutrinos and muons as a function of the cos[zenith] angle. The four plots are a result of a monte carlo simulation for the ANTARES detector.

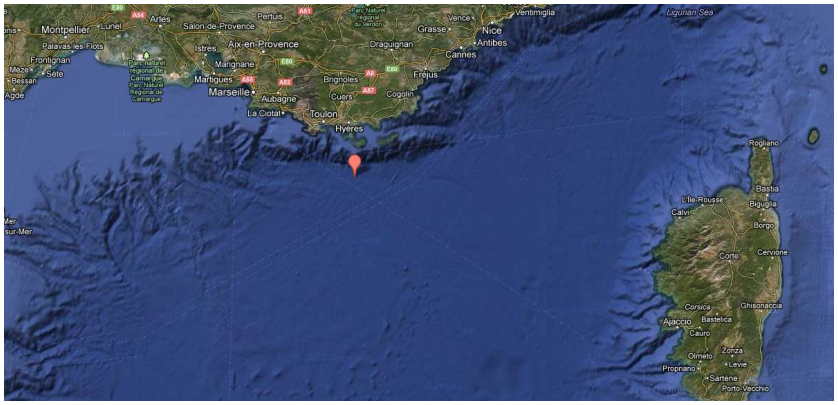

Figure 3.9: ANTARES location in the Mediterranean sea (red balloon)

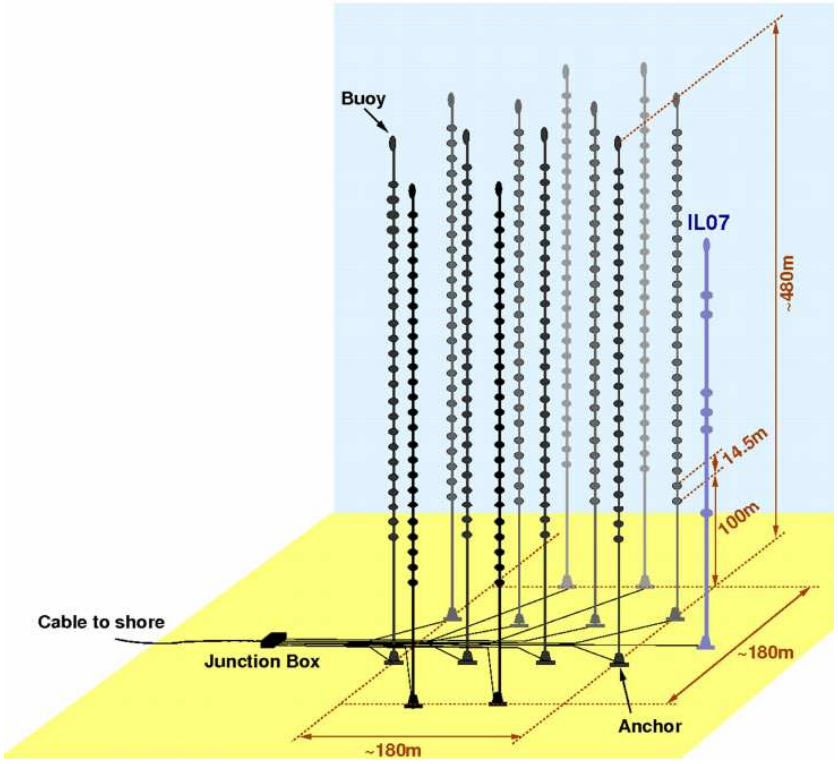

Figure 3.10: Detector layout

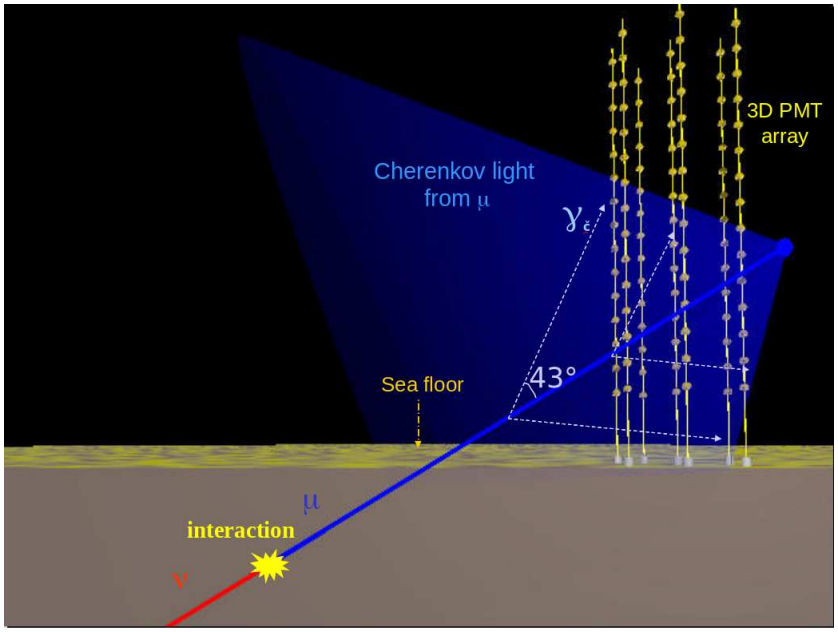

Figure 3.11: Detection principle for ANTARES.

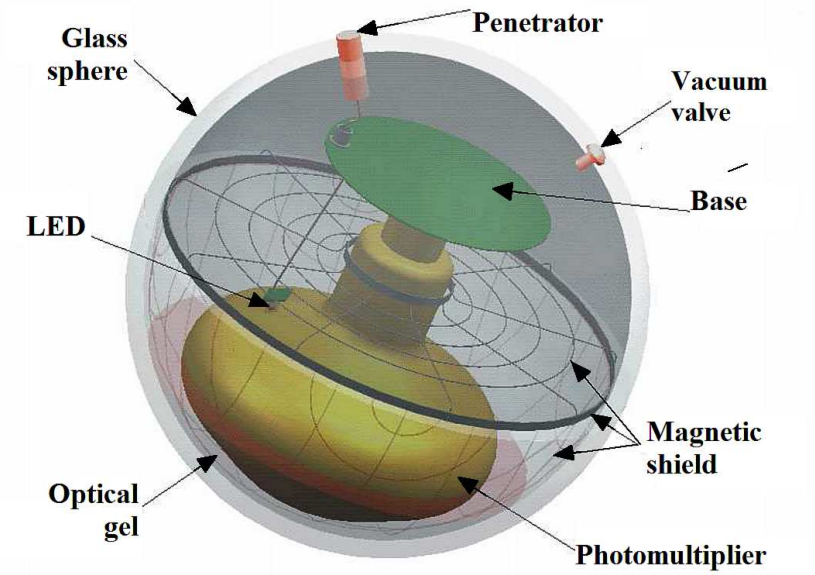

Figure 3.12: ANTARES Optical Module

3.2.1.1 Detector layout

Optical Module

The OM[89] is a vacuum sealed sphere made of glass, it contains among several things, a magnetic shield, a LED (light emitting diode) and most importantly a PMT (Figure 3.12) or PhotoMultiplier Tube is the basic unit of ANTARES. The role of an PMT is to allow the detection of photon(s) by magnifying the electrical current induced by them. This is important as the number of photons produced in a Cherenkov cone is extremely small when compared to the physical size of the detector. In the case of ANTARES these PMTs have to be sensitive to single photons in the visible domain.

Some of the most important characteristic of the PMTs used in ANTARES are as following:

- Photocathode area > 500 cm2
- Quantum efficiency > 20 %
- Collection efficiency > 80%
- TTS (Transit Time Spead) < 3 ns
- Dark count rate < 10 kHz
- Gain up to 5.10^7

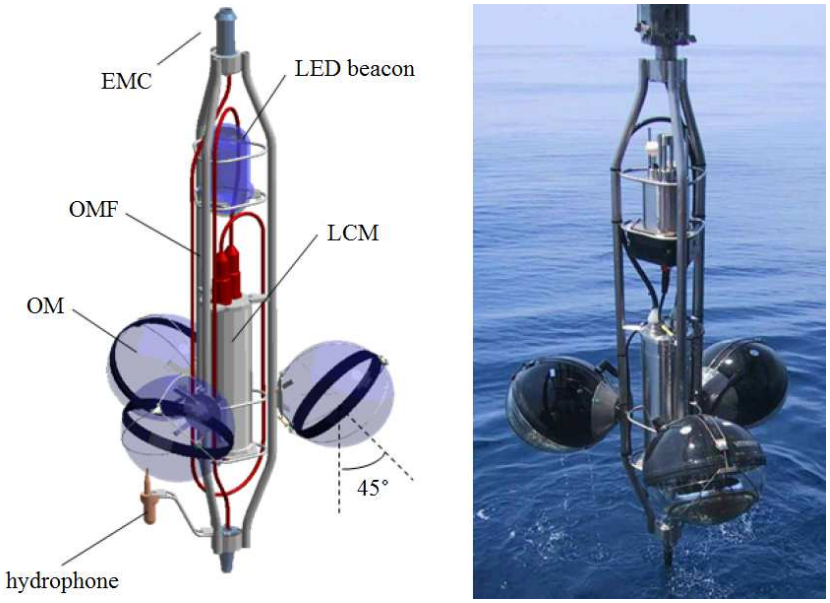

Figure 3.13: ANTARES storey

Storey

The role of the stories (Figure 3.13) in ANTARES is simply to provide a physical support for the three OMs, and for the LCMs (Local Control Module).

The purpose of the LCM is to house the electronics that is needed to power the OMs, processing of the signal, and finally link different stories together.

The most important part of the LCM are:

- The LPB or the Local Power Box which role is to deliver the power for the electronics and the OMs of the storey.
- The CLOCK board which has the role of relaying the synchronization clock signal of the stories (ask again about this).
- The ARS motherboard which does the processing and digitization of the analogue signal sent from the PMTs, the output would be a digital signal containing the hit time and the hit charge.
- The DAQ/SC board which mainly hosts the operating system and gathers the data to be sent to the onshore for storage.
- The COMPASS motherboard that hosts the local sensors that detect the yaw, pitch, and roll, the temperature and the humidity. In addition to the high voltage control that is needed to power the PMTs

- The LED (light emitting diode) beacon, and its main function is the time calibration of the detector.
- The Hydrophones: Their main function is the acoustic positioning of the detector.

The roles of the LED beacon and the hydrophones will be explained more thoroughly in section 3.2.1.2.

Lines

There are 12+1 lines in ANTARES. Twelve lines that house the actual detector, and each line consists as previously mentioned of 25 stories. The extra line is an instrumentation line (IL07) (Figure 3.14) which holds an acoustic detection system and other oceanographic instruments. IL07 is made up of only six stories.

The acoustics detection system (AMADEUS[90]) on the instrumentation line has the role of detecting neutrinos through an acoustic signal. The standard OMs are replaced with special acoustic sensors. There is three of these floors on the IL07 and an additional three on the line 12 of the ANTARES detector. Each floor holds six acoustic sensors all distanced from each other by 1 m.

The other instruments on the IL07 are meant to do studies of the propriety of the environment around ANTARES, such as the Acoustic Doppler Current Profilers (ADCP) which measures the direction and speed of sea current. There is as well a sound velocimeter to measure the local velocity of sound, in addition to sensors that measure the conductivity and temperature of sea water. There is as well other instruments to measure the light attenuation of the water, amount of oxygen in the water and cameras to monitor the bio-luminescent organisms around the detector.

Junction box

The role of the junction is two fold. The first one is link all the lines together electronically and to be a relay between the onshore control center and the detector via the optical network. The second is to provide power to the whole detector as it houses the power transformers.

Electro-Optical cable

The electro-optical cable is a two-in-one cable that connects the onshore control station and the detector. It provides the electrical power for the detector and the data transmission capabilities.

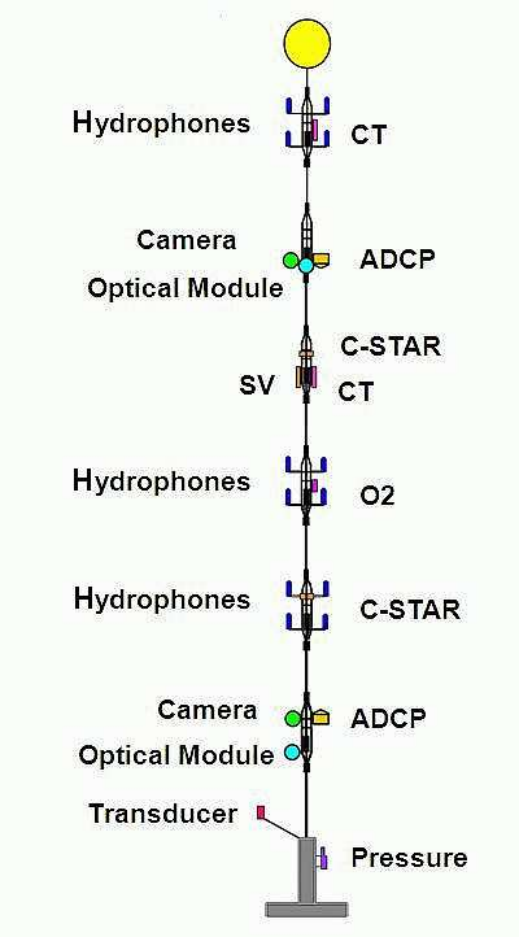

Figure 3.14: Instrumentation line IL07

Anchor & Buoy

Each line is anchored to the sea bed via a bottom string socket (BSS) , every BSS is as well equipped with a autonomous transponder that can help to position itself with reference to acoustic transponders located around the detector . Each line is equipped with an anchor as well with a buoy, the role of the buoy is simply to hold the line straight. On a side note, the BSS of lines 7 and 8 hold a laser beacon which is use to do inter-line offset calibration, this will be discussed in the next section .

3.2.1.2 Calibration

As previously mentioned the LED's and hydrophones installed on the stories and the BSS' are used to calibrate the detector. The ANTARES detector calibration is divided into three separate but yet important calibration systems:

Positioning and pointing

In order to accurately pinpoint astrophysical objects with reference to ANTARES a positioning and pointing calibration should be performed. This is done with the LFLBL (Low Frequency Long BaseLine positioning system[91]) acoustic positioning system found on the BSS of every line. This system uses frequencies between 8 and 16 KHz , this range of frequencies helps determine the overall position of ANTARES by triangulation with five transponders located around the detector with an addition of a ship positioned above the detector. With the help of more than 100 GPS positioning calculation done on the ship, an absolute position of ANTARES relative to earth with an accuracy of 1 m and an accuracy of $1^\circ$and 0.1° degrees in horizontal and vertical pointing.

In addition to using the acoustic system to calibrate the pointing of ANTARES two other methods are implemented to independently verify the results.

Moon Shadow

As the Moon rotates around Earth it will block cosmic rays (Figure 3.16), this will results with fewer than expected number of down-going muons in the direction of the Moon. So one method of verifying the pointing of ANTARES is to look for a deviation of the deficit of down-going muons in respect to the expected Moon position for ANTARES. It is expected that with enough data (at least 5 years) we would be able to improve the horizontal pointing accuracy below 1°.

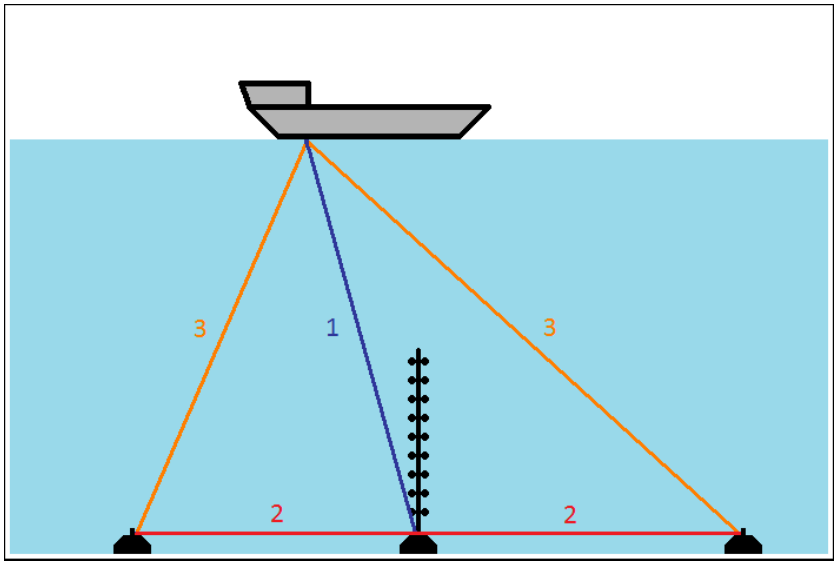

Figure 3.15: The LFLBL system, measurements of distance are done between the BSS and the transponders, BSS and the ship, and between transponders and the ship.

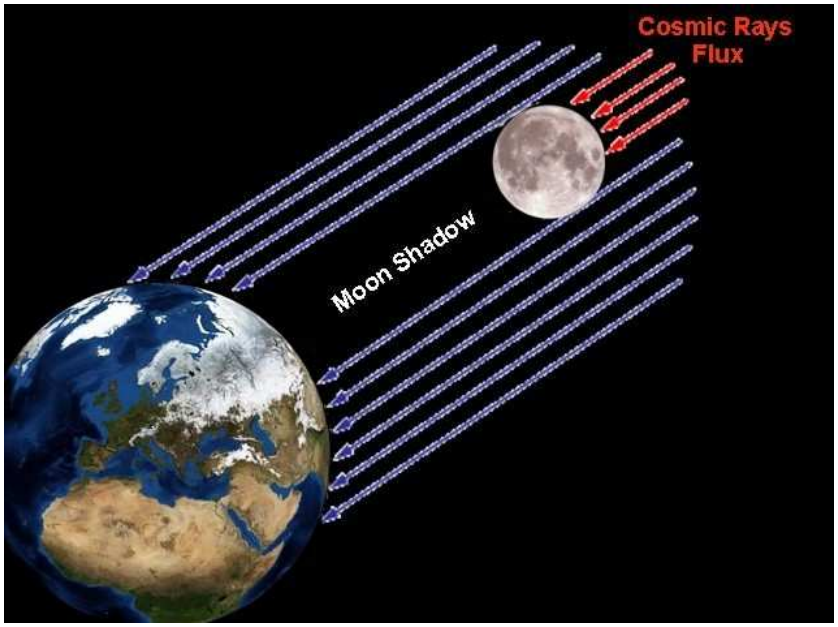

Figure 3.16: Moon shadow with cosmic rays.

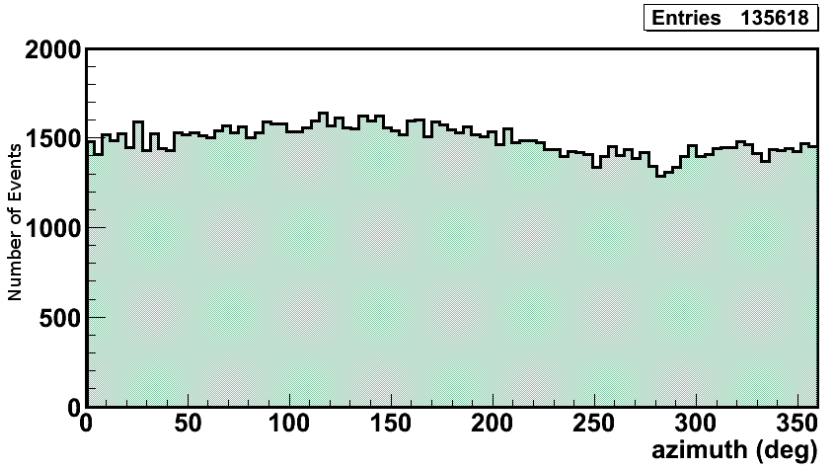

Figure 3.17: Distribution of azimuth angle for events detected by the surface array.

Surface Array

During maintenance operations where we might be recovering or re-installing some detector lines a boat is usually located approximately above the detector for few days. On top of the boat a collection of muon detectors is fitted. The role of the surface array is to study muon events that are both detected by the surface array and the detector ($\sim$ 13 events per day). With the position of the boat precisely known with the help of GPS, the array can reconstruct the direction of the muon (Figure 3.17 & 3.18), after that it is compared to the reconstructed direction by ANTARES which is then results in estimation of the pointing accuracy of ANTARES. This uncertainty is proportional to $\frac{1}{\sqrt{N_{days}}}$. After one sea campaign which had 4 days of operation time, the resulting calculations showed no deviation of ANTARES pointing. However, more time is needed to refine the uncertainty estimations.

Detector dynamic geometry

Since the detector is a not a rigid structure and the shape of the detector lines (Figure 3.20) is under the constant influence of sea current (Figure 3.22), henceforth it is very important to know the dynamic detector geometry to accurately estimate the muon track direction. This is done via acoustic calibration, which uses the acoustic transponder that exists on the BSS of every line along with the hydrophones that are installed on some of the stories (Figure 3.21).

The HFLBL (High Frequency Long BaseLine positioning system[91]) acoustic positioning system uses frequencies between 40 and 60 KHz to calculate the distance between the BSS of each line, and 5 different stories all the lines. This

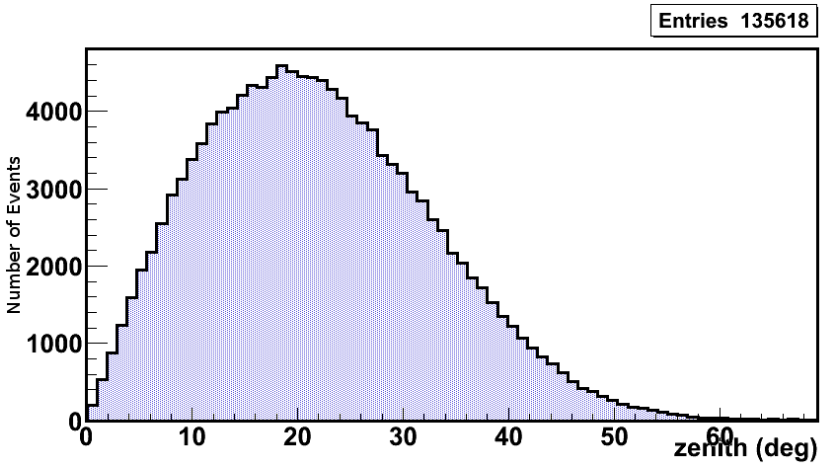

Figure 3.18: Distribution of zenith angle for events detected by the surface array.

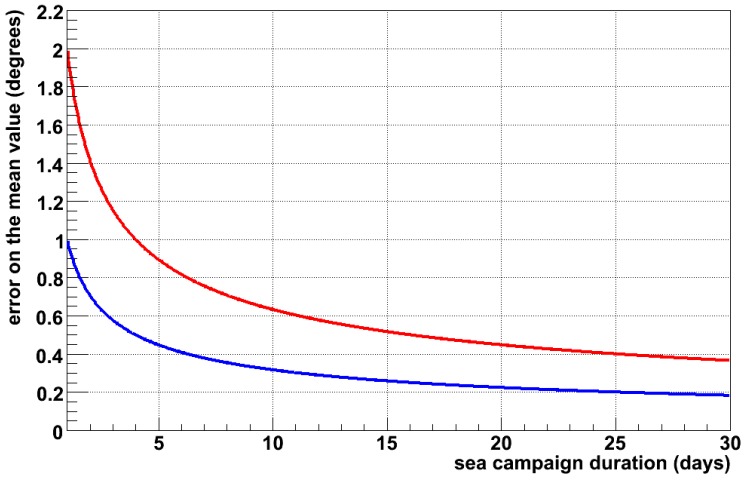

Figure 3.19: Estimation of the pointing uncertainty of the zenith angle (blue) and the azimuth angle (red) as a function of sea campaign duration.

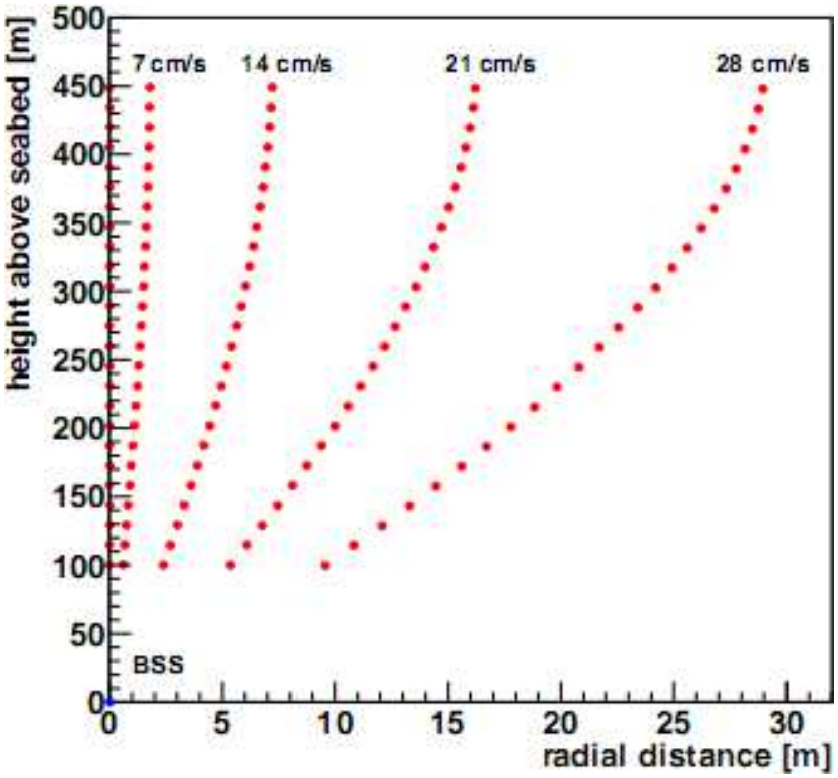

Figure 3.20: Height and radial displacement of each and every stories of a line for different sea current velocities.

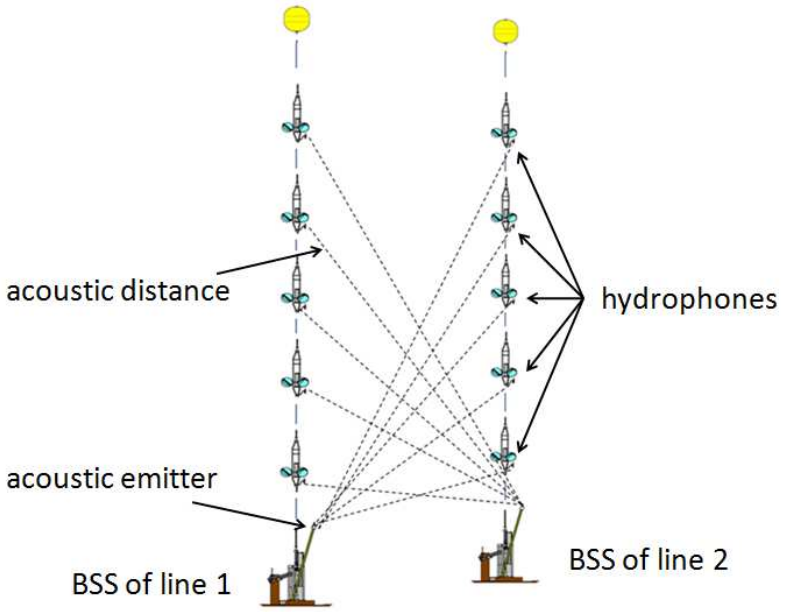

Figure 3.21: Diagram of how the HFLBL system works between two lines.

method allows us to gain a precision of 5 cm on each hydrophone and eventually on the OMs of each floor. In addition to the HFLBL, the compass-tiltmeter system found on every floor is used to estimate the position the remaining stories and this be able to have a fit of each line and in the process getting the full geometry of the detector. The eventual precision on the position of the OMs in around 10 cm. This calibration is done every two minutes.

Time Calibration

Reconstruction of a muon track does not only depends on knowing precisely the position of each OM, it also depends on knowing the time offset among the OMs as the timing is very critical.

Time uncertainty comes from three sources.

- The TTS (Transit Time Spread) which is equal to 1.3 ns.
- Sea water effect on light propagation, and it is dependent on two effects. Light scattering and chromatic dispersion, the contribution of these two effects is about 1.5 ns for photons traveling a distance of 40 m.
- Time residual offset which is equal to 0.5 ns.

The calibration is done by two different methods[92], onshore and in situ.

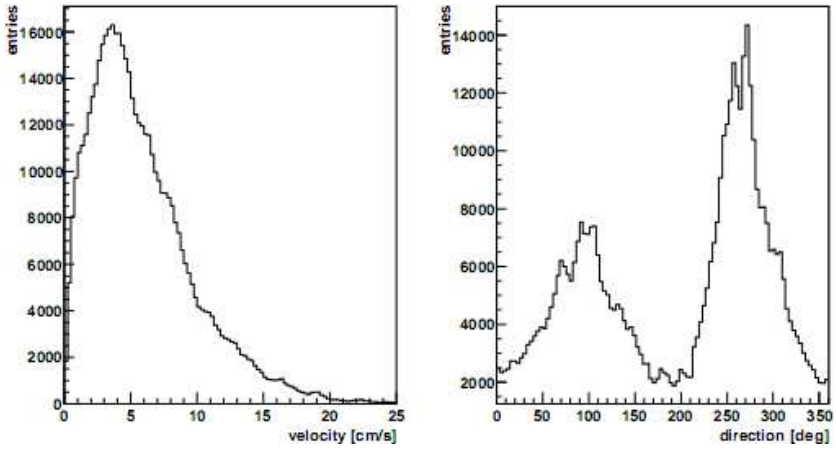

Figure 3.22: Distribution of sea current speed (on the left) and its horizontal direction (right).

The Onshore calibration of the OMs offset (Figure3.24) is done in a dark room to eliminate unwanted light sources. A controlled laser beam is sent to the OM as seen in figure 3.23 . The offset is calculated in reference to the first OM of the first floor.

The in situ calibration is actually a set of three different calibrations done on the sea bed.

- Using the LED beacons[93] the OM offset can be recalculated (Figure 3.24) using these beacons that flashes light at $\lambda = 470$ nm. These beacons exist on floors 2, 9 , 15, and 21 of each line. This is done by flashing the LED beacons and measuring the time differences of the signal among the different OMs and a reference OM. However, since the first LED beacon is on the second floor of each line, the offset can not be measured for the first floor as the light from the LED is emitted upwards, this is solved using the laser beacons.

- Using the laser beacon[93] on the BSS of lines 8. This laser beacon which flashes laser beams at $\lambda = 532$ nm can calculate the inter-line offset between all lines and line 8. This is done as well by flashing the laser beacon and measuring the time differences of the signal among the different lines. In addition, the laser beacon can measure the OM offset for the first floors of each line as as the laser beacon is placed below the first floor.

- ^{40}K which occurs naturally in sea water, it is a radioactive isotope of Potassium. The decay of ^{40}K can produce photons which can help in an indepen-

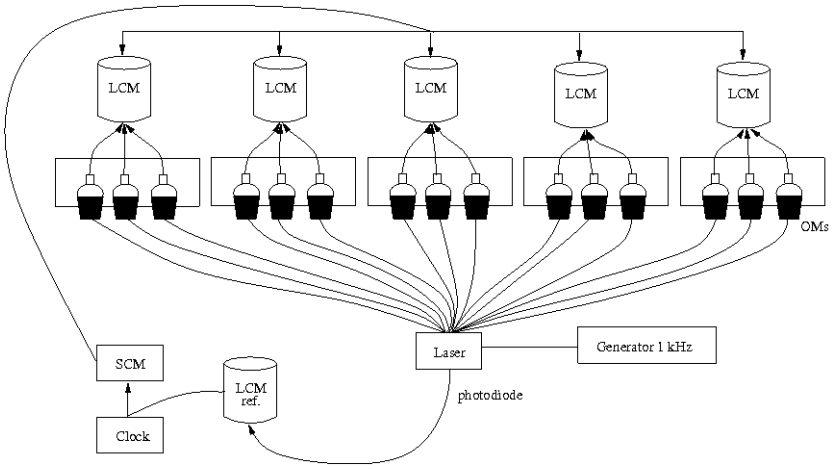

Figure 3.23: OM time offset calibration setup as done in a dark room.

dent way calibrate the arrival time of photons (Figure 3.25). This is done by studying hits coincidence on two adjacent OMs (Figure 3.26).

The various methods used to do the time calibration of the detector achieve an accuracy less than 1 ns.

Angular resolution

The eventual precision of ANTARES is measured by the value of the angle between the trajectory of the neutrino and the reconstructed muon trajectory which is very much dependent on the time calibration and knowing the precise location of every OM, in addition to depending on the kinematics of $\nu \rightarrow \mu + X$.

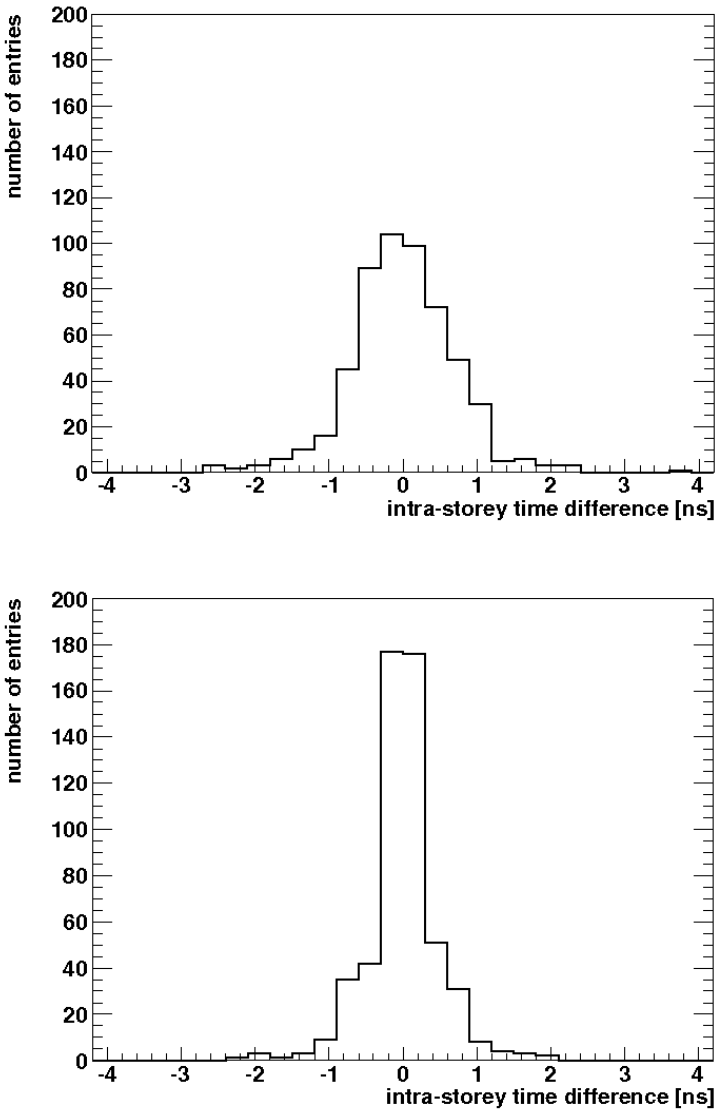

Figure 3.24: Time offset among OMs in the same storey for one of the lines using the time offsets measured onshore (up) and in situ (down).

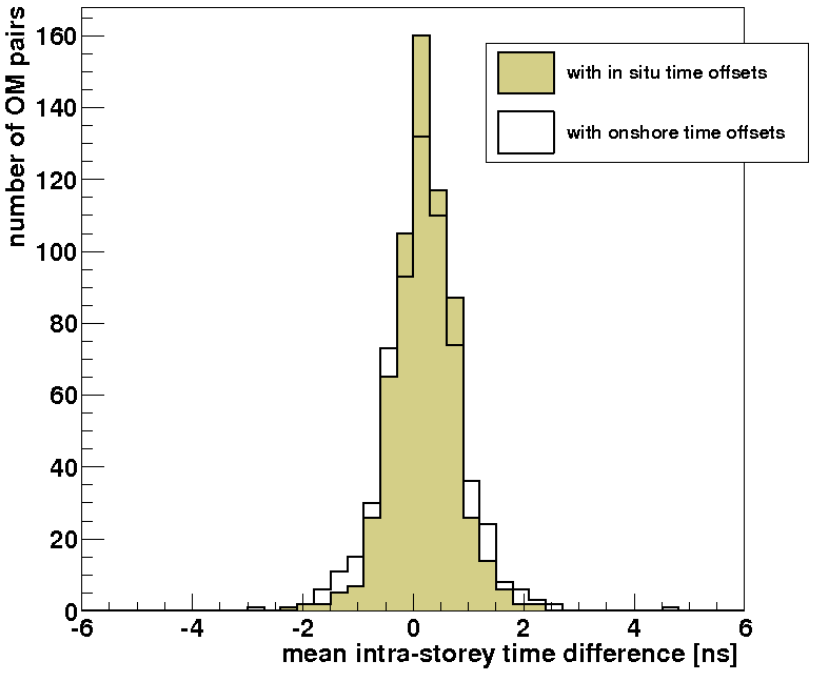

Figure 3.25: Comparison of the distributions of mean intra-storey time differences from ^{40}K and onshore.

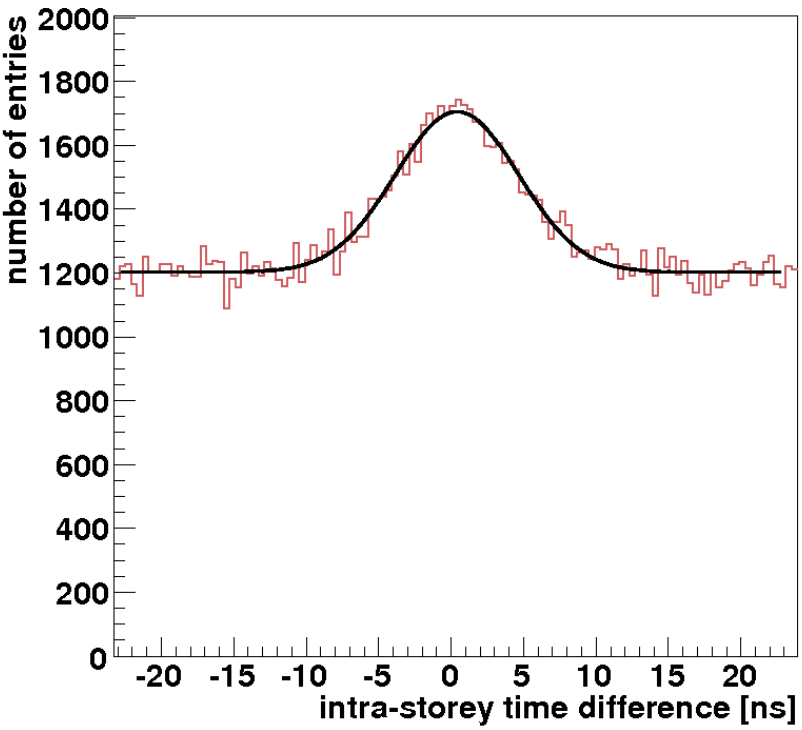

Figure 3.26: Distribution of time differences for background hits on two adjacent OMs. The peak is due to ^{40}K hits detected in coincidence. The data have been fitted to a sum of a Gaussian distribution and a flat background from random coincidences.

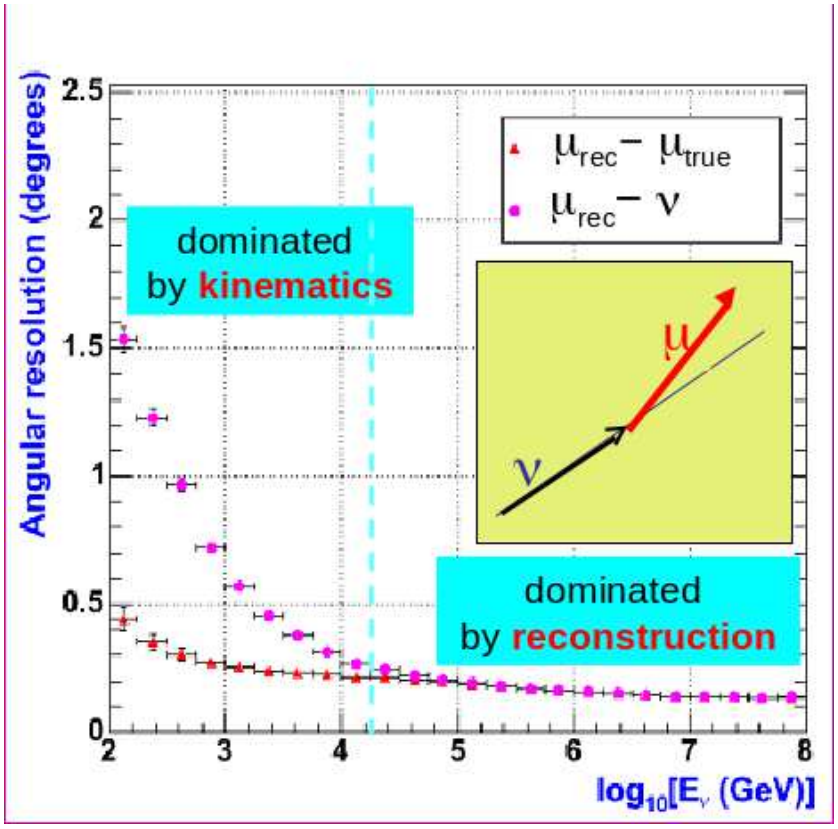

Figure 3.27: Median angles between neutrino and the muon and its reconstructed trajectory as a function of energy of the neutrino.

3.2.1.3 Status of the detector

The construction of the detector started in 2006 when the first line was deployed. But this was preceded by the foundation period in 2001 and 2002 where the electro-optical cable was laid out between the detector site and the onshore station along with the installation of the junction box. The construction was over in 2008 when the last two detector lines were installed. Nevertheless, the detector started collecting data since the installation of the first line, then through 2007 when the fifth line was installed and continued to do so throughout the installation of the remaining seven lines. The detector passed through periods where not all lines were operational or some were not yet installed as previously mentioned, these periods can be seen in table 3.2. The detector has been working with full capacity (12 lines) since 2008.

Line number	Connection Date	Maintenance
1	02/03/2006	-
2	21/09/2006	-
3	27/01/2007	-
4	29/01/2007	03/03/2008 - 28/05/2008
5	29/01/2007	-
6	05/12/2007	27/10/2009 - 03/11/2010
7	06/12/2007	-
8	06/12/2007	-
9	07/12/2007	02/06/2009 - 03/11/2010
10	06/12/2007	07/01/2009 - 06/11/2009
11	25/05/2008	-
12	28/05/2008	12/03/2010 - 13/11/2009

Table 3.2: Connection time and maintenance period for each ANTARES line.

3.2.1.4 Performance and characteristics

ANTARES' location in the upper hemisphere allows it to look at interesting parts of the southern sky (Figure 3.28), one is the galactic center which is a very good candidate for detection of WIMPs induced neutrinos. This is due to the fact that ANTARES is not located on the northern pole but at a lower latitude, the benefit of the location is access to a larger portion of the sky when compared to ICE-CUBE (Figure 3.29). However, the downsize is that visibility of the sky is not constant in the galactic coordinates plan and it is dependent on rotation of earth around the Sun. In figure 3.30 we can see the effective area of the full detector for upgoing neutrinos, the effective area increases with energy, however it is not always increasing, as it is dependent on the direction of the neutrino. The closer the neutrino track to the vertical axis the greater distance the neutrino has to travel through Earth (2*R_{Earth}) before interacting. However, in the low energy regime (Figure 3.31) where we would expect to see a dark matter neutrino signal no such problem exists since the decrease in the effective area starts around 100 TeV for neutrinos with nadir angle below 60°.

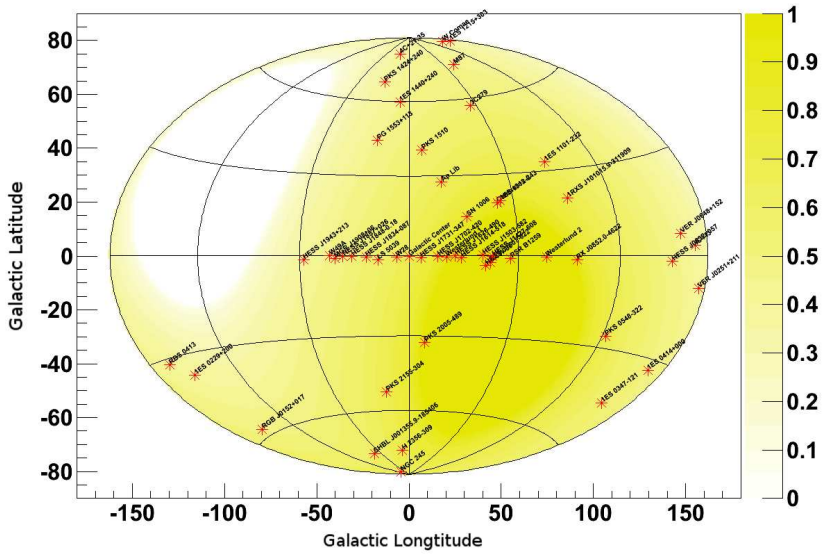

Figure 3.28: ANTARES visibility of the sky in galactic coordinates with a list of probable cosmic neutrino sources.

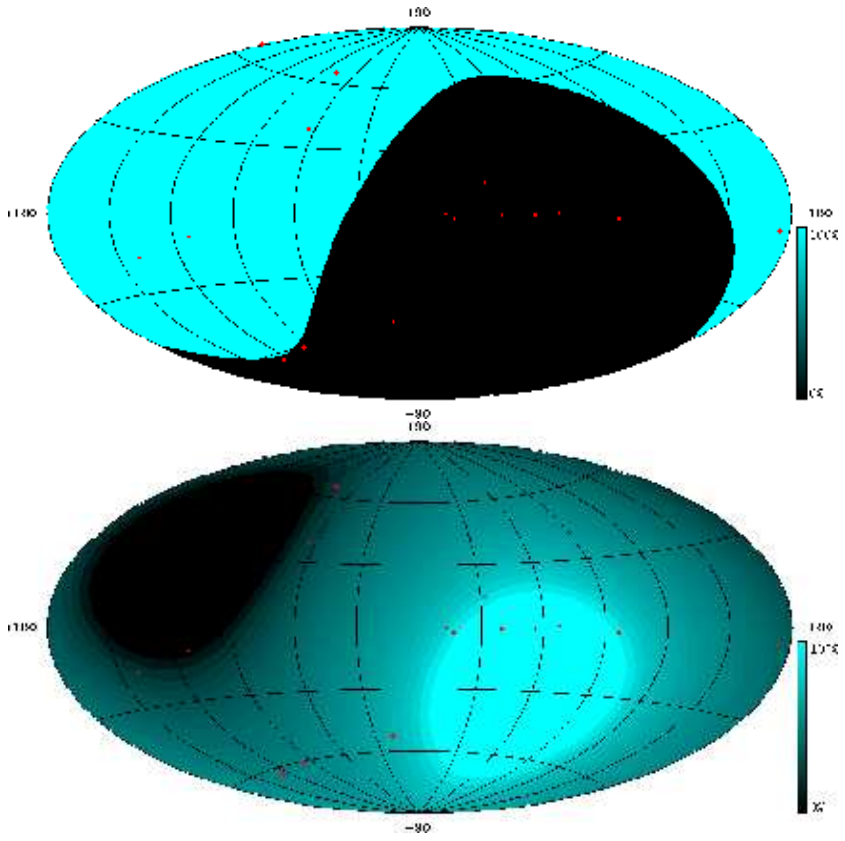

Figure 3.29: Comparison between sky visibility in galactic coordinates of ICE-CUBE (left) and ANTARES (right).

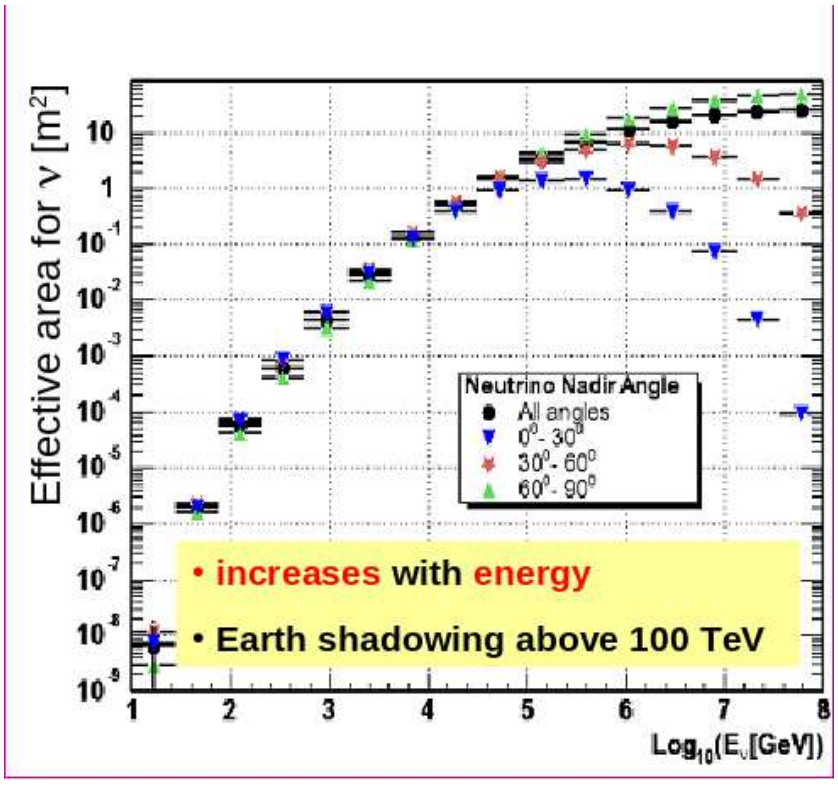

Figure 3.30: Effective area at trigger level for the neutrinos as a function of Log_{10}(neutrino energy).

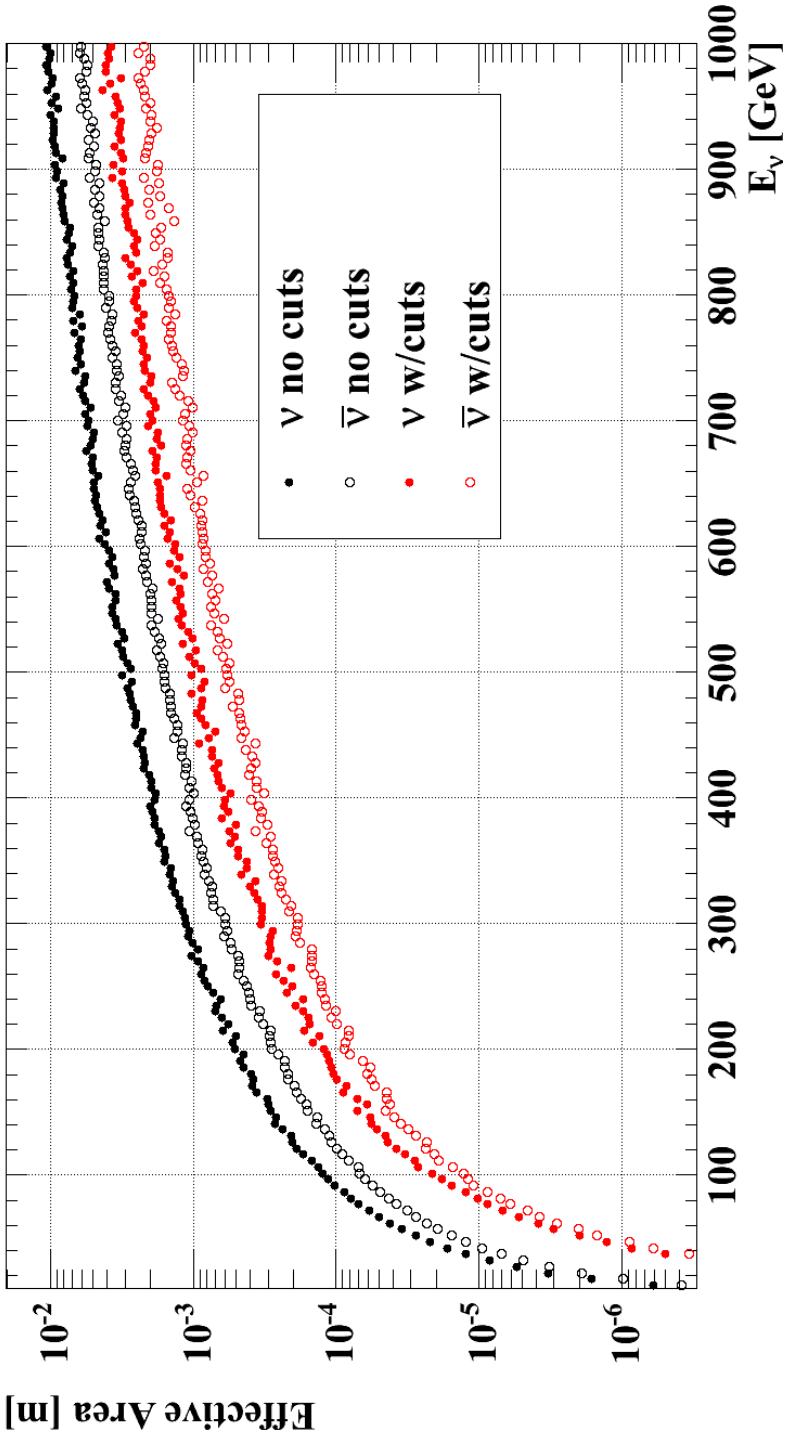

Figure 3.31: The effective area for $\nu/\bar{\nu}$ with and without quality cuts in the low energy regime.

Chapter 4

Monte-Carlo & Data

In this chapter the data acquisition is discussed followed by how each event is reconstructed. And then how the background is simulated.

4.1 Data acquisition

The acquisition of data[94] is divided into frames, each frame is 104 ms long. After the data are collected from the detector they are then sent to an offshore computing center (located in Toulon, France) where each frame is sent to a dedicated processor to minimize the congestion. However, not all frames are sent but only when the L0 hardware trigger has been triggered. L0 trigger in reality represents a threshold of 0.3 photo-electron (p.e) of a hit on the PMT, below this value the electrical noise of the PMT dominates the signal. If L0 is triggered then on the offshore station a series of trigger algorithms (will be explained in 4.1.2) are applied to the frame and if any eventis found then the frame is saved on a run file. The process continues until the size of this file reaches a size of 2 GB. Depending on how many trigger algorithms are applied, a single run file can contain from 1 hour and up to 3 hours of data.

4.1.1 Optical background

While the depth of ANTARES ensures that no light coming from the Sun reaches the detector the sea bed is not in total obscurity[95]. As previously mentioned the decay of ^{40}K[96] can produce photons (eq 4.1 and 4.2) which can be detected by ANTARES OMs. In the case of eq 4.1 the produced electron can be energetic enough to produce a Cherenkov effect in water. The average decay rate of ^{40}K is stable over time and produce a constant rate of hit on the OMs of the order of

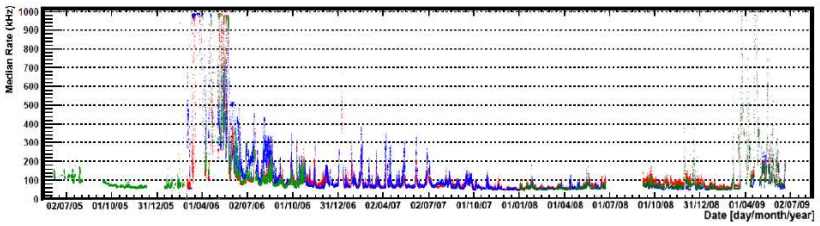

Figure 4.1: Median counting rate of OMs as function of time.

30 ± 7 KHz. However the typical ANTARES single OM counting rate is 55 KHz as see in figure 4.1.

From the figure 4.1 we can extract two values that can help us determine the quality of the run (section 4.1.3). These two variables are the baseline and the burst fraction. The baseline is defined as the flat part of the distribution, and for the burst fraction it is defined as the percentage of time (during one run) where the counting rate is higher than 1.2∗baseline.

$$^{40}K \rightarrow ^{40}Ca + e + \bar{\nu} \tag{4.1}$$

$$\begin{aligned} ^{40}K + e &\rightarrow ^{40}Ar^* + \nu \\ ^{40}Ar^* &\rightarrow ^{40}Ar + \gamma \end{aligned} \tag{4.2}$$

Another contribution to the optical background is bioluminescence[95]. Moreover it is not constant as ^{40}K is, bioluminescence activity is correlated with sea current and varies with seasons, the peaks on figure 4.1 are due to time-averaged bioluminescence activity around ANTARES.

On figure 4.2 we can see the typical counting rate ($\sim$ 100 KHz) registered on the OMs. The rates are usually constant but bioluminescence activity causes bursts as seen.

ANTARES registers an average of 900 neutrinos per year (Figure 4.3). In addition to that if we look at figure 4.4 we can see that the number of neutrinos detected per month on average is season dependent, the reason for this is bio-activity in the vicinity of the detector in Spring and Summer. The full 12 lines detector has a rate of 10 atmospheric muons per second, and 5 neutrinos per day.

4.1.2 Triggers

After each data frame is collected from the detector and sent to offshore station, a number of trigger algorithms can be applied. The most important ones are listed bellow:

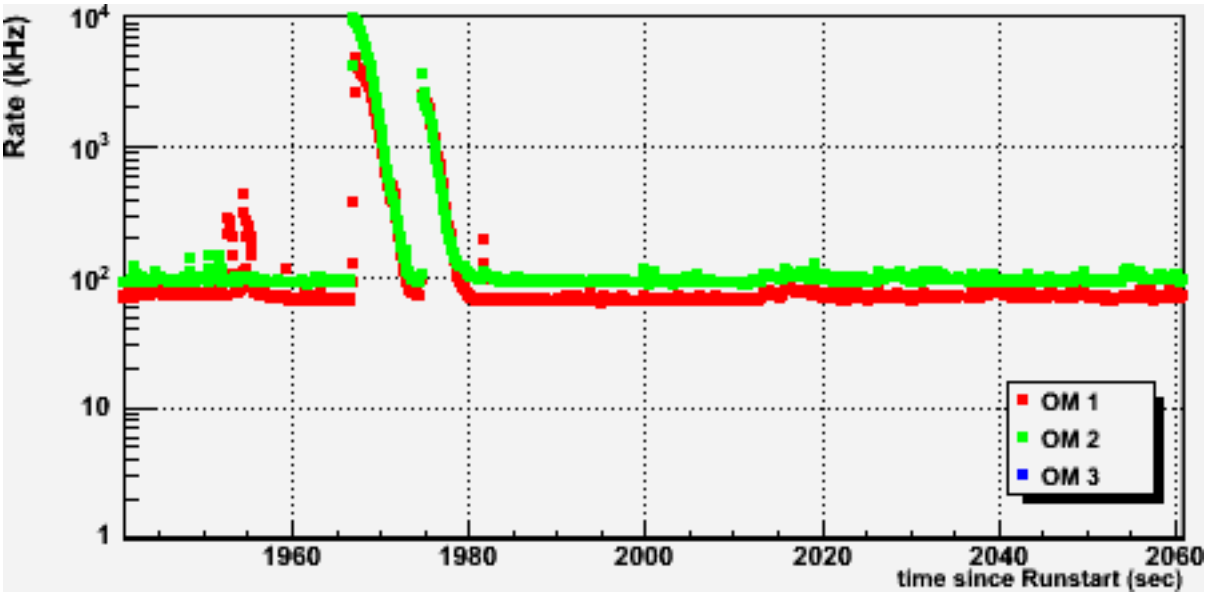

Figure 4.2: Typical rates on OMs on a floor. The flat part represents the baseline, while the peaks are bursts due to bioluminescence.

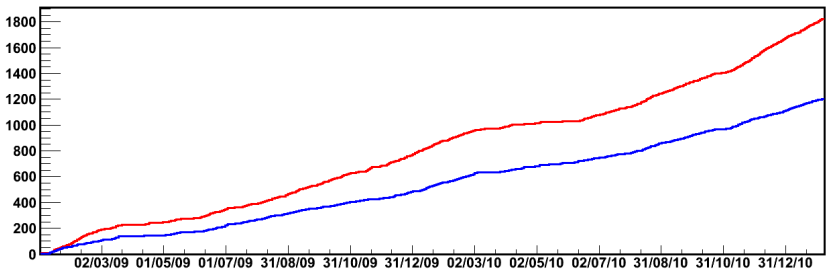

Figure 4.3: Cumulative number of online reconstructed up-going neutrinos (with BBFit(section 4.1.4.1) and basic quality cuts) between January 2009 and December 2010. Red is events with number of lines greater than one and blue is number of lines that is equal to one.

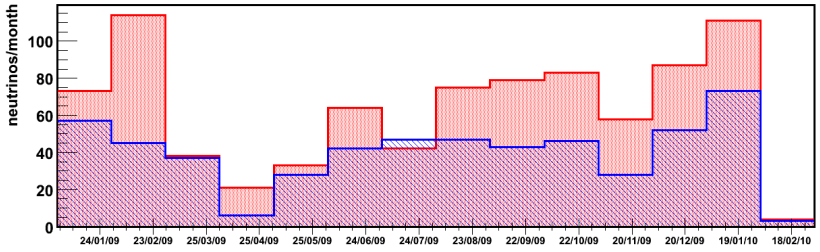

Figure 4.4: Average neutrino events per month. Red is events with number of lines greater than one and blue is number of lines that is equal to one.

L1

A L1 trigger is one of two conditions:

- If the charge of the signal registered by the PMT passes 3 pe (or 10 pe as it depends on the noise condition).
- If the time difference between two L0 hits on two different PMT from the same storey is less then 20 ns.

T3

A T3 trigger is a collection of L1 triggers, based on adjacent or next-to-adjacent stories during a certain time window. This time window is 80 ns when the L1 hits are between two consecutive stories and 160 ns between two stories separated by one stories which records no L1 hits. The typical rate of T3 in normal conditions is <20 Hz.

3N

This trigger looks for a cluster of 5 L1 triggers in a window that corresponds to a muon track going trough the detector. The typical rate of 3N in normal condition is <10 Hz.

4.1.3 QualityBasic

QualityBasic is an effort to estimate the quality of data. the QB flag is a variable assigned to each run to give an estimate of how good the acquired data is. This flag can have up to 5 values [0, 1, 2, 3, 4] :

QB=1

The QB=1 flag is given when :

- No problems at all with the frames, or frame indexing.
- If there is less than 2% synchronization problems in the timeslices (or frames).
- If the difference between run duration (stop time - start time) and N_{frames}* FrameTime is smaller than 450 s.
- A muon rate which computed with the 3N trigger is between 0.01 Hz and 100 Hz

QB=2

All conditions for QB=1 and at least 80% of the OMs were active during the run.

QB=3

All previous conditions for QB=2 , and if the OMs baseline $\leq$120KHz and Burst-Fraction $\leq$40%.

QB=4

All conditions for QB=2 and if the OMs baseline $\leq$120KHz and BurstFraction $\leq$20%.

This criteria will be used later to make a selection on the runs that will be used in the analysis.

4.1.4 Event reconstruction

The reconstruction of muon's direction is done via reconstruction algorithms, we'll go through two of them which will be later used in the analysis. The fit achieved by these two algorithms is based on arrival time of hits. Eventually a more thorough comparison between these two methods will be explored in the next chapter.

4.1.4.1 BBFit

Basic characteristic of BBFit[97]:

1. Detector lines are assumed to be vertical & the distance between the optical modules and the center of the floor is reduced to 0

2. All hits on the same floor are merged

3. χ^2function is used to fit the hits into a muon track (eventually and M-estimator is used to improve the fit)

The end result is that this reconstruction algorithm is a fast and simple algorithm this is mainly due to (1) and (3). Additionally we have a loss of information on the Azimuth direction of events that have all of their hits on one line ((consequence of (2)). Finally, this strategy has better effective area for low energy events (below 150 GeV) when compared to other strategies (more comparison will be shown in the analysis chapter).

4.1.4.2 AAFit

Basic characteristic of AAFit[98]:

1. Full use of the dynamic geometry of the detector

2. Full simulation of the detector electronics

3. Implementation of light scattering PDF in water

4. Multi-stage fitting, utilizing a χ^2, an M-estimator and a maximum likelihood when fitting the hits into a muon track

This strategy is precise and can achieve an angular resolution of 0.3°degrees at $E_\nu = 1$ TeV, it is very susceptible to bioluminescence and very demanding computationally. However, when compared to other strategies this algorithm achieve a better angular resolution, and a better effective area for high energy events (above 200 GeV).

4.2 Monte-Carlo simulation chain

In order to simulate our background to the dark matter events, first we must identify them. Basically all physics background comes from one single source "Cosmic Rays". Events induced by cosmic rays fall into two categories:

Atmospheric Muons

These are muons created by cosmic rays when they hit the upper atmosphere. If the muons are energetic enough they can travel large distances (up to 100 km). So these muons travel the atmosphere going down to the detector. However the majority of these events are already removed simply by selecting up-going events.

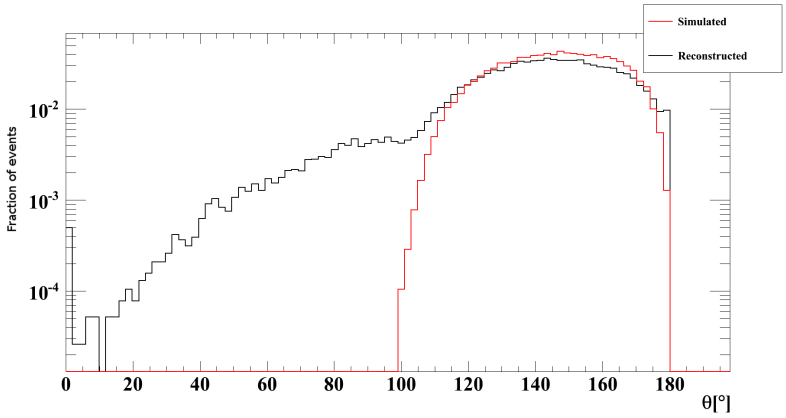

Figure 4.5: Percentage of muons simulated/reconstructed as function of the zenith angle θ. $\theta = 0^\circ$ is the nadir, $\theta = 90^\circ$ is the horizontal and $\theta = 180^\circ$ is the zenith. This distribution is before any cuts, and reconstructed using the BBFit reconstruction method.

Some of these down-going muons are reconstructed inside the detector as up-going (Figure 4.5) due to several factors such as:

- The event is actually a down-going multi-μ event but fitted as an up-going electron event.
- Hits from the optical background.
- Choice of the reconstruction strategy but this has a more limited effect.

Atmospheric Neutrinos

At the same time the above mentioned muons are created, $\nu_\mu$are being simultaneously created by the same process, however these neutrinos rarely interact as they go down from the upper atmosphere, but they do continue through the Earth and interact exactly just as a neutrino signal would. However, it is important to note that ANTARES is dominated by atmospheric muons, in figure 3.8 we can see that the atmospheric muons' flux is 6 orders of magnitude higher than the neutrinos'.

Simulation

The simulation of these two sources is divided into many steps, and uses different software packages.

We will go through all of them starting with the special steps concerning each source.

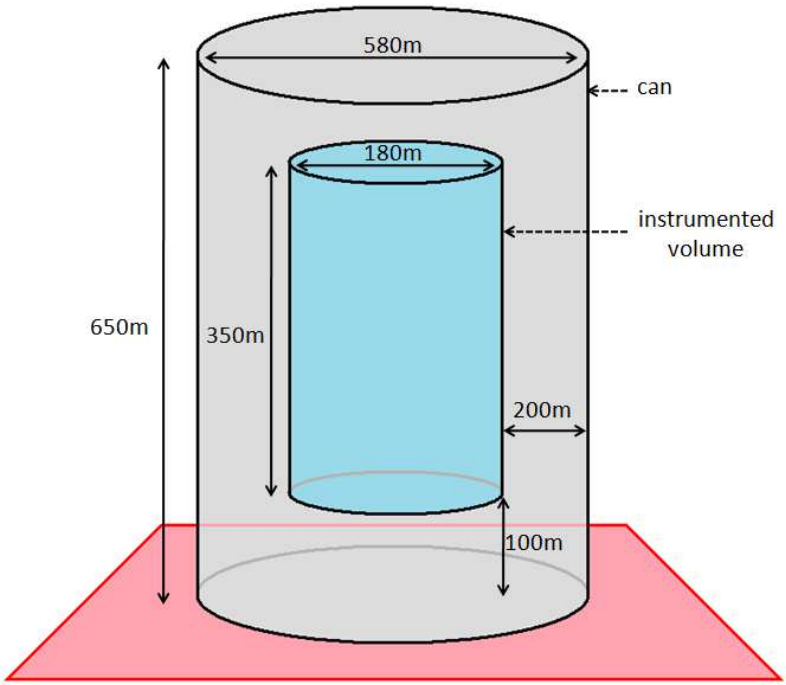

Figure 4.6: The can.

4.2.1 Neutrino simulation

The simulation of atmospheric neutrinos starts with GENEHN ([88] & [99]) which has the role of generating the initial neutrino and then its interaction with matter, followed by GEASIM[100] which handles the hadronic showers created with the simulated neutrinos.

4.2.1.1 GENHEN

GENHEN (GENerator of High Energy Neutrinos) is a neutrino Monte Carlo simulator which simulates according to an input provided by the user the distribution of muon's induced neutrinos on and inside a surface that surrounds the detector. This surface is named "can" (Figure 4.6), it represents the surface of a cylinder surrounding the detector. If the detector is thought to be of cylindrical shape, the radius of the can is the radius of the detector plus ~ 3 times the absorption length of the Cherenkov light (the absorption length will be defined later in section 4.2.3).

The user can select through input data cards the parameters of the simulation, we'll list some of the most important of them:

- Number of neutrino event to be simulated

- Flavor of the neutrino to be simulated
- Energy range of the simulation
- Whether to do charged current interactions or neutral current interactions
- Choice of the parton model of interacting matter
- Model of neutrino interactions
- Neutrino flux (-1.4 for atmospheric neutrinos (insert reference to that number))
- Whether to generate isotropic neutrinos or from a point with a fixed declination in the RA-DEC coordinate system

After the user has selected the input parameter and the simulation is over, the output of the simulation is then parsed into an ASCII file.

4.2.1.2 GEASIM

GEASIM is a particle and shower Monte Carlo simulator based on GEANT, in the case of ANTARES the input is the files simulated previously with GENHEN. However it goes further than GENHEN, by simulating the propagation of showers and the eventual radiation produced by these particles.

4.2.2 Muon simulation

The simulation of atmospheric muons is done directly via MUPAGE[101]:

MUPAGE

MUPAGE (MUon GEnerator from PArametric formulas), as the name suggest it is an atmospheric muon Monte Carlo generator. They are not simulated using collisions between cosmic rays and the atmosphere, but rather using parametric formulas for the expected muon flux at the detector level. MUPAGE takes as input many variables, the most important of them:

- Position of the detector below sea level
- Size of the can
- The θ range of simulation
- Energy range of the muons

- Multiplicity range of the muon bundle
- Water proprieties such as the density, and optical absorption length

After the simulation has ended, as for GENHEN and GEASIM, the output of the simulation is parsed into an ASCII file.

CORSIKA

There is another way of simulating atmospheric muons, this is done via simulating interactions between cosmic rays and The Earth's atmosphere. The main difference between CORSIKA[102] and MUPAGE, is mainly statistics, CORSIKA is more demanding computationally while MUPAGE can offer for the same CPU time a much higher statistics.

4.2.3 Photon propagation

Once the muons are simulated they have to be propagated. This requires the simulation of the light emission as well to their propatgation in water. These emissions include Chernekov radiation from muons and bremsstrahlung from electromagnetic showers . This is done with the KM3 ([**?**])package. In water two effects dominates the propagation of light.

Absorption

Sea water is a transparent material however it is not 100% transparent. Many photons after being generated by the muon get absorbed in water. We define an absorption length of water as the average distance for which the fraction of photons that survives is equal to e^{-1}($\sim$36.7 %). In ANTARES sea water that distance is *sim* 60 m for photons with $\lambda = 473$ nm.

Scattering

Scattering affects the direction of a photon. We can as well define an average distance called scattering distance where a fraction of photons that is equal to e^{-1}does not get scattered, this distance in sea water is *sim*270 m for photons with $\lambda = 473$ nm.

KM3

In KM3 package these two effects are not simulated directly since doing so for each photon and from each muon it would be computationally unfeasible. However, this is done via "photon tables". These tables are pre-generated, and they

give the distribution of arrival time as a function of the direction, and orientation of photons when they hit the PMT at different positions. In addition to the simulation of visible light, KM3 deals as well with the propagation of muons in the medium and the related physical process.

4.2.4 Trigger and optical background simulation

After the propagation of photon from each event has been simulated, the next step is to simulate two things at the same time. First there is a need to simulate the optical background coming from two sources, bioluminescences and K_{40} . The second part is essentially a simulation of how the detector will respond to an event, this is essentially a simulation of the electronics such as the PMTs, and the ARS motherboards. This is all done with a software package called TriggerEfficiency.

Reconstruction

After the simulations have been treated with TriggerEfficiency the Monte Carlo output has the same format as data, so they can be treated as such and have the events reconstructed. And as previously mentioned the two important strategies are AAFit and BBFit, which we will use to reconstruct the events.

Chapter 5

Dark Matter search in the direction of the SUN with 2007-2008 data

In this chapter the analysis and the results obtained from looking at the 2007-2008 data sample will be presented.

5.1 Dark matter neutrino spectrum

In order to analyze the possibility of finding a dark matter neutrino signal, we must first be able to estimate the (anti-)neutrino spectrum coming from WIMP annihilation in the Sun. The spectra were obtained using WIMPSIM[86]. WIMPSIM is defined as:

> A WIMP (Weakly Interacting Massive Particle) Monte Carlo for neutrino telescopes. This code calculates the annihilation of WIMPs inside the Sun or the Earth, collects all the neutrinos that emerge and let these propagate out of the Sun/Earth to the detector including neutrino interactions and neutrino oscillations in a fully consistent three-flavor way. This is done in an event-based scenario which is particularly suitable for interfacing to a neutrino telescope Monte Carlo.

The neutrino spectrum coming from dark matter auto-annihilation is dependent on the mass of the particle, and it changes between hard and soft spectrum depending on which is the dominant annihilation channel. WIMPSIM offers range of Dark Matter masses such as:

$50GeV$, $80.3GeV$, $91.2GeV$, $100GeV$, $150GeV$, $176GeV$, $200GeV$, $250GeV$, $350GeV$

$500GeV$, $750GeV$, $1000GeV$, $2000GeV$, $5000GeV$

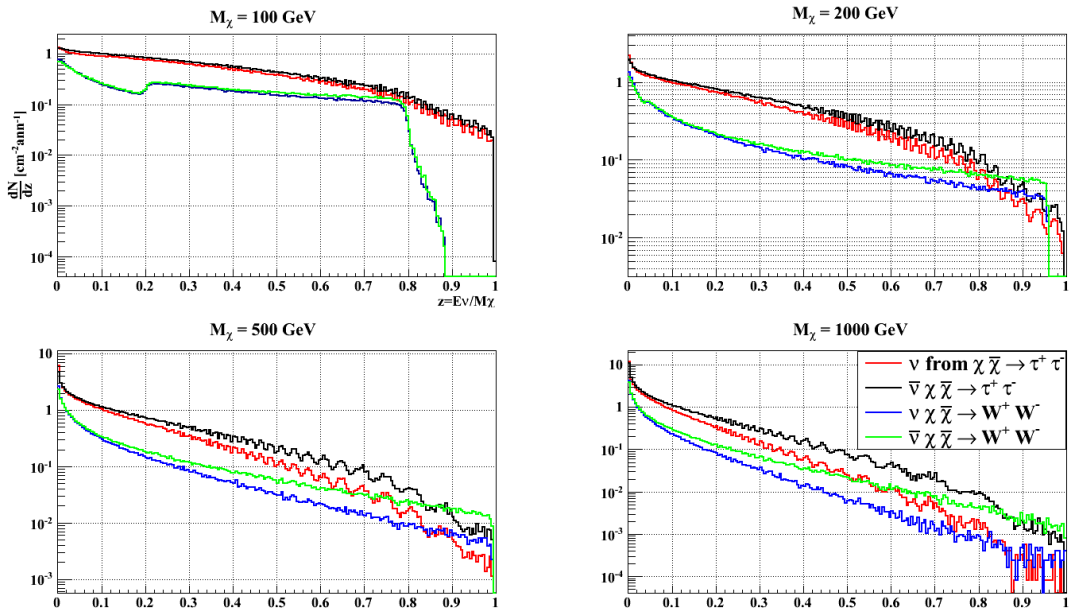

Figure 5.1: Dark Matter neutrino differential flux showing the difference between $W^+W^-$and $\tau^+\tau^-$ annihilation channels.

The softest neutrino flux is due to $\chi\bar{\chi} \to b\bar{b}$. The hard flux has been studied with two different channels. In most general models the hardest flux is produced by $\chi\bar{\chi} \to \tau^+\tau^-$ (Figure 5.1). However assuming the SUSY models it is common to use fluxes produced by $\chi\bar{\chi} \to W^+W^-$ since in such models the branching ratio to $\tau^+\tau^-$ is usually suppressed in comparison with W^+W^-. However since all $\nu_\mu + \bar{\nu}_\mu$ spectrum are normalized to 1 we would expect to see small differences between τ and W annihilation channels when calculating the limits to neutrino fluxes.

It is interesting to note that by examining Figure 5.1 , and 5.3 we notice that the $\bar{\nu}$ flux is higher than the ν. This is due to the fact that ν have higher interaction probability with the Sun's matter than $\bar{\nu}$, resulting in larger absorption of ν than $\bar{\nu}$ inside the Sun. Another remark is that we can see the effect of the neutrino oscillations on the fluxes. Nevertheless there is no reason to assume that these oscillations can be detected with the current detector.

Another note to be taken into consideration is that the absorption for neutrinos with energies above 1 TeV in the Sun is considerable, we would expect to see that the neutrino spectrum from the annihilation of WIMPS with masses higher than 1 TeV has some sort of high energy cutoff as see in figure 5.2, so we would expect that the limits of Soft and Hard spectra converge at very high WIMP masses (above 5 TeV).

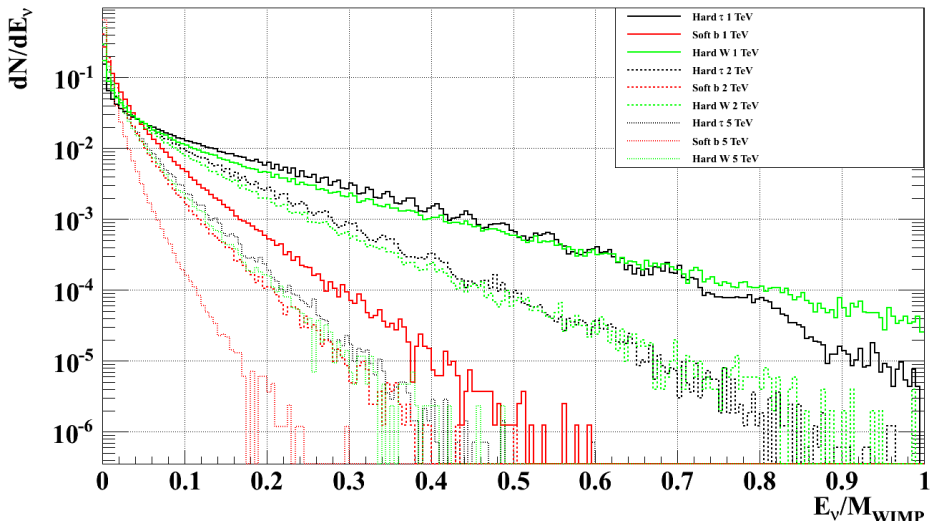

Figure 5.2: Annihilation spectrum for $\nu_\mu + \bar{\nu}_\mu$ from WIMPS with masses of 1, 2, 5 TeV normalized to one.

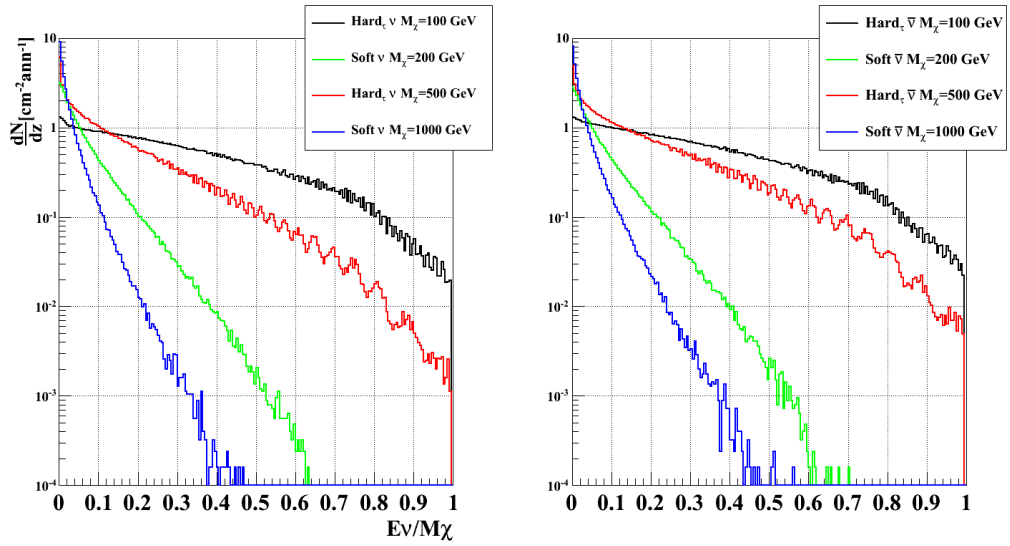

Figure 5.3: Differential fluxes for the Dark Matter models shown as examples in this paper. We use two soft models representing Mχ= (200, 1000) GeV models, and two $hard_{\tau^+\tau^-}$ representing Mχ= (100, 500) GeV models.

The spectrum obtained via WIMPSIM will be used later in the 2007-2008 and 2007-2010 data analysis to estimate a signal as a function of the soft/hard spectrum and the WIMP mass.

5.2 Data selection

The data that were used in the analysis is composed of the 2007-2008 silver runs given by the official data quality list(with quality basic >2) that includes the 3pe and 10pe higher threshold of the 5,9,10, and 12 lines configuration of the detector. This results in 2692 runs, for a total livetime of 293.4 days.

5.3 Reconstruction strategy

The selected reconstruction strategy for this analysis was BBFit. The output of BBFit algorithm is stored in a ROOT file containing more then 30 variables, but in the course of this analysis only a few will be used:

- tchi2 : It is the $\chi^2$of the Cherenkov-like fit of the event. The hits on the OMs of the track are fitted in corresponding to a Cherenkov light cone, tchi2 is a reflection of how good that fit was (after this section all references to χ^2 variable refers to tchi2).
- bchi2: It is the $\chi^2$of the bright point-like fit of the event. The hits on the OMs of the track are fitted in corresponding to a spherical light wave that are produced by a hadronic and electromagnetic showers, bchi2 is a reflection of how good that fit was.
- nhit: Number of hits used in the fit.
- nlines: Number of detector lines used in the fit.
- tcosth: Cos[zenith] of the fitted track.
- tphi: ϕ (azimuth) of the fitted track (variable is empty when the number of lines used in the fit is equal to one).

The output of BBFit also holds extra variables that are not an output of the algorithm itself, but will be used nevertheless in the analysis:

- prct: Cos[zenith] of the neutrino generated by Genhen.
- prphi: ϕ of the neutrino generated by Genhen.
- pre: Energy of the neutrino.

Livetime(days)	5 Lines	9 Lines	10 Lines	12 Lines
3HT	96.2	36.5	38.4	52.2
10HT	37.8	1.7	0.1	30.5

Table 5.1: List of different periods with the corresponding livetime.

5.4 Monte Carlo selection

As previously mentioned between 2007 and 2008 the detector went through the last phases of construction. The effect of this is that the behavior of the detector differs during these periods, for this reason we have more than one set of Monte Carlo, and in fact the set includes 8 different Monte Carlo each with a different livetime (Table 5.1).

Atmospheric neutrinos Monte Carlo for each period consists of two files, one for neutrinos and one for anti-neutrinos.

The simulation had the simulation parameters: Neutrino flux $\Gamma = -1.4$; Energy range: 10 GeV - 10^8GeV ; Isotropic simulation ;

Atmospheric muons Monte Carlo each period consists of only one file.

5.4.1 Dark matter Monte Carlo

The neutrino Monte Carlo generator GENHEN, has two modes for generating neutrinos. The point source mode, which just takes the source's declination and generates the signal neutrinos, and an isotropic mode which generates atmospheric neutrinos. Since the Sun has a variable declination $[-23°26^{'}, 23°26^{'}]$ there is no way to directly use GENHEN to simulate neutrinos coming from the Sun. So in order to create a Dark Matter neutrino MC we will use the atmospheric neutrino Monte Carlo files to select from them neutrinos coming from the Sun's direction.

For the 2007-2008 analysis the following neutralino masses were chosen:

50 GeV, 80.3 GeV, 100 GeV, 150 GeV, 200 GeV, 350 GeV, 500 GeV, 1000 GeV

And for the annihilation channels:

Soft channel: b^+b^-

Hard channel: W^+W^-

Hard channel: $\tau^+\tau^-$

The process goes as following:

- For each period of 5, 9, 10, 12 lines detector, 3pe, 10pe threshold we select the appropriate atmospheric (anti)-neutrino files.

- Take the start date of the first run in that period, and follow the Sun's sky position in Zenith Vs Azimuth for the first 24 hours after that date.
- Take the end date of the last run in that period, and follow the Sun's sky position in Zenith Vs Azimuth for the last 24 hours preceding that date.
- If the period includes a solstice, then the period is divided for two periods from the start date to the solstice and from the solstice to the end date.
- Any events found between these two boundaries are events that corresponds to positions that the Sun takes during that period (Figure 5.4). Events outside that region will be removed.
- If the period include a solstice as indicated before, any event that is found in the overlapping regions gets selected twice or more depending on how many regions overlap at that position.
- For different M_χ we remove events that have $E_\nu > M_\chi$. To make sure the most energetic neutrinos in our sample can actually be a product of WIMP annihilation.
- We apply for each spectrum the corresponding $\frac{dN}{dE}$ (Figure 5.3) to the remaining events by re-weighting the MC events via a convolution with the effective area of the detector.
- We end up with dark matter (anti)-neutrinos for each specific period (Figures5.5 & 5.6).

It is interesting to note that the resulting MC file has a different livetime from the one used to generate it. The area selected by this method does not represent a full year but only an area with the livetime of that period.

In Figure 5.5 we notice an effect where instead of having a smooth[1] event distribution, we find more events concentrated near the middle of the event distribution. This is due to the fact that during Autumn and Spring the Sun is found at exactly the same region of the sky. However what we see in Figure 5.6 is a slight variation of this effect, where the geometry of the detector creates privileged[2] directions in Azimuth (ϕ) where more events are reconstructed in these directions than others. No selection criteria were applied to Figures 5.5 and 5.6.

[1] Small variations are expected due to different number of reconstructed events between Summer-Autumn-Winter-Spring periods.

[2] These directions slightly changes whether there is 5, 9, 10, or 12 lines in the detector.

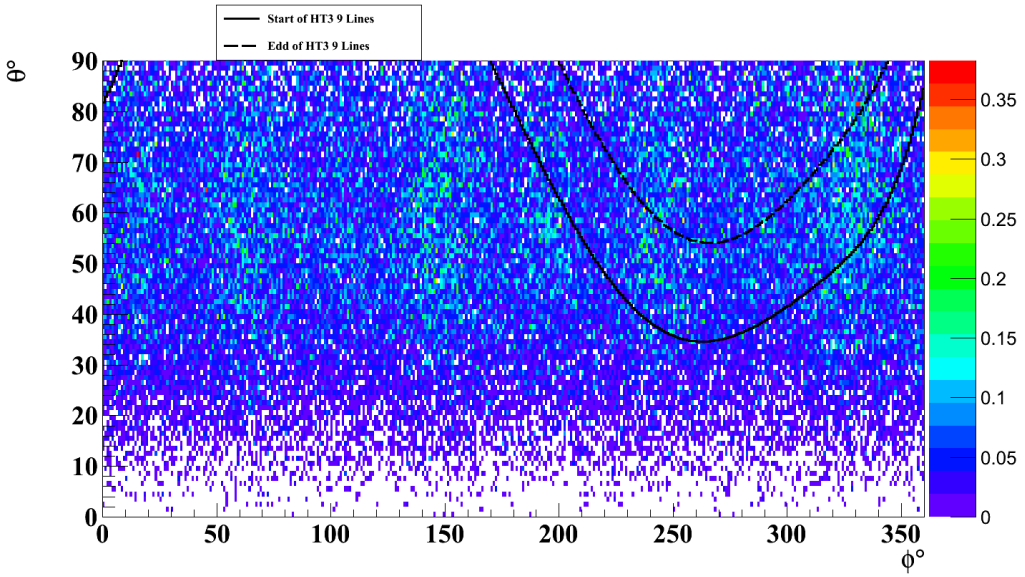

Figure 5.4: Monte Carlo Truth distribution of ϕ and θ for the atmospheric neutrinos. The two black curves represent the Sun's path in the (ϕ-θ) plane for the first 24 hours after the start of the 9Lines-3pe period, and the last 24 hours before the end of that period, events with $E_\nu > 1000$ GeV were removed to select neutrinos for the $M_\chi = 1000$ GeV hard$_{\tau^+\tau^-}$model.

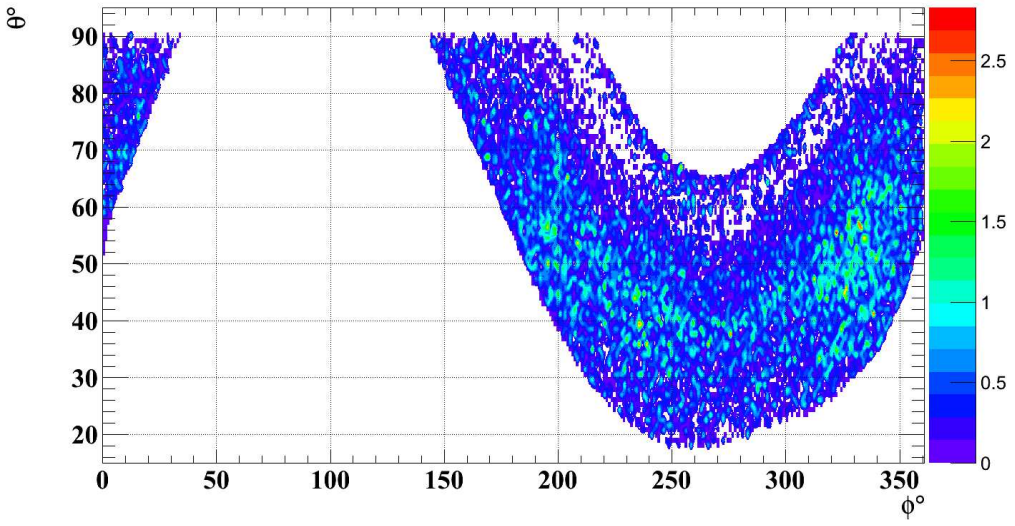

Figure 5.5: Dark Matter neutrino true distribution of ϕ and θ for 1000 GeV Hard.

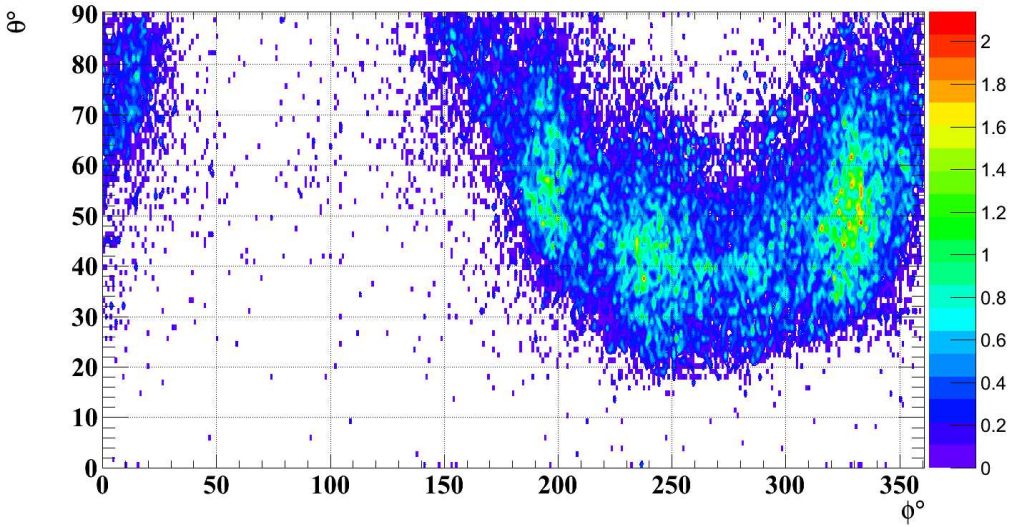

Figure 5.6: Dark Matter neutrino distribution of reconstructed ϕ and θ for 1000 GeV Hard

5.5 Data Monte Carlo comparison

In order to test the agreement between our data and Monte Carlo samples a set of preliminary cuts (basic quality cuts) are proposed on BBFit's variables:

- nhit > 5. BBFit χ^2Cherenkov fit requires exactly 5 hits to fit the track.
- nlines > 1. A cut on the number of lines used in the fit. If the number of lines used is equal to one, the fit doesn't converge on value for ϕ, so these events are removed for this analysis.
- tchi2 < bchi2. A cut that selects events that are better reconstructed as a muon generating a Cherenkov light cone than a shower bright point.
- tcosth > 0. A cut that selects up-going events.

After applying these preliminary cuts to our Monte Carlo and data samples we can see in figure 5.7 a comparison between data and Monte Carlo χ^2 distribution for the 3pe high threshold of the 5,9,10,12 Lines detector periods.

In figure 5.8 we can see a comparison between data and Monte Carlo χ^2 distribution for the 10pe threshold of the 5,9,10,12 Lines detector periods. A good agreement is observed except in the 9 lines period in the high Tchi2 area, a noticeable difference is observed between data and the atmospheric muons. However this does not influence the analysis, as we are more interested is removing events

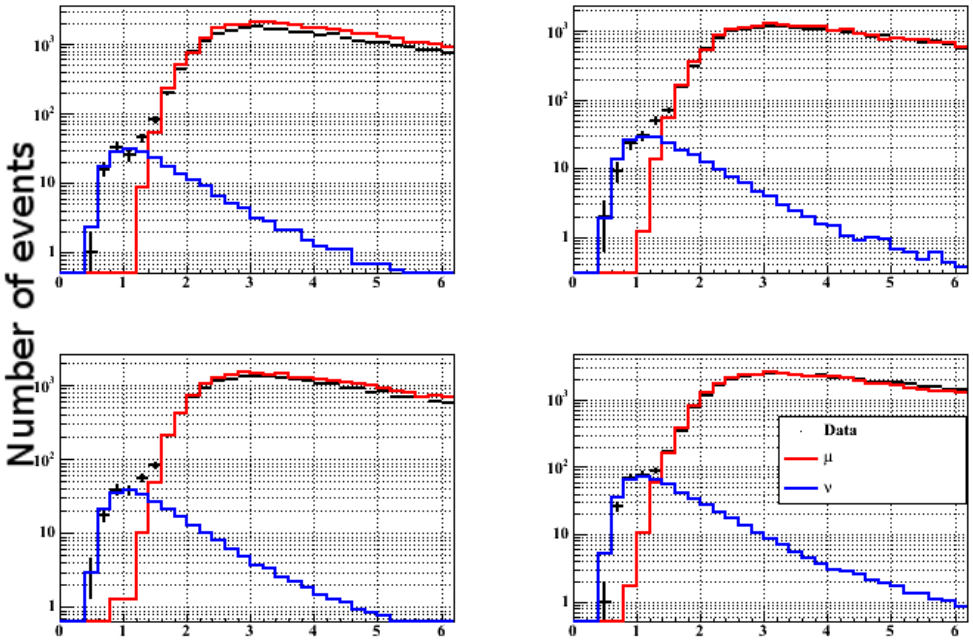

Figure 5.7: Tchi2 distribution for data and atmospheric neutrinos/muons for only the 3pe threshold of the 5,9,10,12 Lines detector periods. Upper left plot is for the 5 lines detector, upper right is for 9 lines, bottom left is for the 10 lines, and bottom right is for 12 lines. The Monte Carlo is normalized to the lifetime of the data taking.

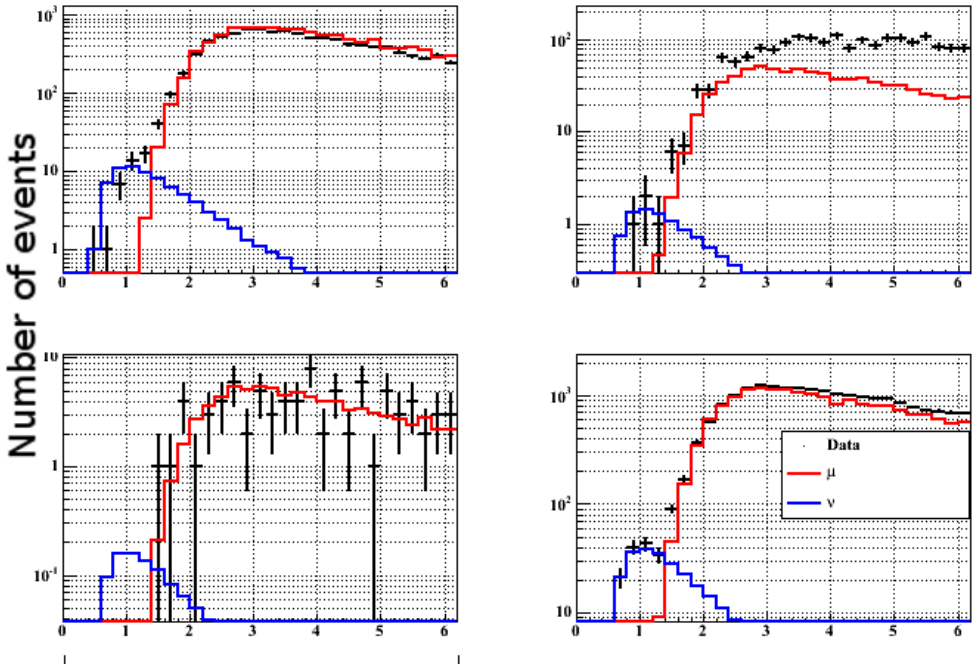

Figure 5.8: Tchi2 distribution for data and atmospheric neutrinos/muons for only the 10pe threshold of the 5,9,10,12 Lines detector periods. Upper left plot is for the 5 lines detector, upper right is for 9 lines, bottom left is for the 10 lines, and bottom right is for 12 lines. The Monte Carlo is normalized to the lifetime of the data taking.

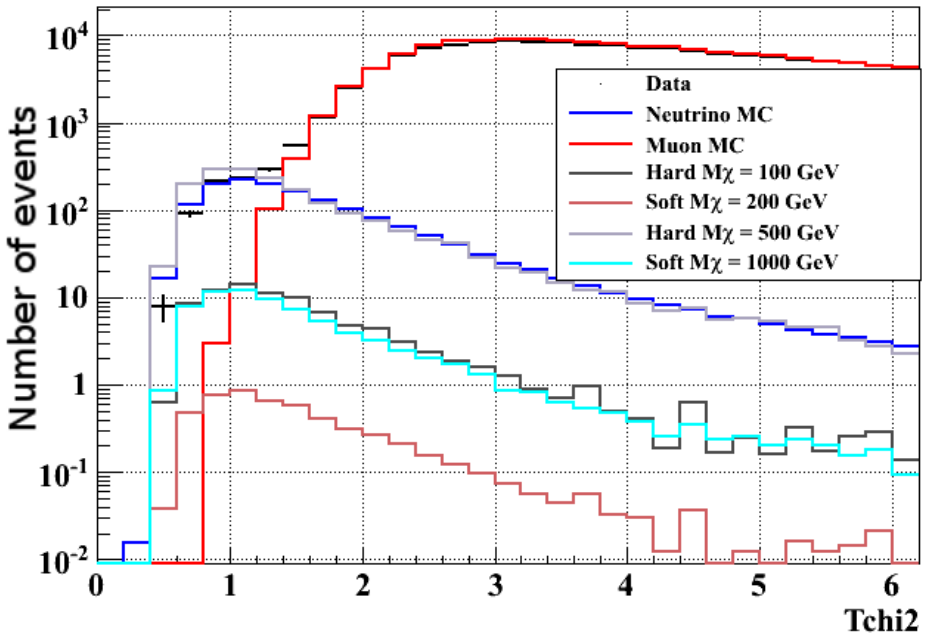

Figure 5.9: Tchi2 distribution for data, atmospheric neutrinos/muons and several Dark Matter models. The Distribution represents the 10pe-3pe 5,9,10,12 Lines periods combined. The muon and neutrino Monte Carlo are normalized to the lifetime of the data taking. The absolute normalization of the Dark Matter distributions are arbitrary.

with high χ^2. As for the 10 Lines period this disagreement is due to the fact that this period has only 2 data runs (about 2.4 hours of livetime), this effect is purely a statistical phenomenon. Finally we can combine all the different periods as seen in figure 5.9. Different WIMP annihilation spectra are included in this plot to study how would a Dark Matter neutrino signal manifest in the detector. Two important observations can be made, one is that we have a very good data Monte Carlo agreement for our whole livetime, and second is that Dark Matter neutrino signal behaves much like the atmospheric neutrinos. The second observation is not valid for all track distributions, this can be seen by looking at the Cos[Zenith] distribution in figure 5.10, this distribution was obtained by cutting loosely on Tchi2 (less than 2). Again we see in this figure that we have a very good data Monte Carlo agreement, but that the Dark Matter neutrino distribution is slightly different from the atmospheric neutrinos.

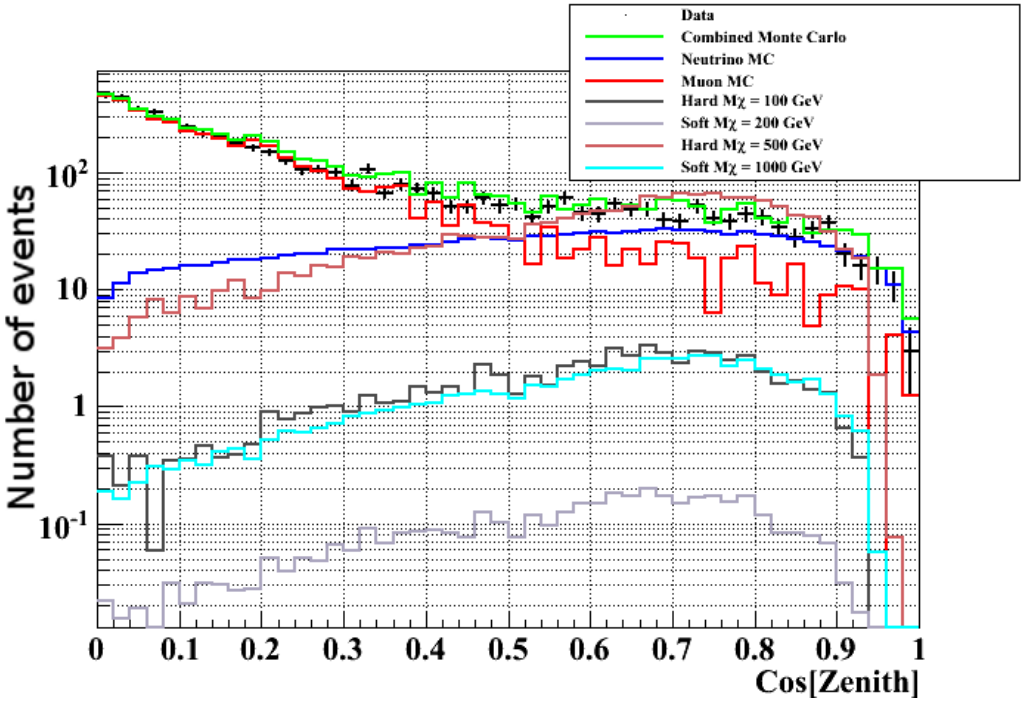

Figure 5.10: Distribution of Cos[Zenith] after a cut on Tchi2<2 for data, atmospheric neutrinos/muons and several Dark Matter models. The muon and neutrino Monte Carlo are normalized to the lifetime of the data taking. The absolute normalization of the Dark Matter distributions are arbitrary.

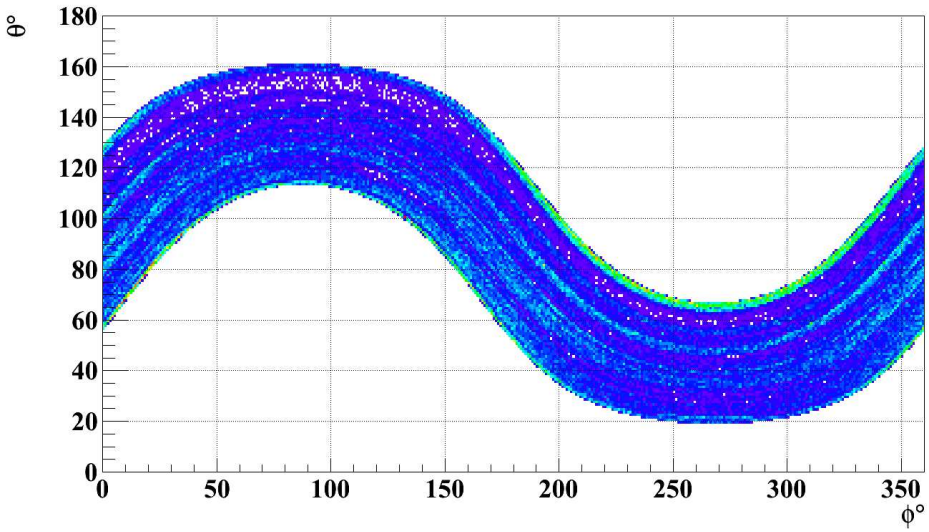

Figure 5.11: Sun's position taken at the arrival time of each event from data.

5.6 Background estimation

To estimate the background (which is due to atmospheric ν and μ events) from the data in the direction of the Sun, we scramble the data by simulating a fake Sun for each event. This method has the benefit of eliminating certain uncertainties arising from the use of the Monte Carlo. The scrambling is done by changing the arrival time of the each event[3], leading to a different position in the sky for the Sun at that given time. However this procedure used for choosing a different time is not done over all of the livetime, that means that each event is randomly given a new time from the same period it comes from and not from other periods. For example an event from the run number 33172 which belongs to the 3pe 9 lines period, will be randomly given a new time from another event belonging to the 3pe 9 lines period. The scrambling as it can be seen in figure 5.12 and 5.13 follows the distribution of the Sun's position as taken from the time arrival of data events quite well (Figure 5.11). The good agreement between data, scrambled data, and the μ & ν Monte Carlo can be seen in both the Zenith and Azimuth distribution of the Sun. We can look at the same distributions of 5.12 and 5.13 again but this time with a quality cut of χ^2<1.6 in figure 5.14, the agreement is again quite good.

Once the scrambling method had been verified, we can see in Figure 5.15 the estimation of the background noise in the direction of the Sun. The background is estimated as the number of scrambled events as a function of the half-angle of a

[3]The scrambling is done many times to increase the statistics of the scrambled sample.

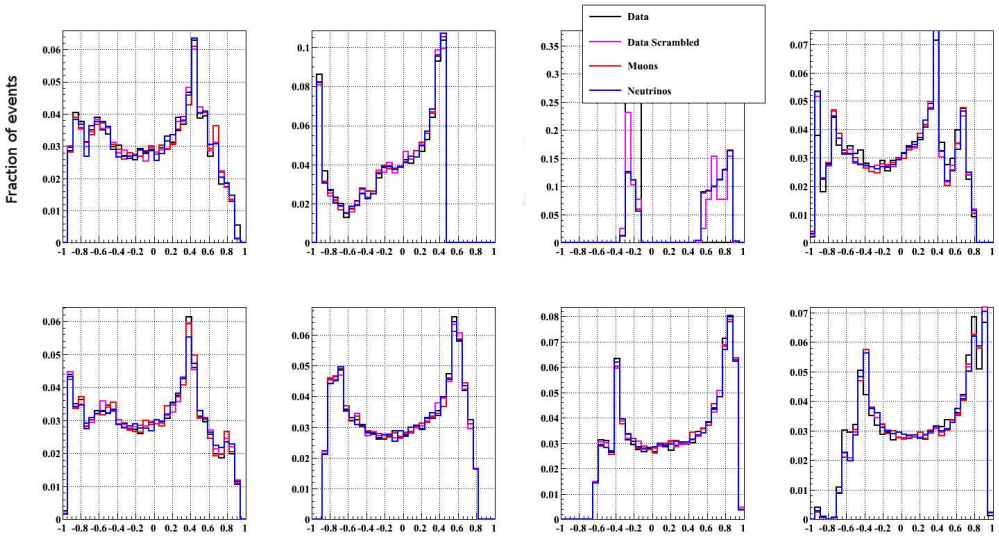

Figure 5.12: Comparison between the Sun's Cos[θ] extracted from data, Scrambled data, and Monte Carlo neutrino/muon. It shows the normalized distributions with respect to the lifetime without any quality cuts. The top distributions are for the 10pe periods, and the bottom are for the 3pe, and from left to right: 5, 9, 10, 12 Lines detector.

cone centered around the Sun as it follows it around the sky during our livetime. A good agreement can be found between the scrambled data and the Monte Carlo. With $\chi^2 < 2$ selection the event sample is largely dominated by atm_μ events, as can be seen in figure 5.9. In addition, for small $\Delta(\Psi)$ angle (which is the half-cone angle), the distribution in figure 5.15 is compatible with random distribution of events $\propto \theta^2$.

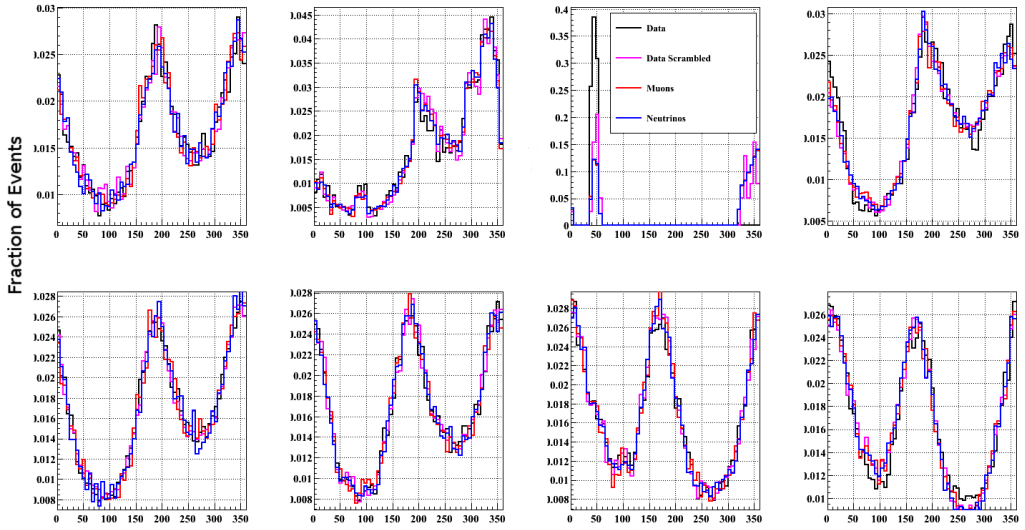

Figure 5.13: Comparison between the Sun's ϕ extracted from data, Scrambled data, and Monte Carlo neutrino/muon. It shows the normalized distributions with respect to the lifetime without any quality cuts. The top distributions are for the 10pe periods, and the bottom are for the 3pe, and from left to right: 5, 9, 10, 12 Lines detector.

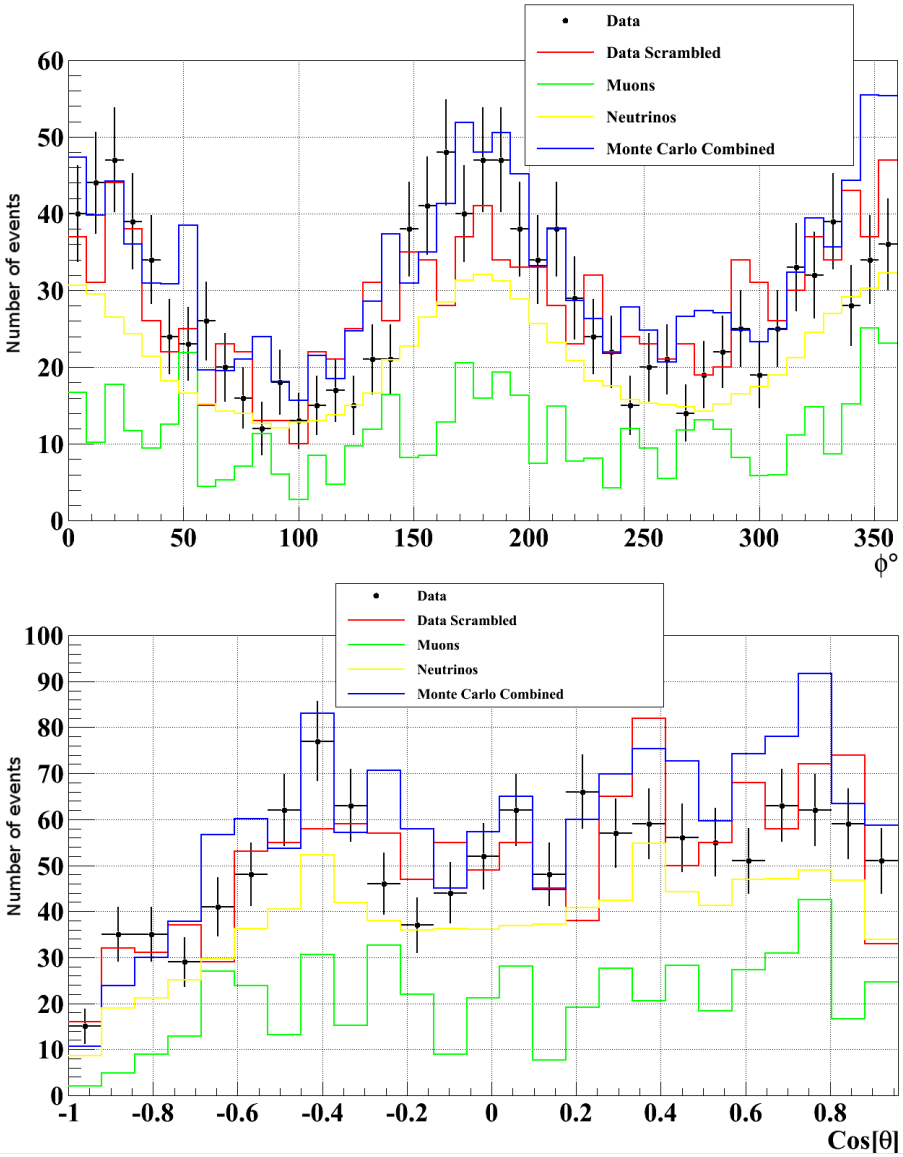

Figure 5.14: Comparison between the distributions of the Sun's ϕ and Cos[θ] from data, scrambled data, and background Monte Carlo. The muon and neutrino Monte Carlo are normalized to the lifetime of the data taking.

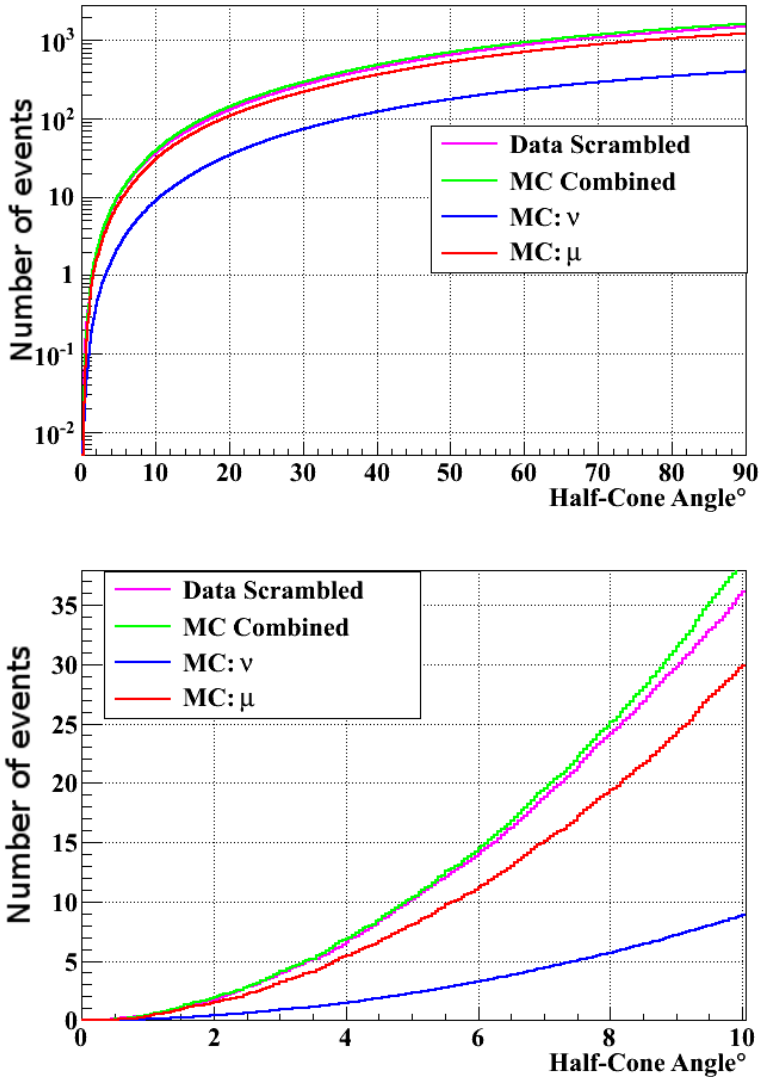

Figure 5.15: Estimation of the background distribution in the direction of the Sun, i.e the number of events inside a cone centered around the Sun as a function of the cone's half opening angle, with a quality cut of Tchi2 < 2.

5.7 Search strategy

If we look again at the angular resolution of ANTARES but this time using BB-Fit reconstruction strategy for energies below 1000 GeV as seen in figure 5.16 we can immediately see that the search for dark matter neutrinos is limited by ANTARES' angular resolution. If we look as well at figure 5.17, where $\Delta(\Psi)$ is the angle between the neutrino trajectory and reconstructed muon track (the neutrino trajectory points toward the Sun as consequence of section 5.4.1) for one dark matter spectrum, we can clearly see in that plot that for the neutrino signal: $\sim 60\%$ is concentrated is in the first 4 degrees and about $\sim 80\%$ in the first 8 degrees. The consequences is that the ratio of $\frac{n_{signal}}{n_{background}}$ is very sensitive to the value of the half-cone angle and this puts it as one of the main variables that will be used the search strategy. The effective livetime is around 140 days which is not competitive with existing limits for discovery, so in consequence the search strategy that we will employ is to extract an upper limit on the signal flux from the Sun using the Model Rejection Factor strategy which will be presented in the next section. Moreover, the expect dark matter signal is small and the scrambling method is going to dilute the signal, and as seen in the previous section in figure 5.15 the estimated background from scrambled data around the Sun is consistent with the background only estimation from the Monte Carlo, lending a Strong argument for the use of the scrambled data as a good estimator of the background.

5.7.1 Sensitivity

The sensitivity to a neutrino signal from dark matter annihilation in the Sun assuming a certain WIMP spectrum is defined in equation 5.1. Where $\bar{\mu}_{90\%}$ is the average sensitivity is calculated using the unified approach to the classical statistical analysis of small signals method or otherwise known as Feldman-Cousins method[103]. Since the detector in the 2007-2008 data set had 8 different configurations, the calculation of n_{signal} is actually a sum over the number of neutrinos and anti-neutrinos signal from each period as seen in equations 5.3 and 5.4 , the variable E_{min} which is used in these two equations is defined as the low energy threshold of ANTARES, while $A_{eff}^{\nu/\bar{\nu}}$ and $t_{livetime}$ are the respective $\nu/\bar{\nu}$ effective area and livetime of each period, and finally $\frac{dN_{\nu/\bar{\nu}}}{dE}$ is the $\nu/\bar{\nu}$ WIMP spectrum.

$$\bar{\Phi}_{90\%} = \frac{\bar{\mu}_{90\%}}{n_{signal}} \tag{5.1}$$

$$\bar{\mu}_{90\%}(n_{bgd}) = \sum_{j=0}^{\infty} \mu\left(j, n_{bgd}\right) \frac{n_{bgd}^{j}}{j!} e^{-n_{bgd}} \tag{5.2}$$

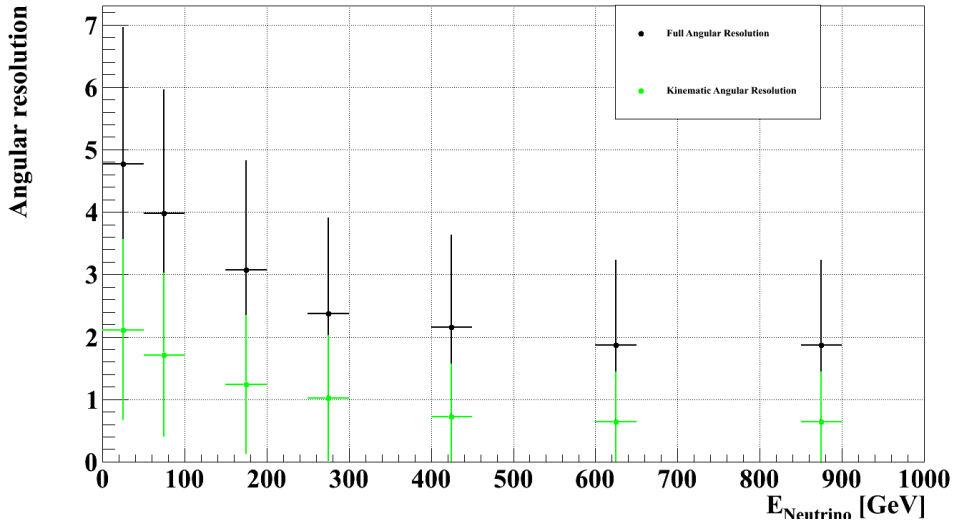

Figure 5.16: Mean angle between the neutrino direction and the reconstructed (BBFit) muons and the mean kinematic angle which is the angle between the neutrino direction and true muon direction, as a function of neutrino energy. A cut of $\chi^2 < 1.6$ was applied here.

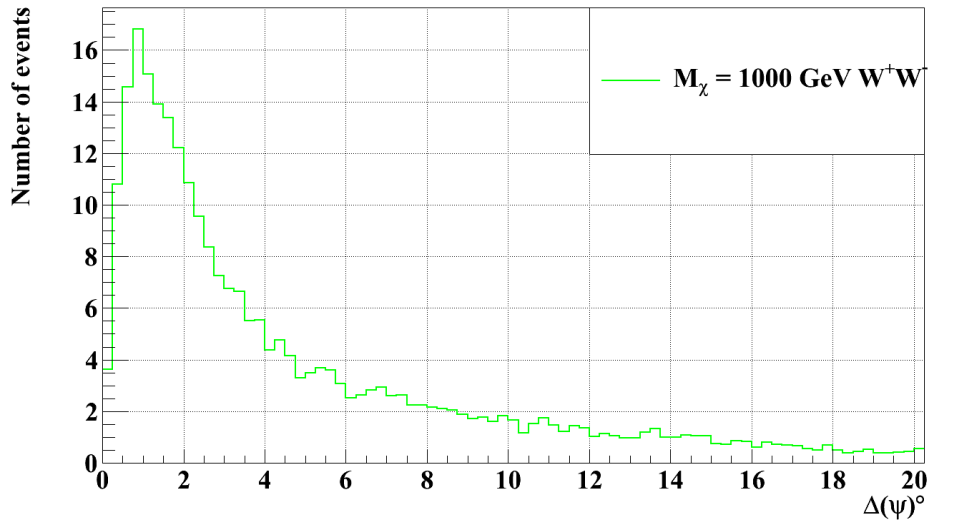

Figure 5.17: The differential distribution of number of events as a function of $\Delta(\Psi)$ which is the angle between the neutrino trajectory and reconstructed muon track for one dark matter spectrum. A cut of 1.6 on χ^2 was applied for this distribution.

$$n_{signal} = n_\nu + n_{\bar{\nu}}$$

$$n_\nu = \int_{E_{min}}^{E=M_\chi} \left[\frac{dN_\nu}{dE} . A^\nu_{eff} \cdot t_{livetime} . dE \right] \tag{5.3}$$

$$n_{\bar{\nu}} = \int_{E_{min}}^{E=M_\chi} \left[\frac{dN_{\bar{\nu}}}{dE} . A^{\bar{\nu}}_{eff} \cdot t_{livetime} . dE \right] \tag{5.4}$$

The average upper limit as it is defined in equation 5.2 stands for the upper limit $\mu\left(n_{detected}, n_{expected}\right)$ calculated with the Feldman-Cousins method and weighted by its Poisson probability, the n_{bgd} variable stands for the expected number of background, and j for the detected number of background.

5.7.2 Search variables and optimizations

As we previously saw, the half-cone angle between the direction of the Sun and the direction of the reconstructed muon is a good discriminator between a dark matter neutrino signal and the background, this can be seen again in figure 5.18. In addition if we look at figure 5.19 where we have the track χ^2 distribution of our background and our signal, we can see that for up-going events such as atmospheric neutrinos and the dark matter neutrino signal they have the same shape but the down-going muons that are reconstructed as up-going have a distinct shape. Thus the χ^2 variable will help us separate the badly reconstructed down-going muons (which dominates our data) and our up-going events which contains atmospheric neutrinos and a possible dark matter neutrino signal. The effect of other variables such as N_{hit}, or bchi2 are assumed to be minimal and will not be used in this optimization.

As consequence, these two variables (half-cone angle $\Delta(\Psi)$, χ^2) will be used to minimize the sensitivity to a dark matter signal. The search for the optimal point in ($\Delta(\Psi)$, χ^2) will be done by fixing the χ^2 at a certain value and search for the $\Delta(\Psi)$ cut that gives the lowest sensitivity, and then repeat the calculation for a different value of χ^2 . This iterative process is then done for all available WIMP spectra in order to find the best sensitivity for each dark matter model. The search region for the χ^2 variable would be between $\chi^2 = 1.2$ and $\chi^2 = 2$, and as for $\Delta(\Psi)$ it would be between $\Delta(\Psi) = 0^\circ$ and $\Delta(\Psi) = 10^\circ$.

Looking back at figure 5.19 we can expect to find the same χ^2 cut for all dark matter spectrum regardless of its mass or what annihilation channels, as they all share the same shape. This is indeed what is found as a result of the optimization as we can see in figure 5.21 where we can see the result of the difference of the optimized values for the sensitivity for two example spectrum . Now if we take

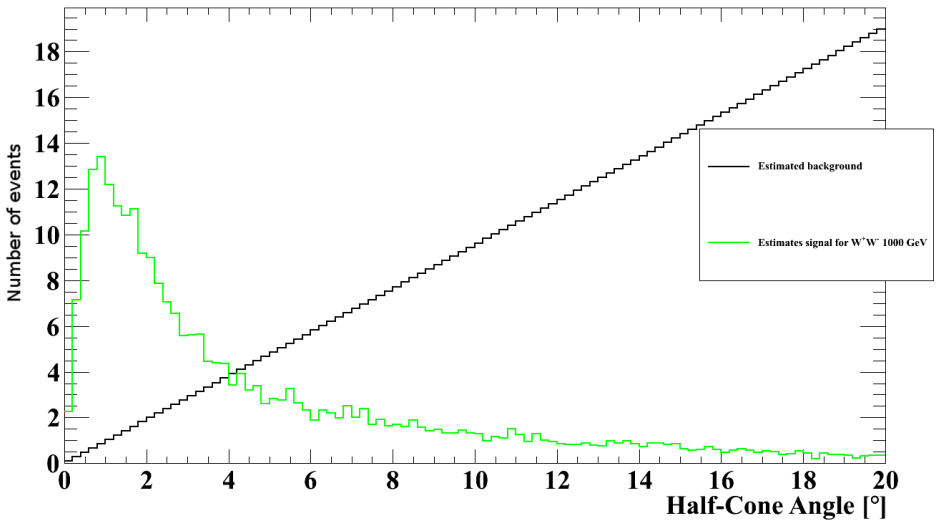

Figure 5.18: A comparison of the differential distribution of estimated dark matter signal and a fitted distribution of atmospheric background. A cut of $\chi^2 < 2$ was used here.

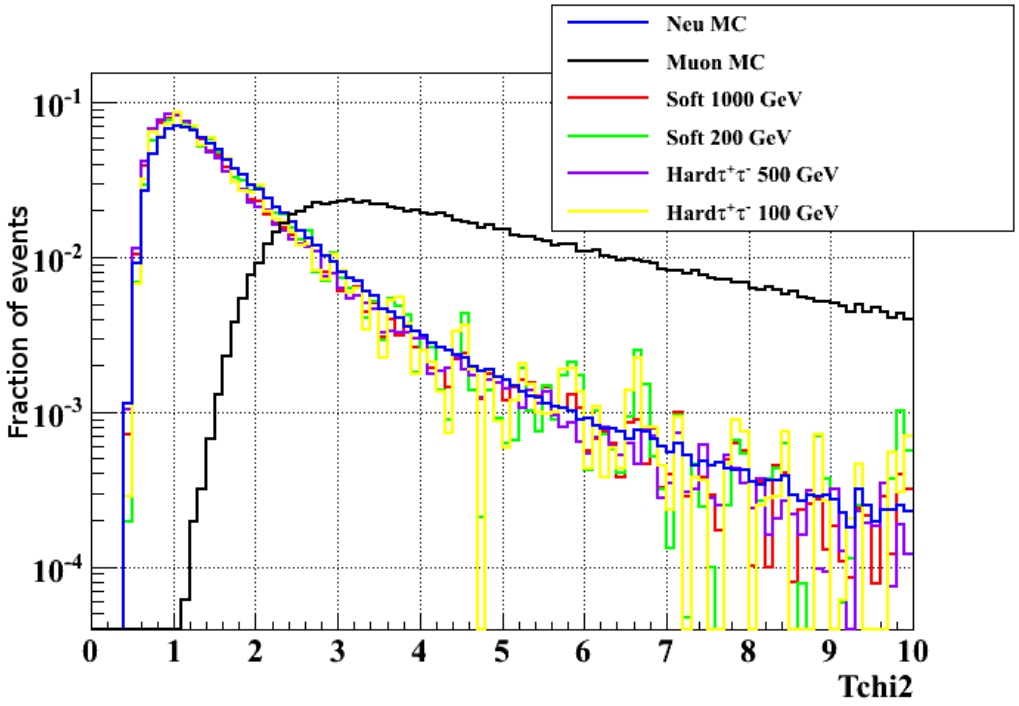

Figure 5.19: A comparison of the normalized to one χ^2distributions of the atmospheric muons, neutrinos and some dark matter spectrum.

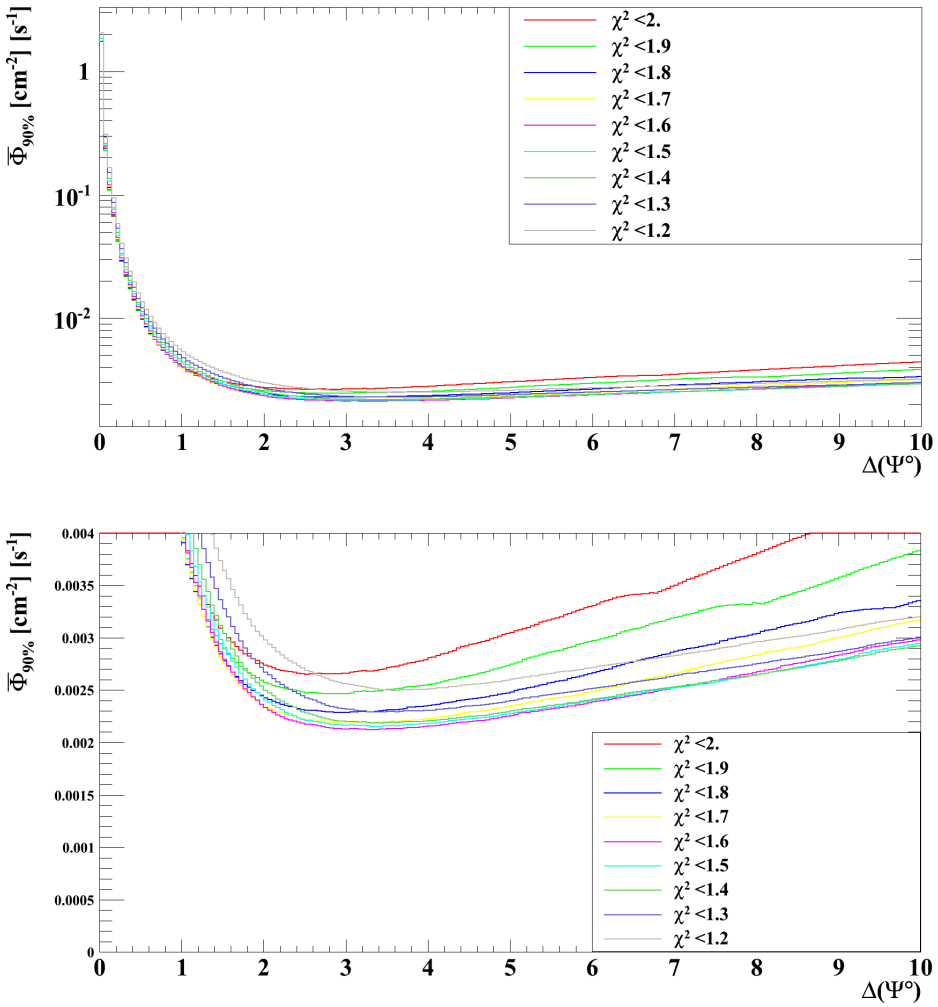

Figure 5.20: An example of minimization plot for a dark matter spectrum with $M_{WIMP} = 1000$ GeV via $\tau^+\tau^-$channel. The upper and lower plots are the full and zoomed versions of the same distribution.

a look at figure 5.22 we find a clear pattern where if the mass of the WIMP is heavier the higher fraction of the signal is concentrated at small $\Delta(\Psi)$ values. This is simply due to the fact that the heavier the WIMP is, more energetic the neutrinos can be and in consequence they have better angular resolution. The same effect can be noticed when looking at different annihilation channels as the b^+b^- channel is softer than W^+W^- or $\tau^+\tau^-$. Looking again in figure 5.22 we can see that the signal for 500 GeV $\tau^+\tau^-$ is concentrated at even lower $\Delta(\Psi)$ values than the signal for 1000 GeV b^+b^-, the simple reason is that the former simply annihilates on average into higher energetic neutrinos than the latter even though it is twice as heavy. This leads us to two predictions:

1. For the same annihilation channel we would expect to find a anti-correlation between optimized $\Delta(\Psi)$ cut and the WIMP mass, the heavier the WIMP the smaller the $\Delta(\Psi)$ cut should be.

2. For the same WIMP mass we would expect to see lower $\Delta(\Psi)$ cuts for $\tau^+\tau^-$ and W^+W^- (with almost no difference between them) when compared to the b^+b^- annihilation channel.

These two predictions are confirmed when looking at the final values of the optimized $\Delta(\Psi)$ cuts seen in figure 5.23.

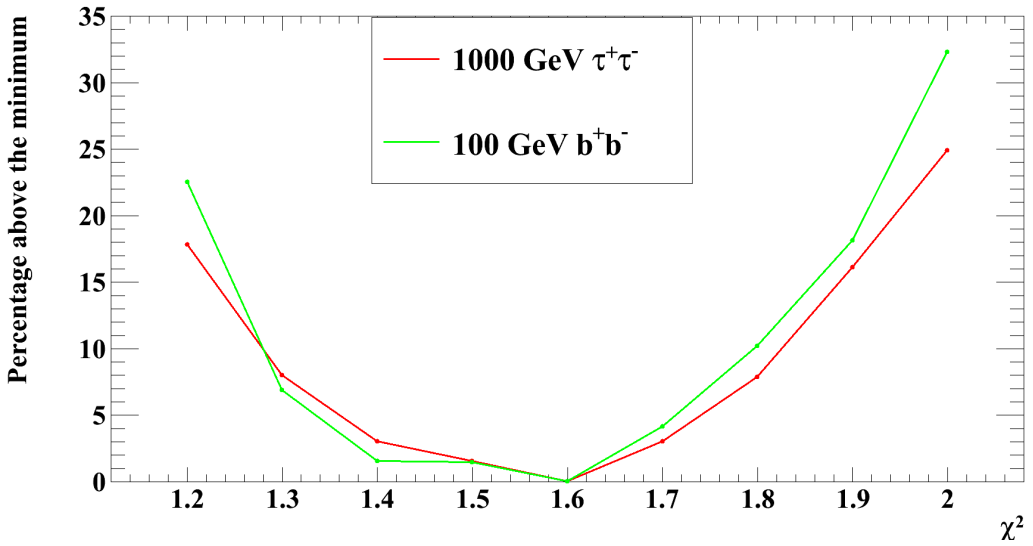

Figure 5.21: Percentage of difference among optimized sensitivity $\bar{\Phi}^{90\%}$ and the best value ($\chi^2 < 1.6$)with as a function of the χ^2 cut.

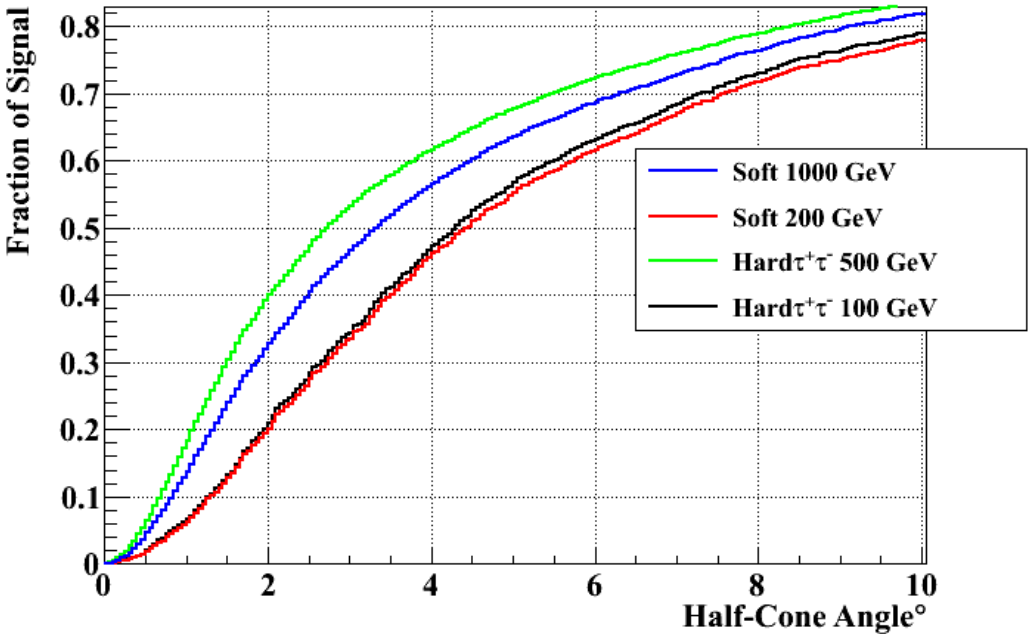

Figure 5.22: Normalized cumulative distributions of $\Delta(\Psi^\circ)$ for four dark matter spectrum with a cut of $\chi^2 < 2$.

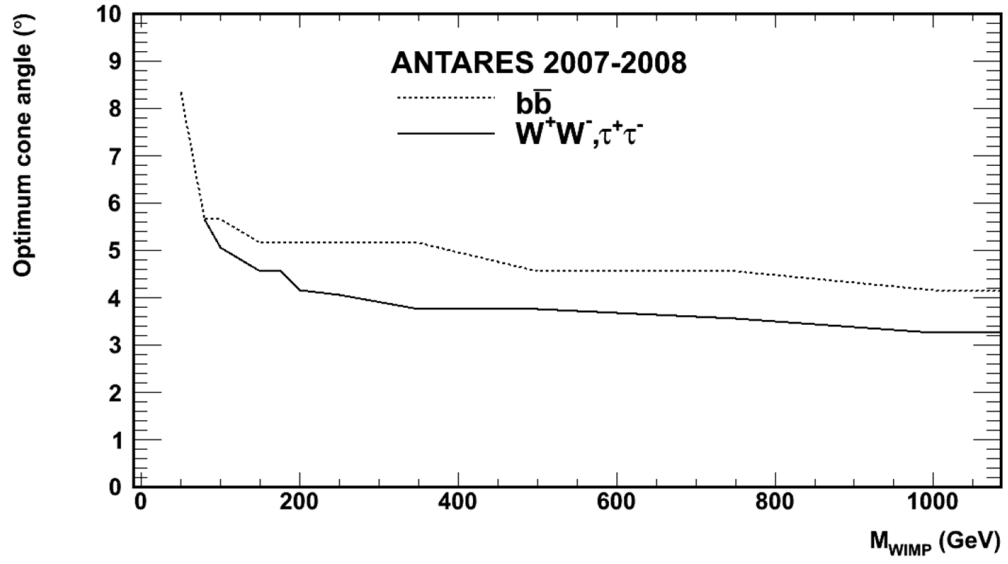

Figure 5.23: Optimal half-angle cut around the Sun as a function of the WIMP mass.

The resulting optimized sensitivities to different WIMP masses and spectra can be seen in figure 5.24, it is clear that we are much more sensitive to heavier WIMPs with harder spectra.

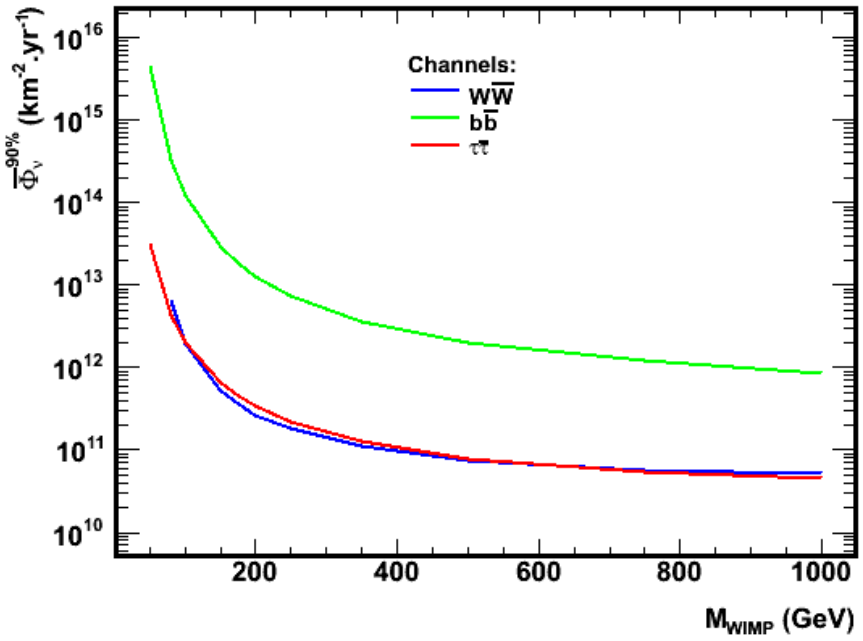

Figure 5.24: Sensitivity on the neutrino flux coming from dark matter annihilation inside the Sun as a function of WIMP mass and Spectra.

5.8 Unblinding results

5.8.1 Systematics Uncertainties

The systematics uncertainties for this analysis have been estimated[104]. There are several sources[105] for the uncertainty:

1. 15% in effective area due to OM efficiency uncertainty.
2. 15% in effective area due to OM time resolution uncertainty.
3. 15% uncertainty on angular resolution: .53$\pm$ .08 degrees.
4. Uncertainty on the absolute pointing of the detector[106]. The uncertainty is about 0.13° in azimuth and 0.06° in zenith angle.

It is important to note that there is no uncertainty on the expected background, as the estimation is done via scrambled data. The effect of (3) and (4) is to worsen the distribution of the signal in figure 5.18 and shift the peak to larger values of $\Delta(\Psi)$. As for (1) and (2) the effect is on the signal efficiency (effective area) and are assumed to be Gaussian. The effect of these uncertainties on the upper-limit were calculated using POLE++[107]. The resulting degradation on the the upper limit are found to be between 1.5% and 5.1%[104] depending on the WIMP mass and the spectrum (5.25).

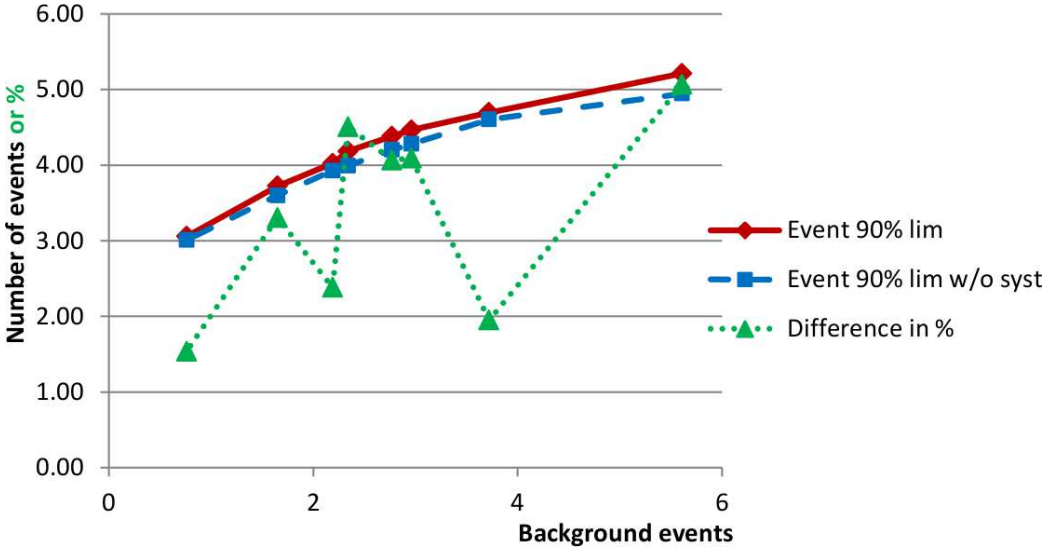

Figure 5.25: Comparison of the expect number of background with and without the expected uncertainties. The number of background is the expected number extracted from the optimization for the spectra, some of them have equal background expectation.

5.8.2 Upper limits

Figure 5.26 shows the differential distribution of the unblinded data towards the direction of the Sun, no excess events is found with respect to estimation done with scrambled data in the direction of the Sun. With this we can move from sensitivities to limits as it can be seen in figure 5.27 which is due to the fact that no excess events is found it is extremely similar to sensitivities previously extracted in figure 5.24 . In order to compare our results to different experiments such as ICECUBE, it is customary to display the results in muon flux. The relationship between the neutrino and muon flux is presented as following in equations 5.5 & 5.6 :

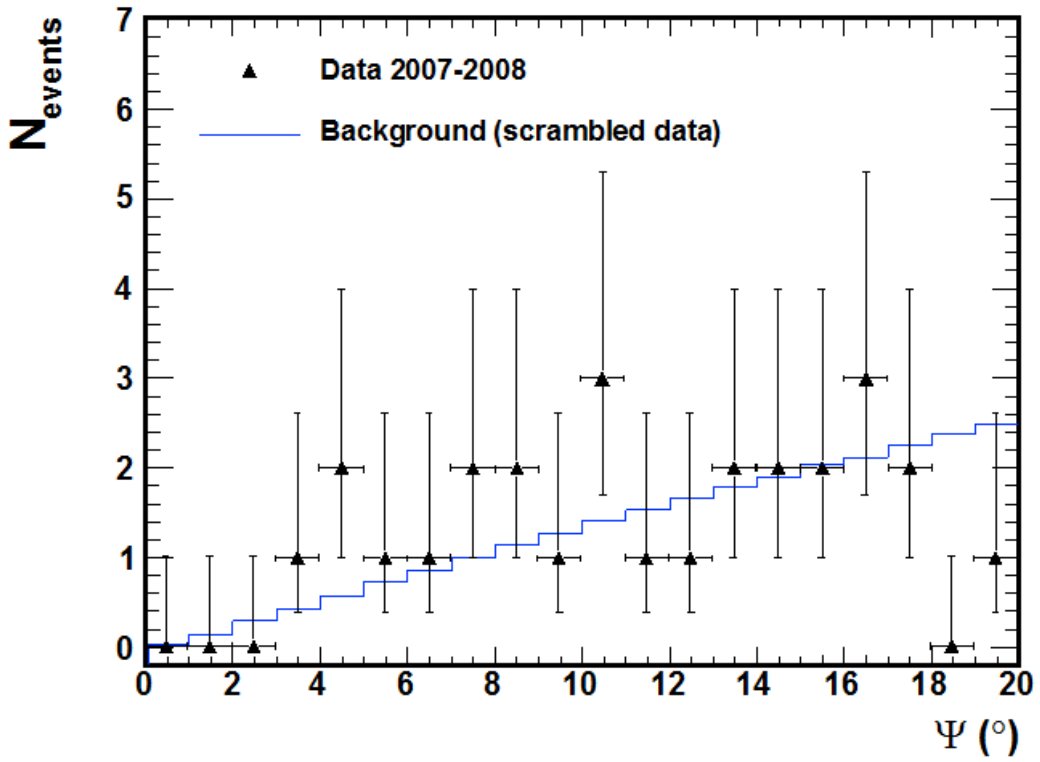

Figure 5.26: A comparison plot of the differential distribution of data and estimated background from scrambled data as a function of half-cone angle around the Sun. The χ^2 cut that was applied here is < 1.6

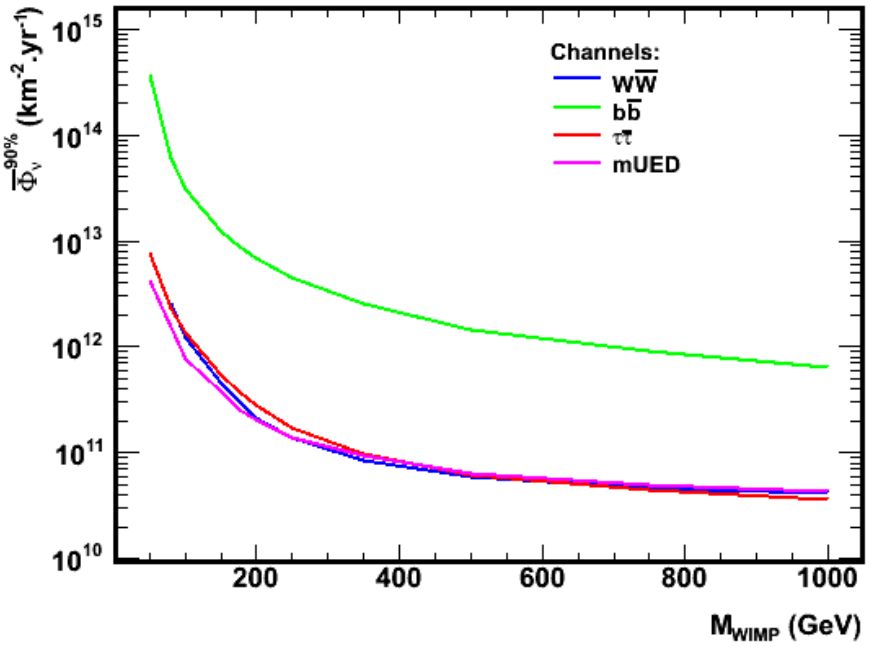

Figure 5.27: Limits on neutrino flux coming from dark matter annihilation inside the Sun as a function of WIMP mass and Spectra.

$$\frac{d\Phi_\mu}{dE_\nu} = \frac{d\Phi_\nu}{dE_\nu} P_{earth} \rho N_A \sigma_{CC}(E_\nu) R_{eff}(E_\nu) \tag{5.5}$$

$$\frac{d\Phi_\mu}{dE_\nu} . A_\mu^{Eff} = \frac{d\Phi_\nu}{dE_\nu} . A_\nu^{Eff} \tag{5.6}$$

where, P_{Earth}: Probability of a neutrino not interacting in Earth (Figure 5.28). ρ: Density of matter. σ_{CC}: Charged Current cross-section (Figure 5.29). R_{eff}: Effective muon range (Figure 5.30).

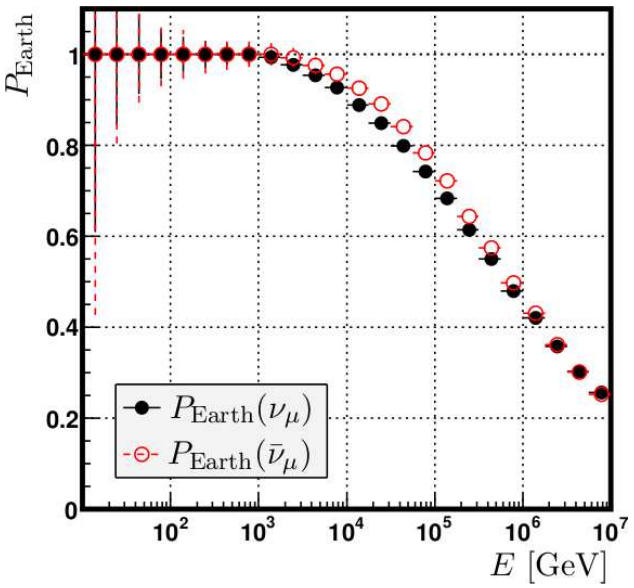

Figure 5.28: Probability of a $\bar{\nu}/\nu$ not interacting in Earth as a function of its energy [108] .

From eq 5.5 we can use P_{Earth}, σ_{CC} and R_{eff} as a conversion factor between neutrino flux and muon flux and we can transform our neutrino limits into muon limits as we can see in figure 5.31.

As we have seen in chapter 2, we can go from the μ or ν flux to the annihilation rate Γ inside the sun, and if we further assume there is an equilibrium between Γ and the capture rate C of WIMPs we can put limits on the σ_{SD} and on σ_{SI} as seen figure 5.32 & 5.33. It is obvious from the last three figures that while we are able probe some of the CMSSM parameter space in Spin-dependent cross-section (Figure 5.32) and just starting to close in on the spin-independent region (Figure 5.33), but the limits imposed by ANTARES when compared to other experiments are not exactly competitive (Figure 5.31). The limits presented by the SuperK experiment[109] dominate at WIMP masses below 180 GeV, while

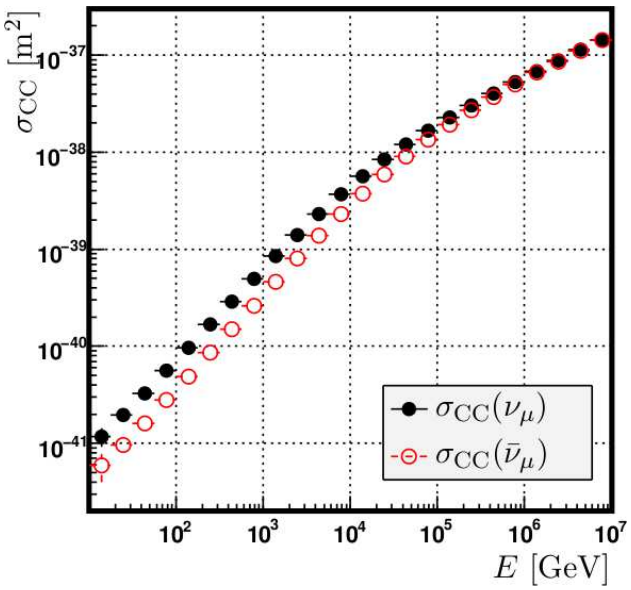

Figure 5.29: Charged Current cross-section of $\bar{\nu}/\nu$ with matter as a function of its energy [108] .

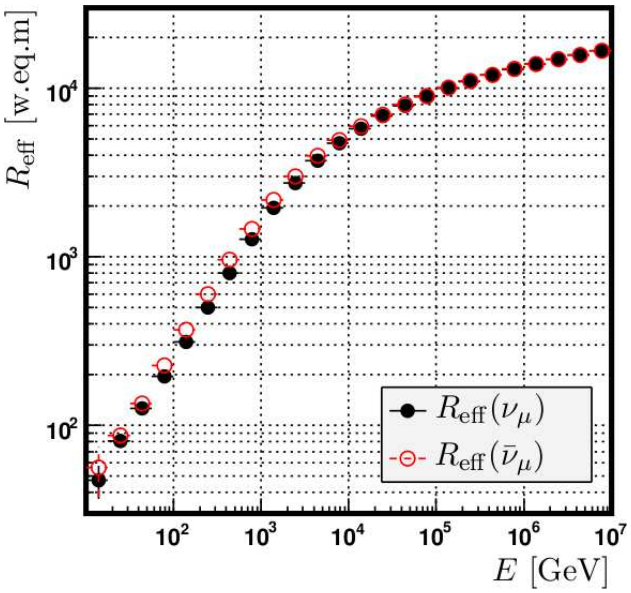

Figure 5.30: Effective range of $\bar{\mu}/\mu$ as a function of its neutrino energy [108] .

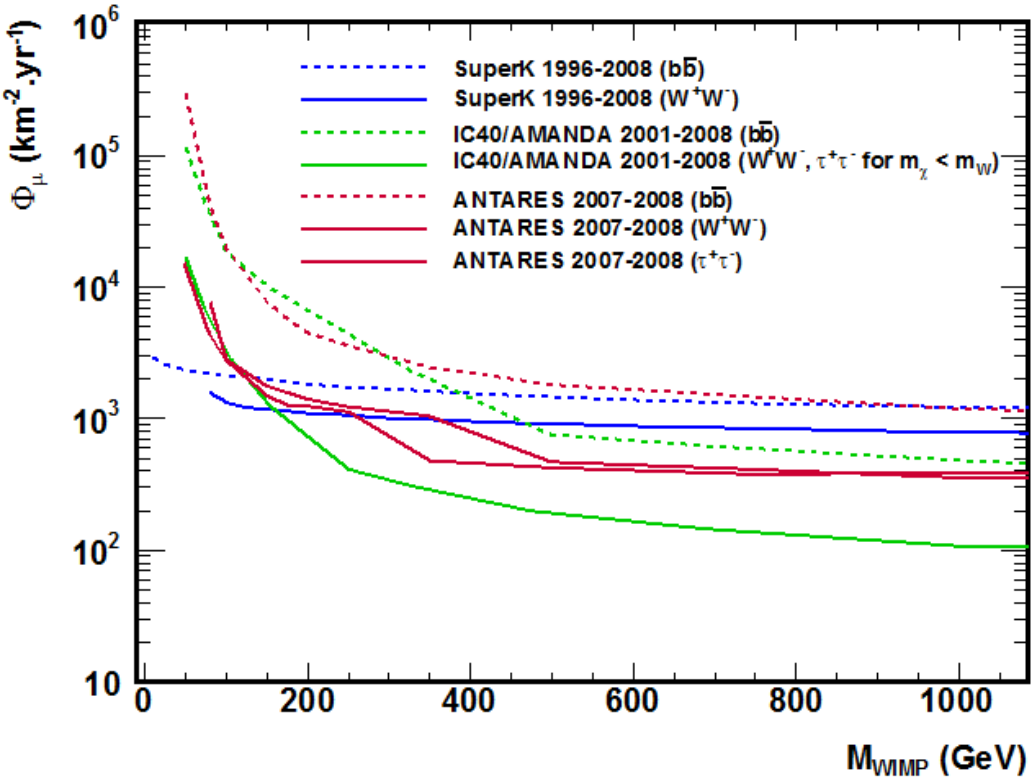

Figure 5.31: Limits on the muon flux as a function of WIMP mass and spectrum.

those by ICECUBE[69] dominate at masses higher then that. However, we would expect with the 2007-2010 data analysis (next chapter) to improve the limits in a way to allow us to be competitive with those of SuperK and ICECUBE.

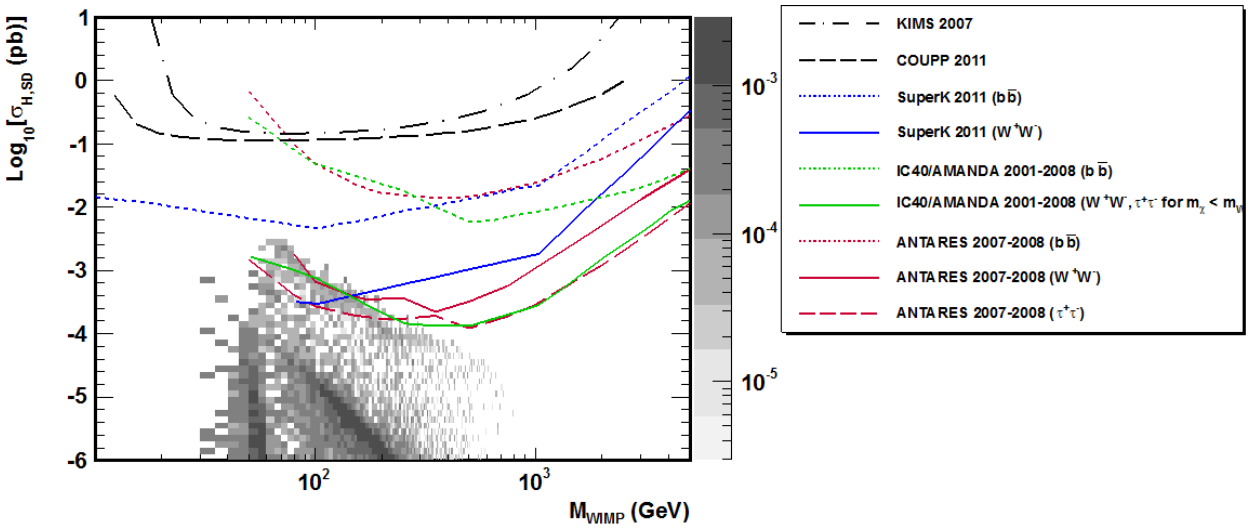

Figure 5.32: Limits to spin dependent cross-section of WIMPs inside the Sun.

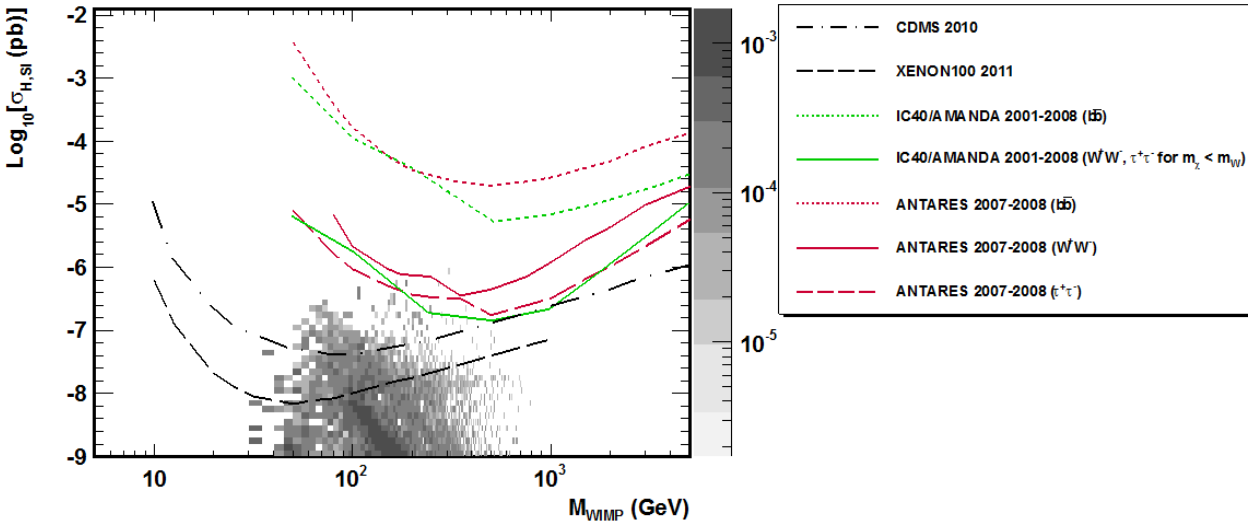

Figure 5.33: Limits on spin independent cross-section of WIMPs inside the Sun.

Chapter 6

Dark Matter search in the direction of the SUN with 2007-2010 data

In this chapter we will present the analysis with the 2007-2010 data.

6.1 Data selection and new background Monte Carlo

A recent development in the generation of the MC allows us to use more data. Instead of having one MC file for each period (ex: 9 Lines 3 pe) now each run has its own MC[110] that is generated according to the detector efficiency (working OMs) and averaged optical background of that run. The benefit of this method is the opportunity to include previously excluded data runs with lower quality in the analysis. Each run now has 5 main MC files (plus an additional 12 for the ν_e neutrino and for NC interaction events), 1 for atmospheric muons and 4 for atmospheric (anti-)neutrinos (2 low energy simulation and 2 with normal energy ranges). Data selection is now done for runs with $QB \geq 1$ (section 4.1.3). In addition between 2007 and 2010 we have over 8000 runs. However, we exclude from the data sample runs where the Sun is above the horizon. With this criteria we find 2882 runs (314.6 days livetime) where the Sun is below the horizon for the entire run-time, and an additional 1756 runs (226.3 days of livetime) where the Sun changes between below and above the horizon during run-time. We end up with 4638 runs with a total livetime of 541 days and 427.7 days of effective livetime with the Sun below the horizon. The simulation parameters of the MC is essentially the same as in the 2007-2008 analysis with small differences, we include some of them:

- Atmospheric muons were generated with 1/3 of the livetime of the run.
- Low energy atmospheric neutrinos are generated between 5 GeV and 3 TeV

with 2.10^8 neutrinos per run.

- Standard atmospheric neutrinos are generated between 100 GeV and 10^8 GeV with 10^9 neutrinos per run.

6.1.1 Dark Matter Monte Carlo

In the section 5.4.1 we presented a way to simulate the dark matter neutrino signal. However, this method will not be used for this analysis because of the short livetime for each MC which is few hours, while it was few months in the previous chapter. So in this section we will present the new method that is based as well on each run having its own dark matter neutrino MC.
The Sun does indeed have a variable declination $[-23°26^{'}, 23°26^{'}]$ with a period of 6 month ($46°52^{'}$), but during one run (typically 2 hours) the declination varies on average by $0.021°$, so for all that matters during one run the Sun can be considered stationary in equatorial (declination [δ] , right-ascension [RA]) coordinates. So it might be possible to use the neutrino MC generator in its point source mode to simulate a neutrinos coming from the Sun. However, we must first verify that it works.
In GENHEN, the point source mode is a mode where the source is fixed in δ but during simulation RA is randomly generated in [0 ,2π] interval, so it is important to verify that this will not affect the calculation of the position of the Sun with a fixed δ. For this we pick a random run and calculate the position of the Sun in local coordinates [Elevation, Azimuth] via three different methods:

1. True position of the Sun.

2. Position of the Sun with both δ and RA fixed. Both values are calculated at mid-run time.

3. Position of the Sun with δ fixed and RA randomized as in GENHEN. The used δ is calculated at mid-run time.

Figure 6.1 shows the true position of the Sun taken from the previously selected run. It is obvious that the position taken in the sky by the Sun is quite limited in the coordinates space. Now if we take a look at figure 6.2, we can clearly see that using methods (2) and (3) produce exactly the same Sun position in the local coordinates but nevertheless they don't look exactly like in 6.1. However, if we look at the distributions only in the region where the Sun should only be during the time of the run(taken from figure 6.1) we can see that the agreement is perfect (Figure 6.3).

So the method for creating our signal MC is the following:

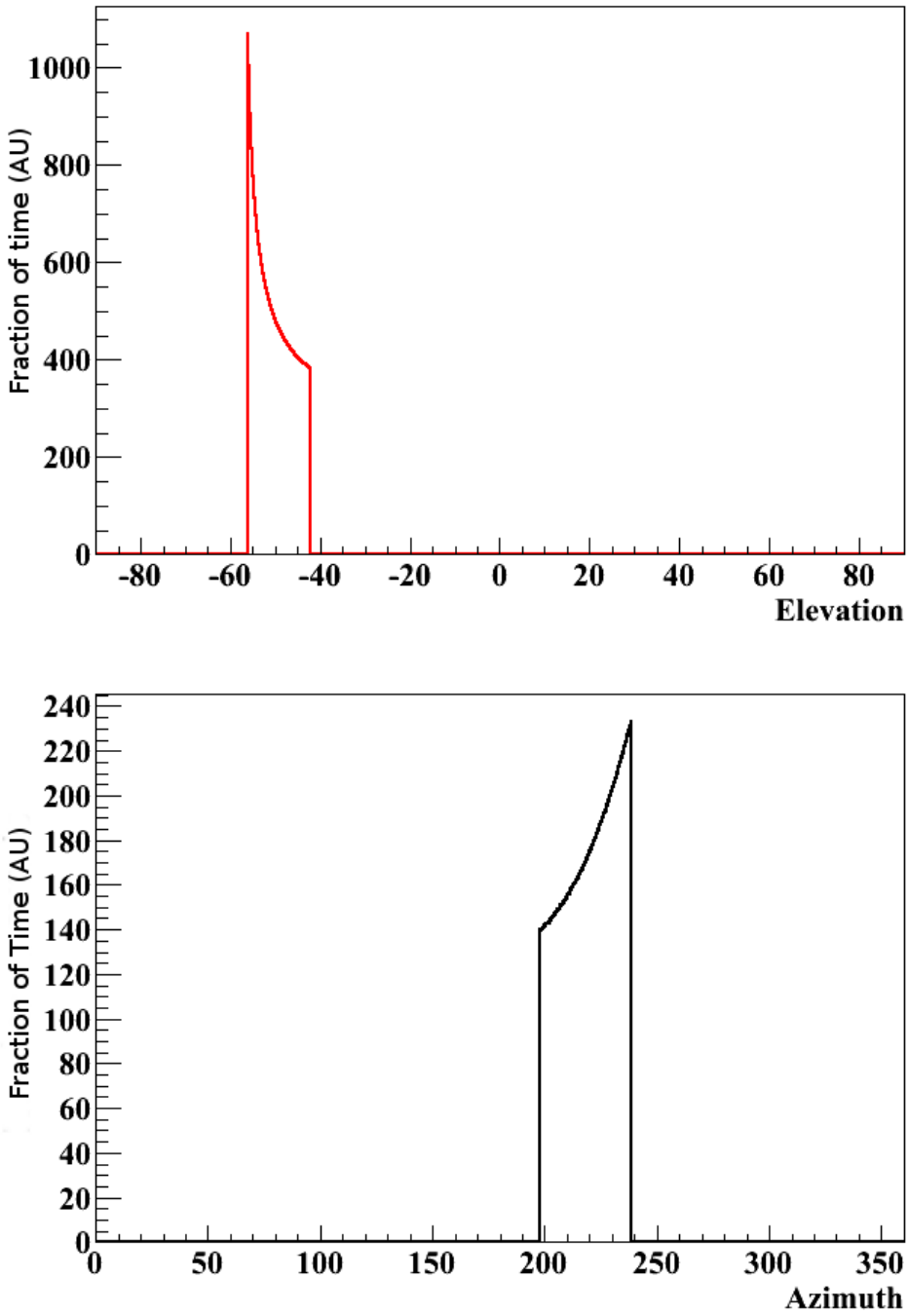

Figure 6.1: . True Position of the Sun during one run.

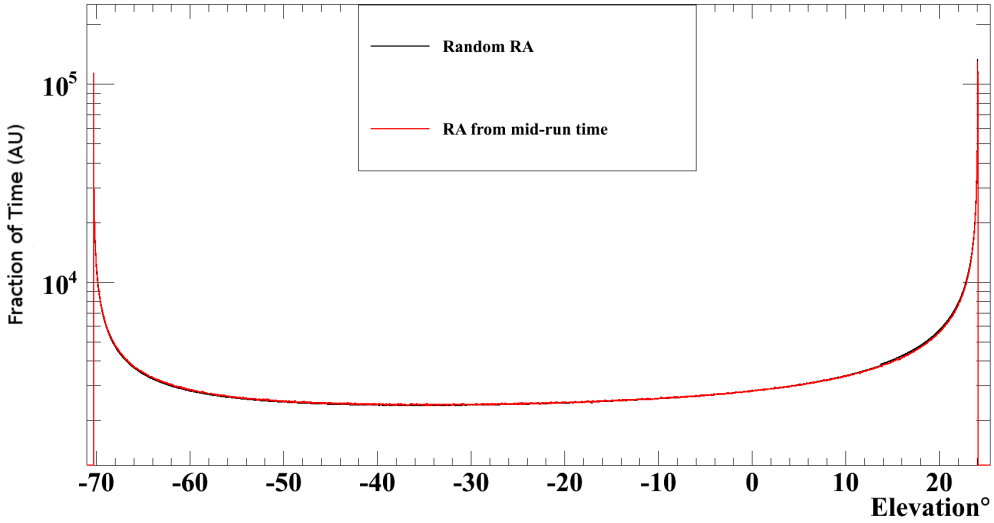

Figure 6.2: . Comparison of two different methods to calculate the position of the Sun in local coordinates (Elevation). First method is with both δ and RA fixed (red curve) while the other is with δ fixed and RA randomized (black curve).

1. For each run calculate the value of δ of the Sun at mid-run time, and use it with GENHEN point source mode to create the $\nu/\bar{\nu}$ MC.
2. Calculate the region where the Sun occupies in local coordinates (Zenith , Azimuth) during the run and remove events from the MC that are outside this region.
3. For different M_χ we remove events that have $E_\nu > M_\chi$.
4. We apply for each dark matter model the corresponding $\frac{dN}{dE}$ to the remaining events by re-weighting the MC event spectrum via a convolution with the effective area of the detector.

After applying this method we get the following distribution of our MC signal in figures 6.4 & 6.5 .

6.2 Reconstruction Strategy

For this analysis both AAFit and BBFit reconstruction strategies will be used. And later in section 6.6 we will present a comparison of the two strategies and the implications on presented sensitivities and limits.

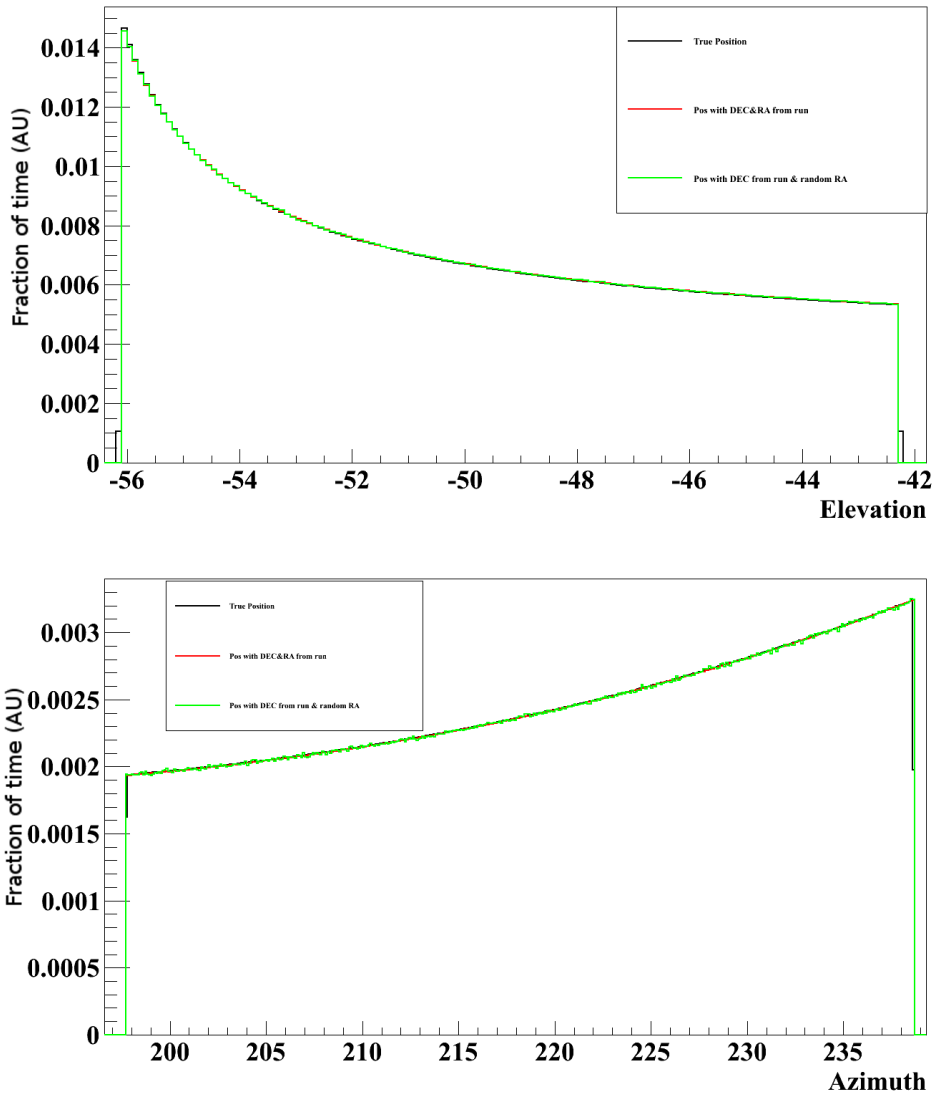

Figure 6.3: Comparison of the three different methods of generating the Sun position in local coordinates. Upper plot is for Elevation and the lower is for Azimuth.

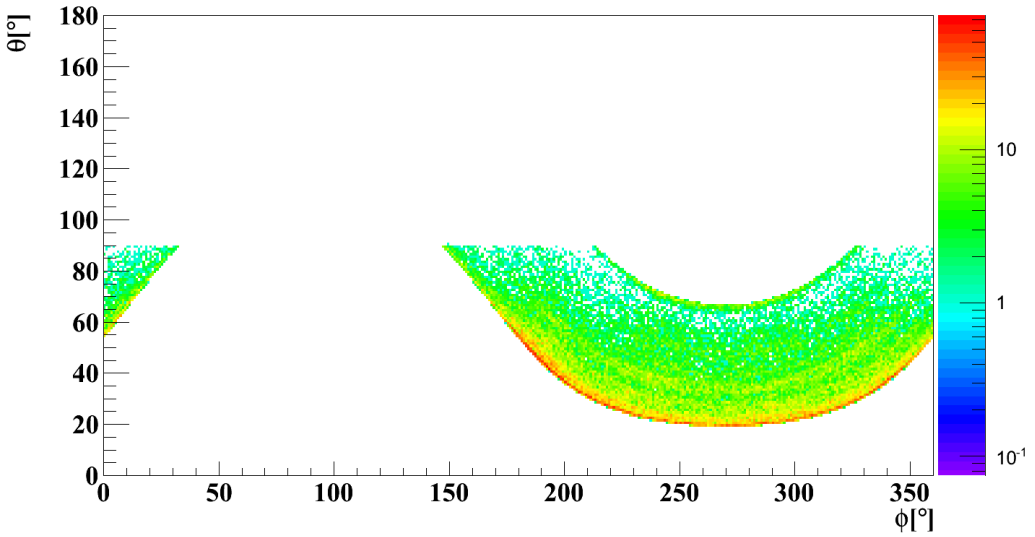

Figure 6.4: The true distribution of θ° and ϕ° of our dark matter neutrino signal for the 2007-2010 period.

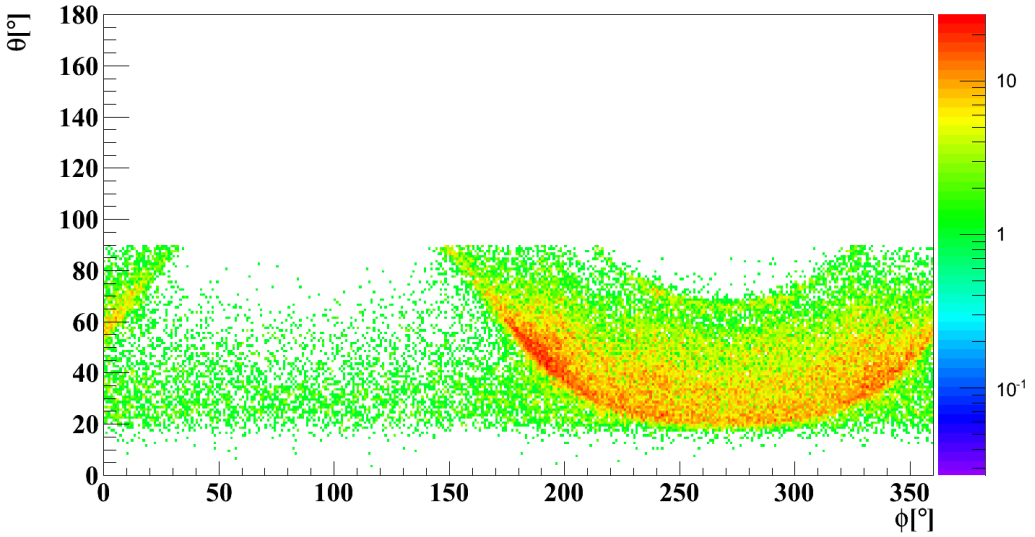

Figure 6.5: The distribution of reconstructed θ° and ϕ° using AAFit reconstruction strategy of our simulated dark matter neutrino signal for the 2007-2010 period. No cuts were applied here.

For BBFit all variables mentioned in section 5.3 will be used again for this analysis.
For AAFit we will use the following variables:

- Λ: Value of the maximum likelihood of the fit.
- β: Estimation on the angular uncertainty of the direction of the fitted muon track.
- Nhit: Number of hits used in the fit.
- tcosth: Cos[zenith] of the fitted track.
- tphi: ϕ (azimuth) of the fitted track.

6.3 Search strategy

The search strategy that is going to be employed in this chapter is going to be in essence exactly as in chapter 5. The extracted sensitivities and eventual limits will again be based on the unified approach to the classical statistical analysis of small signals or Feldman-Cousins [103]. The difference now in equations 6.1, 6.2, & 6.4 is that $t_{livetime}$ and A^{ν}_{eff} are now calculated for each run, this changes the equation 6.3 to become $n_{signal} = \sum_{run} n^{run}_{\nu} + n^{run}_{\bar{\nu}}$.

$$\bar{\Phi}_{90\%} = \frac{\bar{\mu}_{90\%}}{n_{signal}} \tag{6.1}$$

$$\bar{\mu}_{90\%}(n_{bgd}) = \sum_{j=0}^{\infty} \mu\left(j, n_{bgd}\right) \frac{n^{j}_{bgd}}{j!} e^{-n_{bgd}} \tag{6.2}$$

$$n_{signal} = n_{\nu} + n_{\bar{\nu}} \tag{6.3}$$

$$n_{\nu} = \int_{E_{min}}^{E=M_{\chi}} \left[\frac{dN_{\nu}}{dE} . A^{\nu}_{eff} \cdot t_{livetime} . dE \right] \tag{6.4}$$

6.4 Dark Matter with BBFit

In this section we will represent the sensitivities produced with BBFit.

6.4.1 BBFit Multi-line analysis

As in chapter 5 this analysis will follow the same route with the addition of one enhancement to the analysis.

6.4.1.1 Data Monte Carlo comparison

Just as in the 2007-2008 data analysis we need to test the agreement between our data set and our Monte Carlo, and for that we use a set preliminary cuts (basic quality cuts), we list them here[1]:

- Nhit ≥ 5. BBFit χ^2 Cherenkov fit requires exactly 5 hits to fit the track.
- nlines > 1. A cut on the number of lines used in the fit. These events are called Multi-line events, where the BBFit algorithm converge into a solution on ϕ.
- tchi2 < bchi2. A cut that selects events that are better reconstructed as a muon generating a Cherenkov light cone than a shower bright point.
- tcosth > 0. A cut that selects up-going events.

In figure 6.6 we can see the comparison of the χ^2 distribution of data, background MC for atm_μ and atm_ν , and two dark matter spectra (1000 GeV $\tau^+\tau^-$ and 50 GeV b^+b^-). We can notice immediately that the data-MC agreement at large values of χ^2 is bad, background estimation coming from atmospheric muons is twice as much data. However this will not be an issue as we are more interested in the low χ^2 region where we have good data-MC (where atm_ν dominates), also scrambled data is going to be used again to estimate the background in the direction of the Sun. In addition we can conclude as we did earlier in section 5.5 that the dark matter spectra (from the two extremes, low mass soft channel to high mass hard channel) behaves similarly in χ^2 as to atm_ν . Figure 6.7 presents another comparison between data and MC as a function of $\text{Cos}[\theta]$ with a tight cut of $\chi^2 < 1.6$. With such cut on the χ^2, the agreement between data and MC is much better.

[1] They are basically the same as the previous analysis

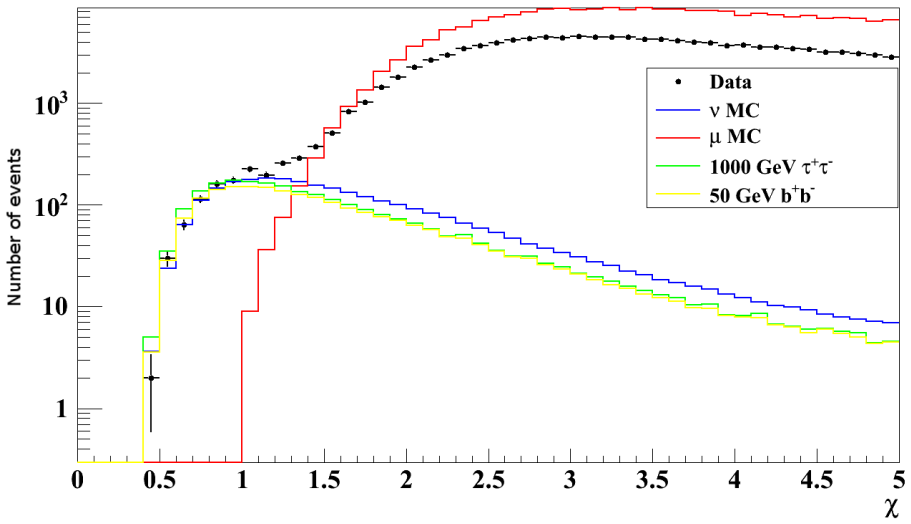

Figure 6.6: The distribution of χ^2 for data and atmospheric neutrinos/muons and two dark matter spectrum. The muon and neutrino Monte Carlo are normalized to the lifetime of the data taking.

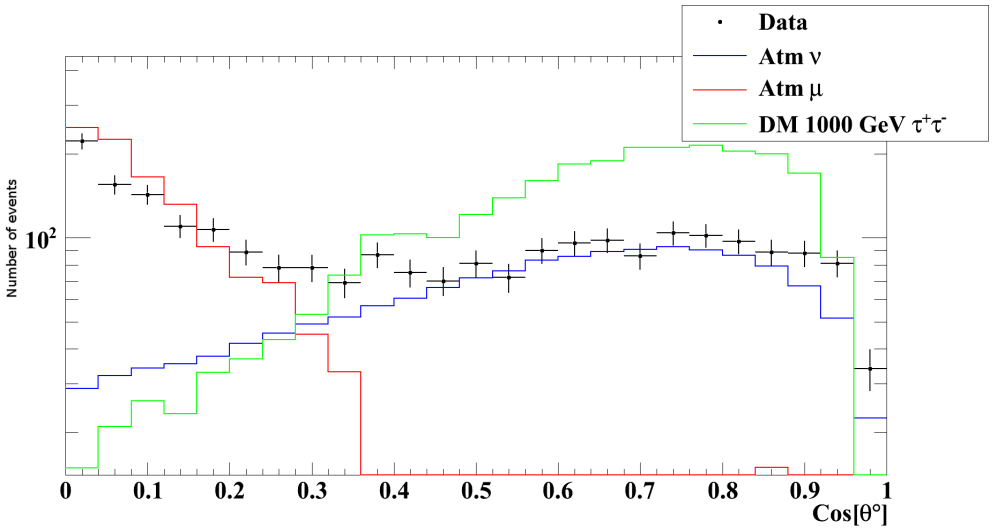

Figure 6.7: Cos[θ] distribution for data and atmospheric neutrinos/muons and one dark matter spectrum. A cut of $\chi^2 < 1.6$ was applied here. The muon and neutrino Monte Carlo are normalized to the lifetime of the data taking.

6.4.1.2 Background estimation

The background estimation in the direction of the Sun is done similarly as shown in section 5.6. However, since now we have a different MC for each run, the scrambling of the Sun is done within the time-frame of the run to which the event belong to. In figure 6.8 we can see a comparison of the estimation of the background in the direction of the Sun as a function of the half-cone with scrambled data and the MC. While the agreement is not perfect, this should not be a problem as again we will be using the scrambled data as our estimator of the background. Again we find that for low $\Delta(\Psi)$ the background is compatible with a random distribution of events $N_{events} \propto \Delta(\Psi)^2$

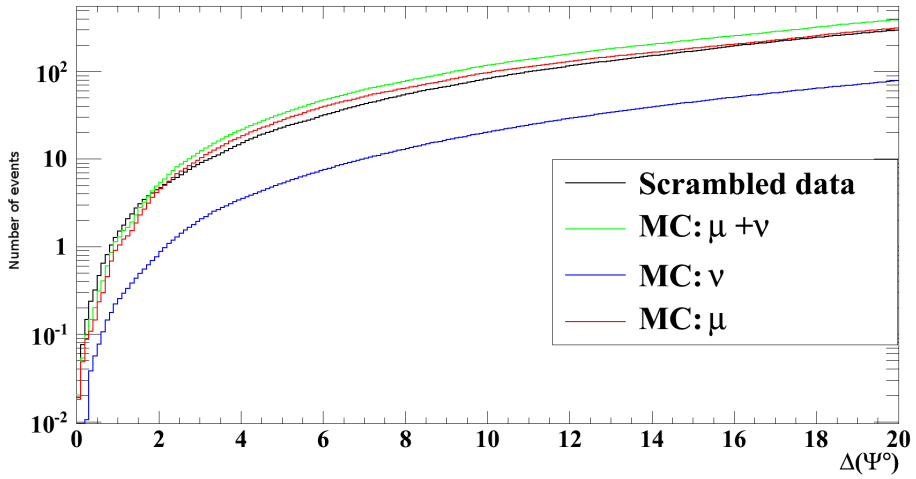

Figure 6.8: The estimation of the background in the direction of the Sun as a function of the half-cone centered around it. The scrambled data in addition to the MC are presented here. A cut of $\chi^2 < 2$ was applied here.

6.4.1.3 Search variables and optimization

The search variables for this part of the analysis are going to be again χ^2 and $\Delta(\Psi^\circ)$. And again the search region for the χ^2 variable would be between $\chi^2 = 1.2$ and $\chi^2 = 2$, and as for $\Delta(\Psi)$ it would be between $\Delta(\Psi) = 0^\circ$ and $\Delta(\Psi) = 10^\circ$. Similarly to chapter 5, we find one χ^2 cut for all of our dark matter models, this value is again 1.6 . Figure 6.9 shows a comparison of the estimated background in the direction of the Sun from scrambled data and one dark matter model for the optimized χ^2 cut. Figure 6.10 shows the value of the optimized $\Delta(\Psi^\circ)$ cut as a function of the WIMP mass, we can notice that for $M_{WIMP} = 150$ GeV the

annihilation channel W^+W^- the optimized cut is slightly better than 176 or 200 GeV, this behavior is purely a random behavior, and if we change the χ^2 cut, we find a cut that is larger than 176 GeV and smaller than 100 GeV WIMP mass. These values when compared to those obtained in the 2007-2008 analysis (figure 5.23) we see a slight tightening of the cuts. This is due for two reasons, one is the more specialized run-by-run MC. The second reason is because the 12-lines detector has better angular resolution than the 5-lines detector, the 2007-2008 analysis had larger contribution of the 5-lines detector compared 2007-2010 analysis.

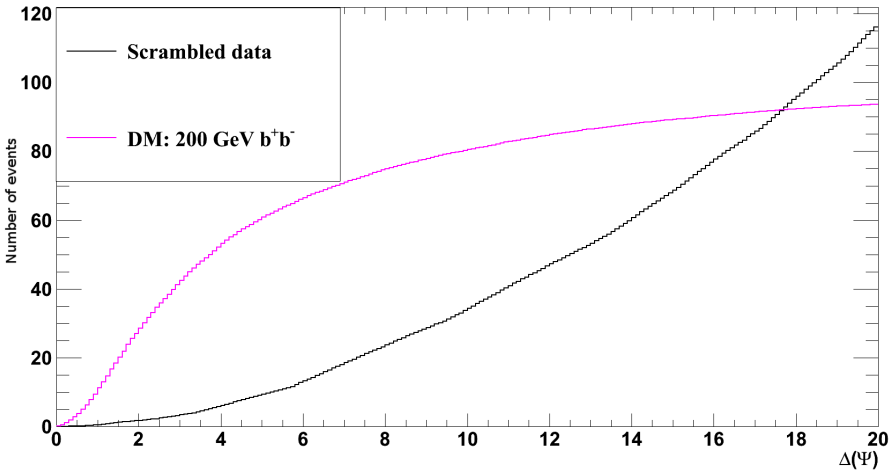

Figure 6.9: Comparison of the estimated background in the direction of the Sun from scrambled data and one dark matter model (200 GeV b^+b^-).A cut of $\chi^2 <$ 1.6 was applied here.

Finally in figure 6.11 we can see the resulting sensitivities. As expected annihilation channels W^+W^- & $\tau^+\tau^-$ provide us with better sensitivities than b^+b^-, while higher WIMP masses are better than low WIMP masses.

6.4.1.4 Comparison with 2007-2008 analysis

The analysis in the previous chapter with the 2007-2008 is a BBFit multi-line analysis. With 2007-2010 we have 427.7 days of effective livetime while the 2007-2008 we had 146.7 days of effective livetime (when the Sun is below the horizon). Additionally the contribution of the 5-lines detector to the livetime drops from 50% during 2007-2008 to less than 15% in 2007-2010, the 5-lines detector is a much smaller in comparison to the 12-lines detector and has a smaller effective area, so while we gain an improvement factor from the livetime, we gain as well by

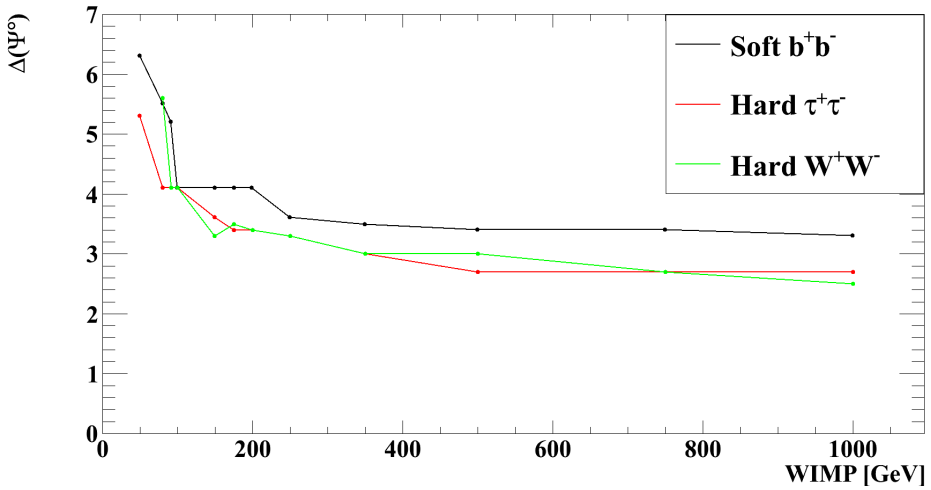

Figure 6.10: Comparison of the optimized $\Delta(\Psi^{\circ})$ cut as a function of the WIMP mass and the annihilation channel .

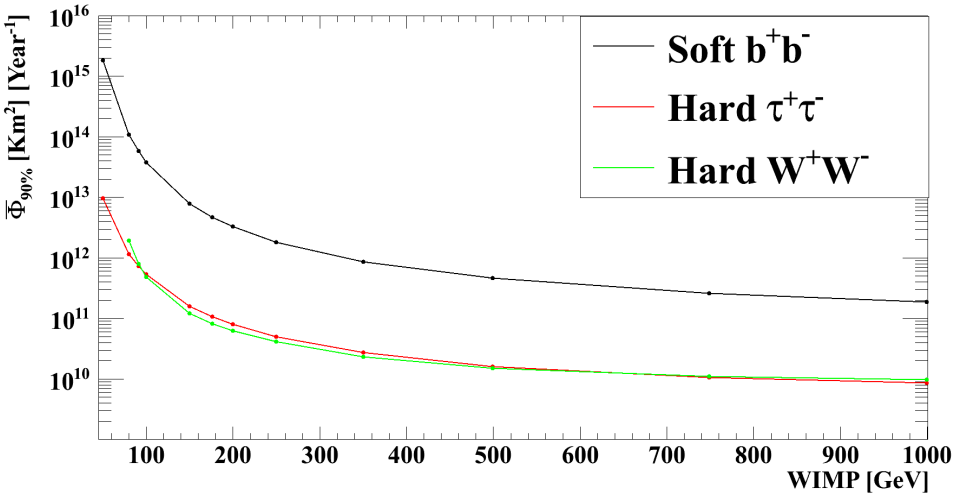

Figure 6.11: Sensitivity to neutrino flux coming from dark matter annihilation inside the Sun as a function of WIMP mass and the annihilation channel.

lowering the total contribution of the 5-lines detector. Finally, figure 6.12 shows the improvement we get over the 2007-2008 analysis, we gain a factor $3 \sim 5$.

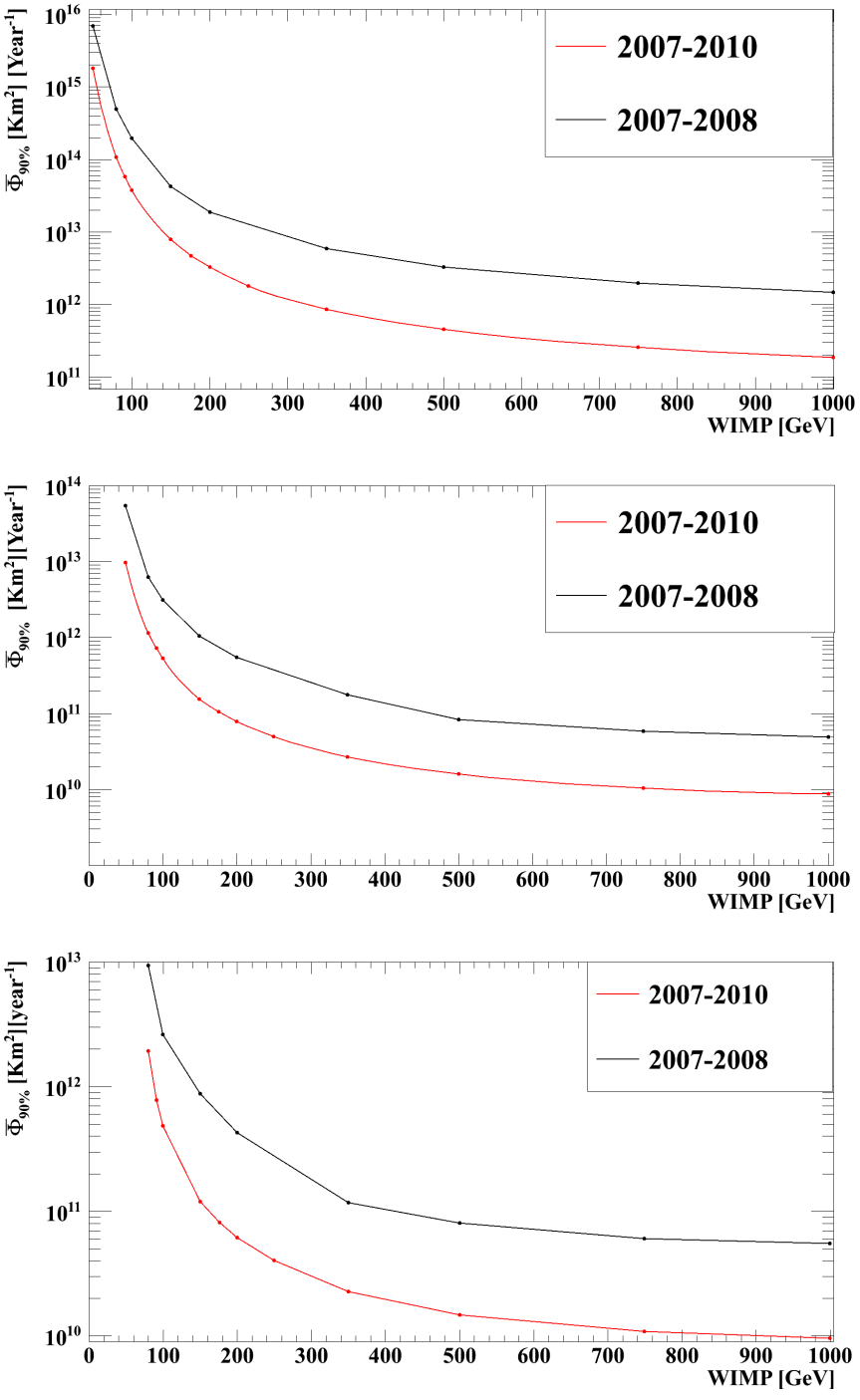

Figure 6.12: Comparison of sensitivities to neutrino flux coming from dark matter annihilation inside the Sun as a function of WIMP mass between the 2007-2008 and 2007-2010 analysis. Top plot is for b^+b^- , middle is for $\tau^+\tau^-$, and the bottom is for W^+W^-.

6.4.2 BBFit Single-line analysis

The single line events in BBFit are events that are reconstructed will all hits happening on one line (nlines = 1). Since every hit on the different OMs in each floor are merged in BBFit the information on the horizontal direction of the muon (azimuth or ϕ) is lost. This present us with a problem, if we have no information on the horizontal direction of the muon then its direction can not be compared to the Sun. For this reason in chapter 5 these events were removed from our data selection with the pre-analysis cut nlines > 1. However, if we take a look at figure 6.13 we can clearly see that for low WIMP masses the ratio of the single line events to multi line events can be as high as 7. The reason for this is that the single line events are dominated by low energy events for which the muon track is short, this is seen with the fact that the soft channel have a higher ratio than the hard channels, and that the lighter the WIMP is the higher the ratio is. However, the reason why the 50 GeV b^+b^- has a smaller ratio than the next WIMP mass (80.3 GeV) or when compared to 50 GeV $\tau^+\tau^-$ is because that spectrum is so soft that a good part of its low energy events falls below our low energy neutrino threshold.

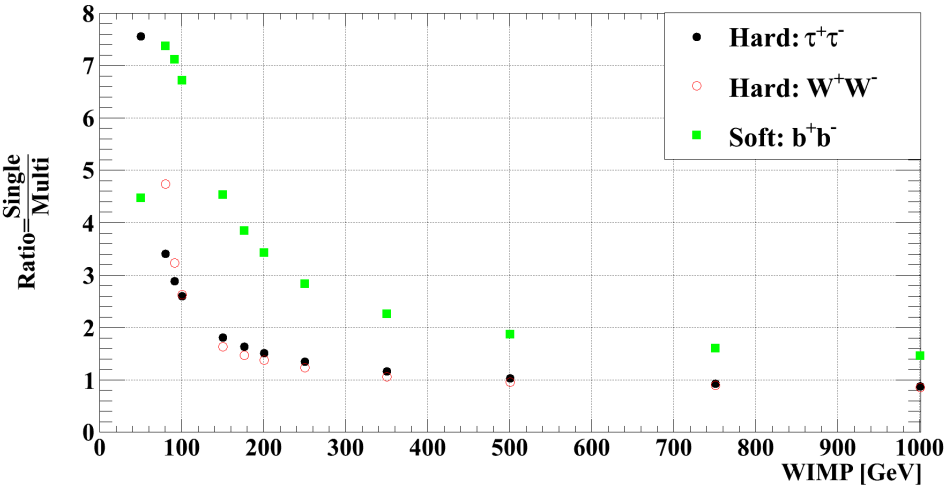

Figure 6.13: The ratio of single line events to multi line events as a function of the the WIMP mass and the annihilation channel. No quality selection cuts were applied here.

Removal of these events is clearly an issue as we are neglecting a large portion of our signal, and if we can use these events we can greatly improve our sensitivities at low WIMP masses. The way to do this is to simply change the definition of $\Delta(\Psi^\circ)$ in the cone search analysis. $\Delta(\Psi^\circ)$ is defined as the half-cone angle be-

tween the direction of the Sun and the direction of the muon. Previously it was calculated as described in equation 6.5 where θ_S and ϕ_S are the zenith and azimuth angle of the Sun, while θ_μ and ϕ_μ are the zenith and azimuth angle of the reconstructed muon. However, in this analysis it will be calculated as an angle between two tracks in a two dimensional plane as we can see in equation 6.6 , so in essence $\Delta(\Psi^\circ)$ becomes $\Delta(\theta)$ the difference between the zenith angle of the Sun and the reconstructed muon.

$$\Delta(\Psi) = \arccos(\sin(\theta_S).\sin(\theta_\mu).\cos(\phi_S - \phi_\mu) + \cos(\theta_S).\cos(\theta_\mu)) \quad (6.5)$$

$$\Delta(\theta) = |\theta_S - \theta_\mu| \quad (6.6)$$

So instead of looking for events inside a cone centered around the Sun, now we would be looking for events that are located in a horizontal band centered around the zenith of the Sun (figure 6.14). Selecting events that occur in horizontal bands has the drawback of presenting us with a higher background when compared to the half-cone angle for the multi line events as we can clearly see in figure 6.15. In the course of this analysis we will investigate whether the sensitivities produced with the single-line analysis are competitive to those with multi-lines analysis and whether they can be used or not to improve our overall sensitivities.

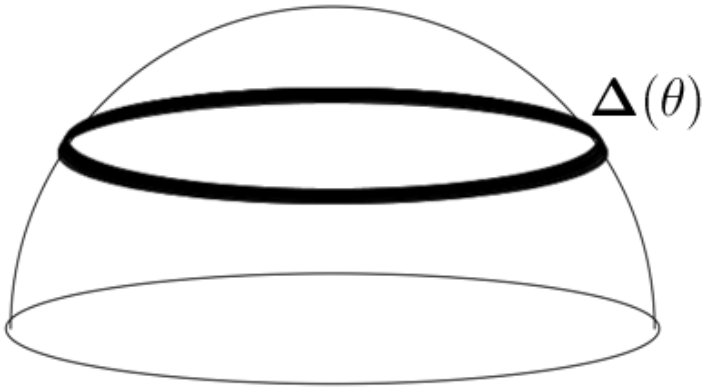

Figure 6.14: A simple diagram showing the region confined by $\Delta(\theta)$.

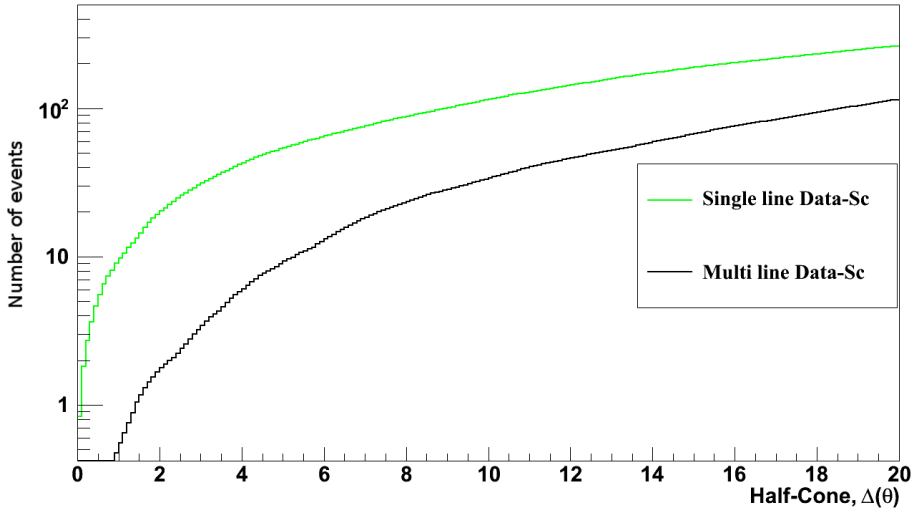

Figure 6.15: Comparison between the estimated background given by scrambled data for the single line events and multi line events in the direction of the Sun as a function of $\Delta(\theta)$ and $\Delta(\Psi)$ for the same χ^2 cut (1.6).

6.4.2.1 Data Monte Carlo comparison

The pre-analysis quality cuts that we apply on BBFit variables are essentially the same as in the multi-line analysis, with small differences:

1. tchi2 < bchi2.
2. nlines = 1
3. $\cos(\theta) > 0$.
4. $\cos(\theta) \neq 1$.

For items (1), and (3) are just the standard pre-analysis cuts that we apply. As for (2) it is obvious that we need events that are reconstructed with one single line. For (4) it is a cut that allows us to remove a significant number of badly reconstructed atmospheric muons before even starting the analysis.
Events with $\cos(\theta) = 1$ are events that are reconstructed as exactly vertical, so cut (4) is applied because if we take a look at the estimated number of atmospheric muons with $\cos(\theta) = 1$ we find it to be at least four orders of magnitude higher than the estimated number of atmospheric neutrinos (figure 6.16), additionally the estimated number of dark matter events is 0. So this cut allows us to lower significantly our background without affecting the signal at all.

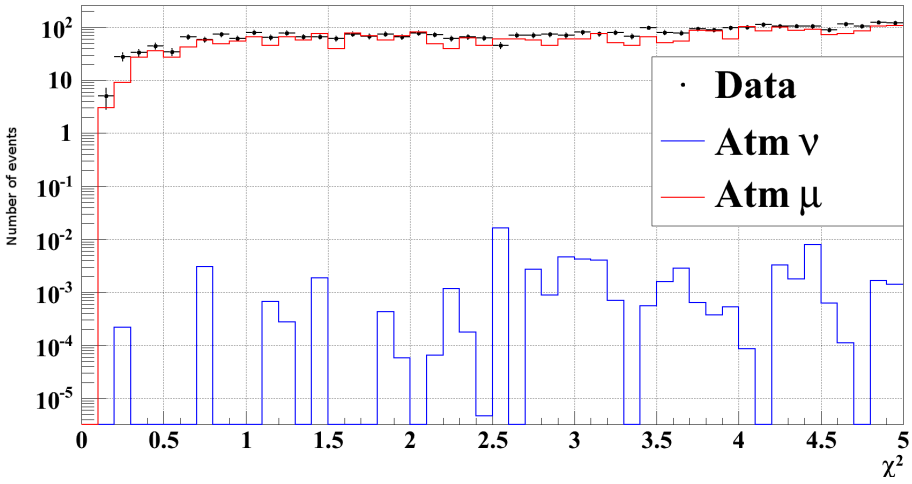

Figure 6.16: Comparison of χ^2 distribution among data, atm$_\nu$, atm$_\mu$ for $\cos(\theta) = 1$. The muon and neutrino Monte Carlo are normalized to the lifetime of the data taking.

Figure 6.17 shows the distribution of the number of hits or Nhit. It might be tempting to apply a cut of Nhit > 7 to remove the large contribution of atm$_\mu$ as other analyzes that use the single line events do (such as neutrino oscillations[111]), additionally this cut can help us separate atm$_\nu$ from atm$_\mu$ as seen in figure 6.18 where can clearly see its effect on the separation of the atm$_\nu$ and atm$_\mu$, without it, it is difficult to have a reasonable χ^2 cut that can separate the two. However, by applying this cut, we would be removing 86% of our signal in the case of dark matter spectrum of 50 GeV b^+b^- and 61% in the case of 1000 GeV $\tau^+\tau^-$. Additionally quick tests on the its effect on the eventual sensitivities were explored. Applying Nhit > 7 (or Nhit < 6 and Nhit < 5) gives us a worse sensitivities when compared to no cut. In the end we would be sacrificing the purity of our data sample (higher contribution of atm$_\mu$) in exchange for better sensitivities.

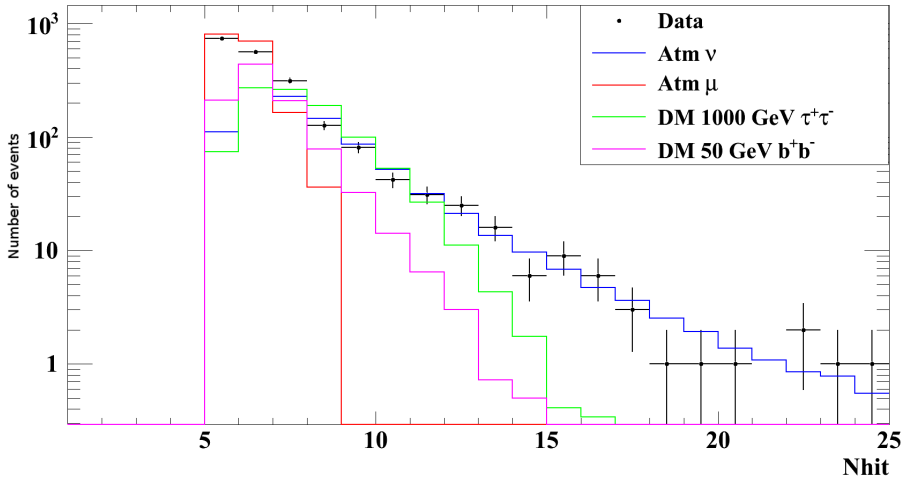

Figure 6.17: Comparison of Nhit distribution among data, atm$_\nu$, atm$_\mu$, and two dark matter spectra. The dark matter spectra were normalized to number of events of atm$_\nu$ to emphasize the shape of the distribution. The muon and neutrino Monte Carlo are normalized to the lifetime of the data taking.

6.4.2.2 Background estimation

The background estimation will follow the same procedure described in 6.4.1.2. However, the estimation of the background in the direction of the Sun is done as previously stated with the $\Delta(\theta)$ variable. Figure 6.19 shows a comparison of the estimated background in the direction of the Sun among the scrambled data, and Monte Carlo (atm$_\nu$ & atm$_\mu$). The plots shows a very good agreement between the scrambled data and the estimation from the Monte Carlo, this is in a way a reflection of the very good Data Monte Carlo agreement we see in section 6.18

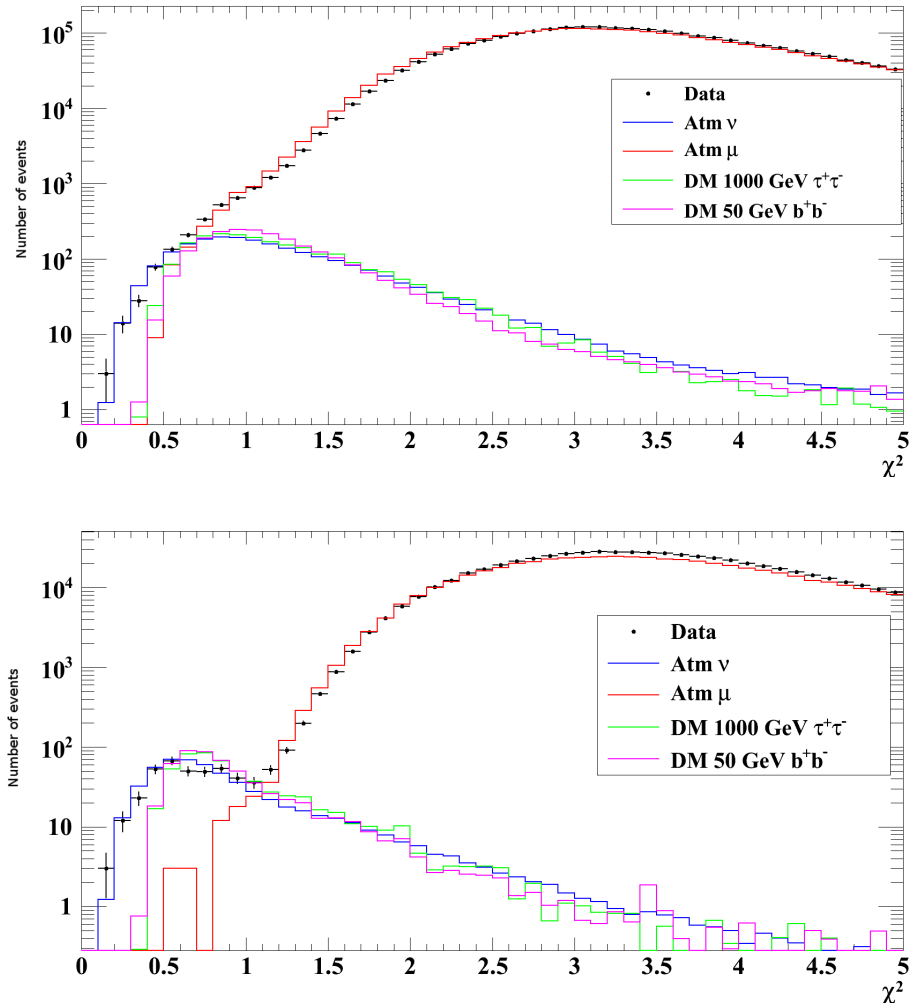

Figure 6.18: Comparison of χ^2 distribution among data, atm$_\nu$, atm$_\mu$, and two dark matter spectra. The dark matter spectra were normalized to number of events of atm$_\nu$ to emphasize the shape of the distribution. The upper plot is without Nhit>7 , while the lower is with this cut. The muon and neutrino Monte Carlo are normalized to the lifetime of the data taking.

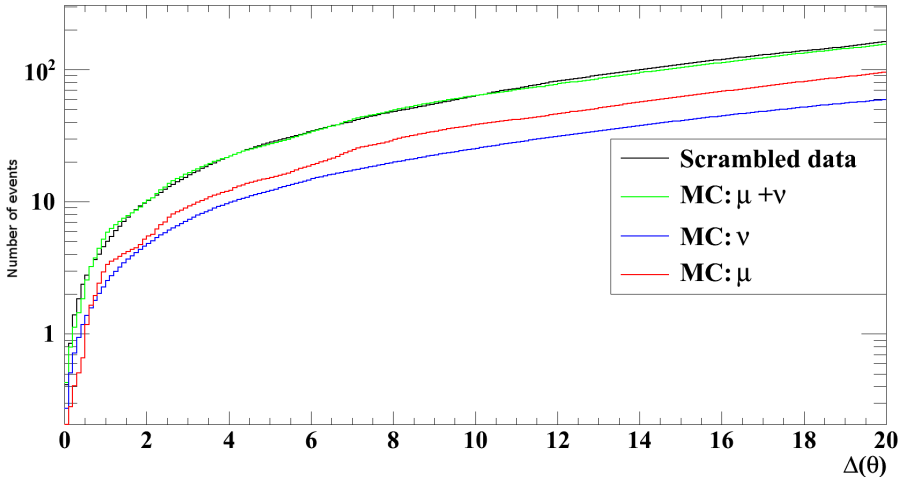

Figure 6.19: The estimation of the background in the direction of the Sun as a function of $\Delta(\theta)$. The scrambled data in addition to the MC are presented here. A cut of $\chi^2 < 0.9$ was applied here.

6.4.2.3 Search variables and optimization

The search variables that will be used in this analysis are still the same that were used before (with the substitution of $\Delta(\Psi)$ by $\Delta(\theta)$). In addition, this time a new cut based on Nhit is going to be introduced in the analysis. However, we will not use Nhit as an optimized cut, the optimization will follow as before with slight variation:

- χ^2 focus region is going to be between 0.7 and 1.2 .
- $\Delta(\theta)$ focus region will be between 0° and 20°.
- For each χ^2 cut and dark matter model calculate $Nhit_{max}$ which the value of maximum value of the Nhit variable for the specific dark matter model.
- Apply χ^2 & $Nhit_{max}$ cut on the scrambled data and then proceed to estimate the background in the direction of the Sun.
- Search for the optimal $\Delta(\theta)$ cut for the optimal value of $\bar{\Phi}_{90\%}$.
- Repeat the process for the entire focus region of χ^2, and then select the best value of all optimal values of $\bar{\Phi}_{90\%}$.

The use of $Nhit_{max}$ is tailored specifically for low mass WIMPs as they are produce low energy neutrinos which in turn leave a lower number of hits on the detector.

The good data-MC agreement in figure 6.17 allows us to use $Nhit_{max}$ as a cut in this analysis. The low mass WIMPs are as well the target of this analysis since figure 6.13 showed us that the best use of the single line events is to improve the sensitivities of the low mass WIMPs.
As in the multi-lines section or the previous analysis, a single χ^2 cut was found for all the dark matter models as a result of the similarity of the χ^2 distribution shape. This cut is $\chi^2 < 0.9$. additionally figure 6.21 shows the value of the optimized $\Delta(\theta)$ cuts, and again we see exactly what we expected: larger cuts on softer and lighter WIMPs models and smaller on harder and heavier WIMPs models. The typical value for the $Nhit_{max}$ that we find during this analysis is between 12 and 18. Note that for heavy WIMPs this applying this cut does not affect the resulting sensitivities.

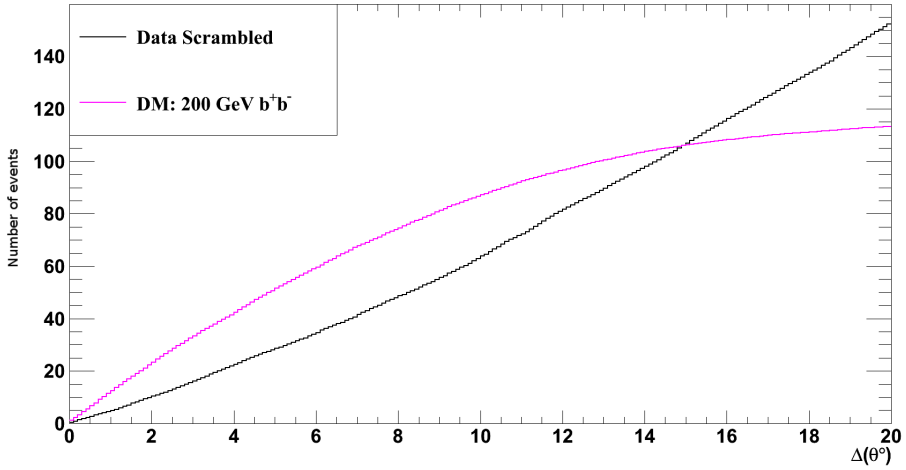

Figure 6.20: Comparison of the estimated background in the direction of the Sun from scrambled data and one dark matter model (200 GeV b^+b^-). χ^2<0.9 and $Nhit_{max} = 14$.

Figure 6.20 shows a comparison of the estimated background from scrambled data and one dark matter model (200 GeV b^+b^-). It is interesting to note that in the multi-line analysis for small $\Delta(\Psi)$ the background is compatible with a random distribution of events $N_{events} \propto \Delta(\Psi)^2$, but in the case of single-line the background is still compatible with a random distribution of events but $N_{events} \propto \theta$. The reason for this is that in the case of multi-line analysis the random distribution of events is in a 2D plane (θ, ϕ) while in single-line analysis it is in a 1D plane (θ).

The resulting sensitivities can be seen in figure 6.22, additional commentary on the results and comparison to the multi-line analysis will be discussed in the next section.

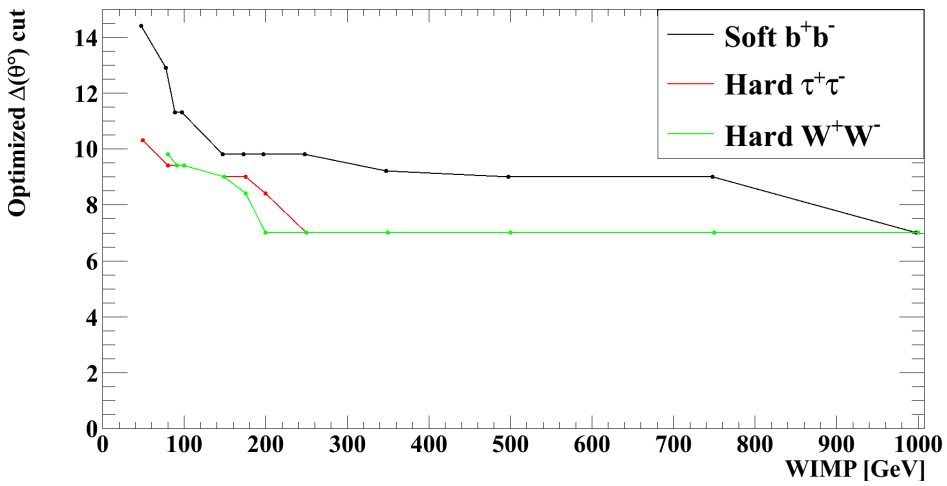

Figure 6.21: Comparison of the optimized $\Delta(\theta^\circ)$ cut as a function of the WIMP mass and the annihilation channel .

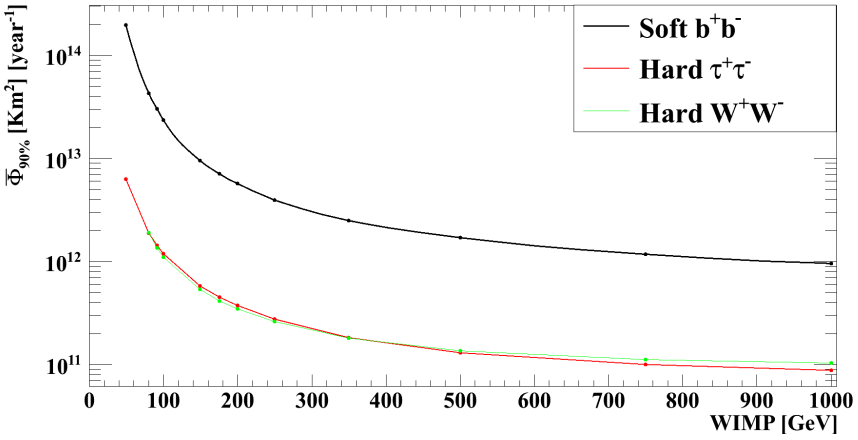

Figure 6.22: Sensitivity to neutrino flux coming from dark matter annihilation inside the Sun as a function of WIMP mass and the annihilation channel for the BBFit single-line analysis.

6.4.3 Single & Multi line combined analysis

In this section we will discuss the comparison of the single and multi line analyzes and their combination method.

6.4.3.1 Single Vs Multi line comparison

Figures 6.23 & 6.24 show us the comparison among the different sensitivities we get from both analyzes. As predicted we can see the best improvement to our sensitivities we get is for low WIMP masses with b^+b^- as the annihilation channel with single-line sensitivity being almost an order of magnitude better. At the other end of dark matter models, the limits obtained by multi-lines from 1000 GeV hard channels (W and τ) are this time an order of magnitude better than their single-line equivalent. While we understand why at low WIMP masses we get almost an order of magnitude better sensitivity, we need to explain those with harder spectra at high mass. If we remember figure 6.13 at high WIMP masses we get as much multi-lines event as single-line, so they must get sensitivities of equal order. However, the reason with this discrepancy has to do with the expected background. For multi-lines 1000 GeV $\tau^+\tau^-$ the optimal cuts for (χ^2 , $\Delta(\Psi)$) are (1.6 , 2.7°) which yields an expected background of 2.6 events, while in the case of single-line with (0.9 , 7°) as optimized (χ^2 , $\Delta(\theta)$) they yield an expected background of 40 events. $\bar{\mu}_{90\%}$ in the case of 2.6 events is about 4.224 while in the case of 40 events it is 12.586. For this reason if we assume that at their respective cuts we still have the same number of signal events between the multi-lines and single-line[2] we would expect that the sensitives with multi-lines to be at least 3 times better than those with single-lines.

[2]Which is not true as we have more multi-lines events after cuts in this specific case

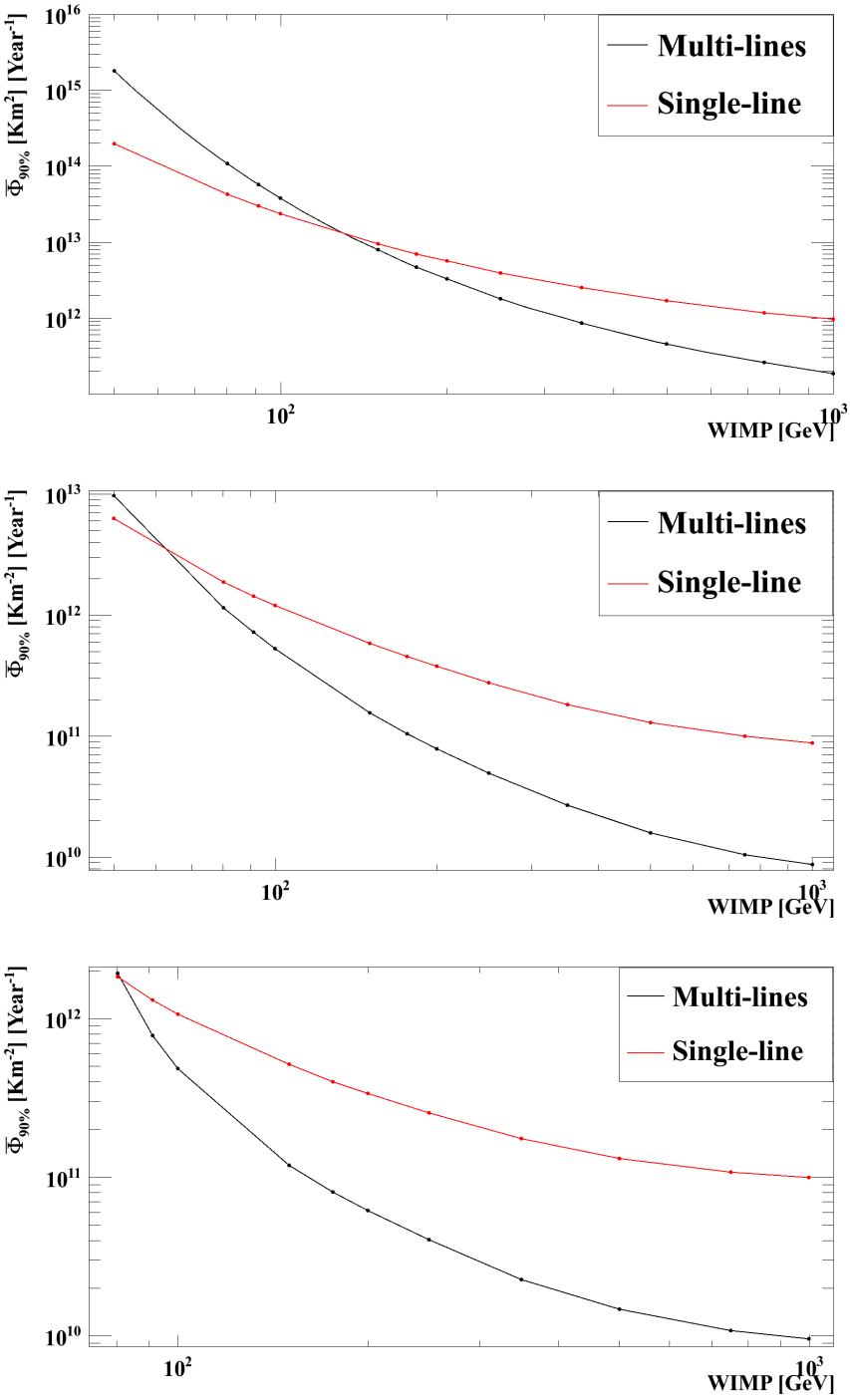

Figure 6.23: Comparison of sensitivities to neutrino flux coming from dark matter annihilation inside the Sun as a function of WIMP mass and the annihilation channel between multi-lines and single-line BBFit analysis .Top plot is for the soft b^+b^-, middle is for $\tau^+\tau^-$, while to bottom is for W^+W^-.

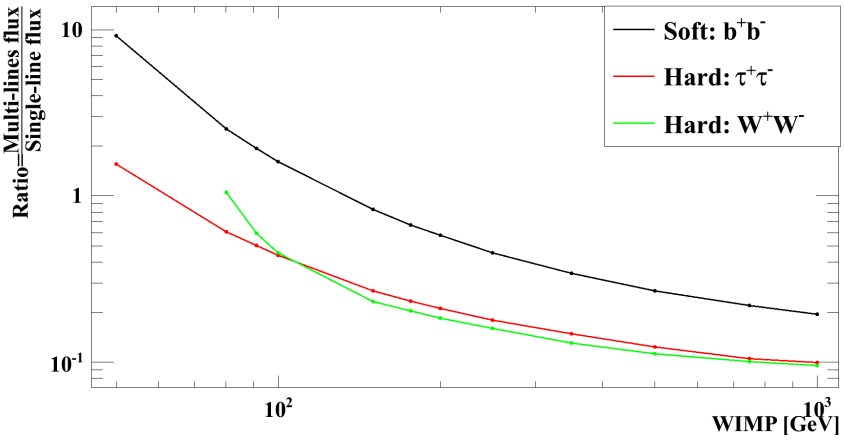

Figure 6.24: Ratio of multi-lines neutrino flux to single-lines flux from figure 6.23 as a function of WIMP mass.

6.4.3.2 Dual Optimization

The data sets used by the multi-lines and single-line analysis are a none overlapping data sets, this should allows to directly combine the sensitivities produced by the two analyzes to improve them. However, we will not just use the already optimized sensitivities and combine them (by summing the signal, the background, and then calculate $\bar{\Phi}_{90\%}$). What we will do is re-do the optimization as following:

1. Fix the χ^2_{multi} cut at a value in its focus region (1.2 , 2).
2. Fix the χ^2_{single} cut at a value in its focus region (0.7 , 1.2).
3. For the χ^2_{single} cut, calculate the corresponding $Nhit_{max}$ for a dark matter model single-line signal distribution and apply it to the single-line data set.
4. With these cuts we can estimate on a 2-D plane as a function of $\Delta(\Psi)$ & $\Delta(\theta)$ the background in the direction of the Sun (figure 6.25) and the signal (figure 6.26).
5. Using figures 6.25 & 6.26 we can calculate again on a 2-D plane $\bar{\Phi}_{90\%}$ (figure 6.27).
6. From figure 6.27 the optimal values of $\Delta(\Psi)$ & $\Delta(\theta)$ can be found that correspond to best value of $\bar{\Phi}_{90\%}$.
7. Process is then repeated for all possible values of (χ^2_{multi} , χ^2_{single}).

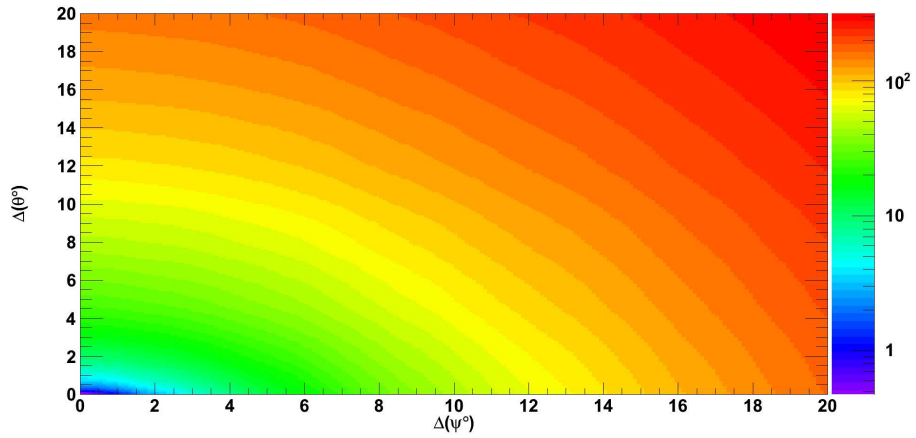

Figure 6.25: Estimation of our background in the direction of the Sun as a function of $\Delta(\Psi)$ & $\Delta(\theta)$. The cuts used χ^2_{multi}<1.6 , χ^2_{single} < 0.8

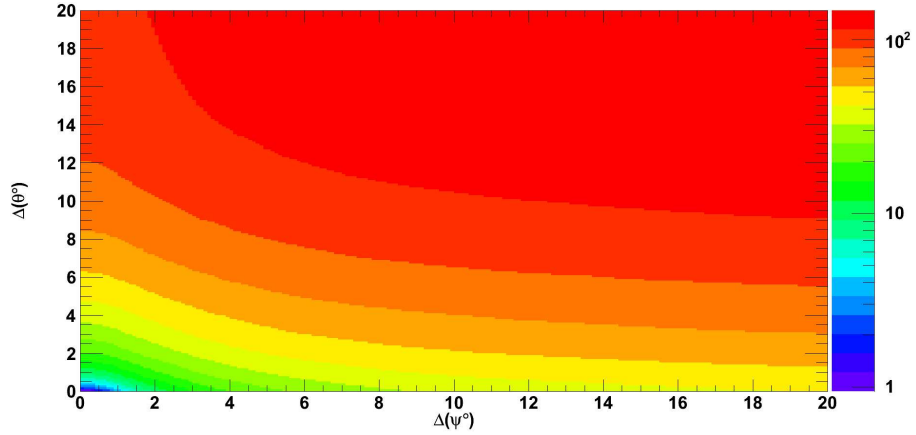

Figure 6.26: Estimation of the signal of 50 GeV $\tau^+\tau^-$ dark matter model as a function of $\Delta(\Psi)$ & $\Delta(\theta)$. The cuts used χ^2_{multi}<1.6 , χ^2_{single} < 0.8

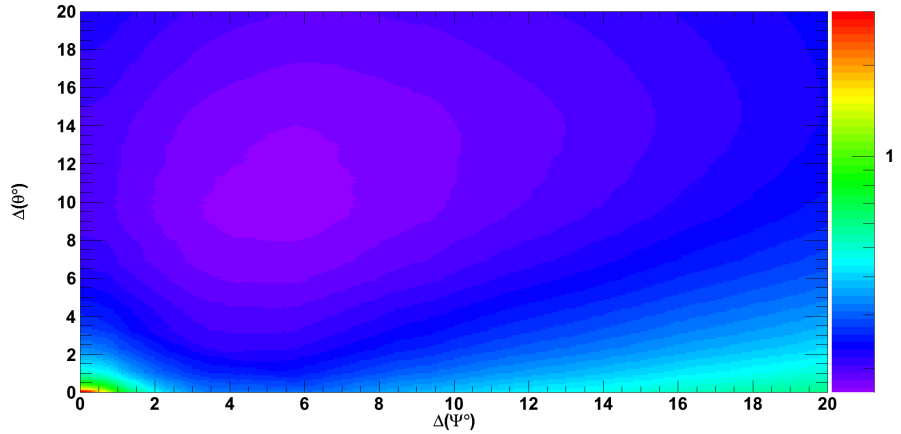

Figure 6.27: Distribution of $\bar{\Phi}_{90\%}$ $[cm^{-2}][s^{-1}]$ for 50 GeV $\tau^+\tau^-$ dark matter model as a function of $\Delta(\Psi)$ & $\Delta(\theta)$. The cuts used χ^2_{multi}<1.6 , $\chi^2_{single} < 0.8$

For spectra where the sensitivity by one analysis dominates the other (ex : a factor ten difference) like 50 GeV b^+b^- or 1000 GeVW^+W^- (among others), we find again using the optimization process described above, the same χ^2 and $\Delta(\Psi)$ or $\Delta(\theta)$ cuts again. However, for models with similar sensitivities such as 80.3 GeV $\tau^+\tau^-$ (among others) we end up with cuts on χ^2_{multi}, χ^2_{single}, $\Delta(\Psi)$, and $\Delta(\theta)$ that are different from the ones we had in the two previous sections. For example previously we had $\chi^2_{multi} < 1.6$, $\Delta(\Psi) < 5.5^\circ$, $\chi^2_{single} < 0.9$, and $\Delta(\Psi) < 12.9^\circ$ for the 80.3 GeV $\tau^+\tau^-$ dark matter model. While in the dual optimization method we find: $\chi^2_{multi} < 1.7$, $\Delta(\Psi) < 5.6^\circ$, $\chi^2_{single} < 0.8$, and $\Delta(\Psi) < 7^\circ$.
Figure 6.28 shows a comparison among the sensitivities of multi-lines, single-line and combined analyzes. The soft channel is the channel that is most affected by the inclusion of the single-line data set. For WIMPs masses below 100 GeV the resulting combined analysis is dominated by the single-line sensitivities as clearly presented, the effect of the single-line is still visible at masses below 176 GeV. For larger masses the multi-lines sensitivities dominate again and combining the two samples does not improve upon the already obtained sensitivities. In the case of $\tau^+\tau^-$ the single-line does not dominate at low masses but they do have an effect on WIMPs with a mass of 50 GeV where they improve our sensitivities by a factor of 2. The effect diminishes from 80.3 GeV and heavier WIMPs where the multi-lines sensitivities dominate again. Finally, we have the same effect for the W^+W^- as in the $\tau^+\tau^-$, WIMP models at a mass of 80.3 GeV gain an improvement of a factor 2, but for larger masses (>100 GeV) the multi-lines sensitivities dominate again.

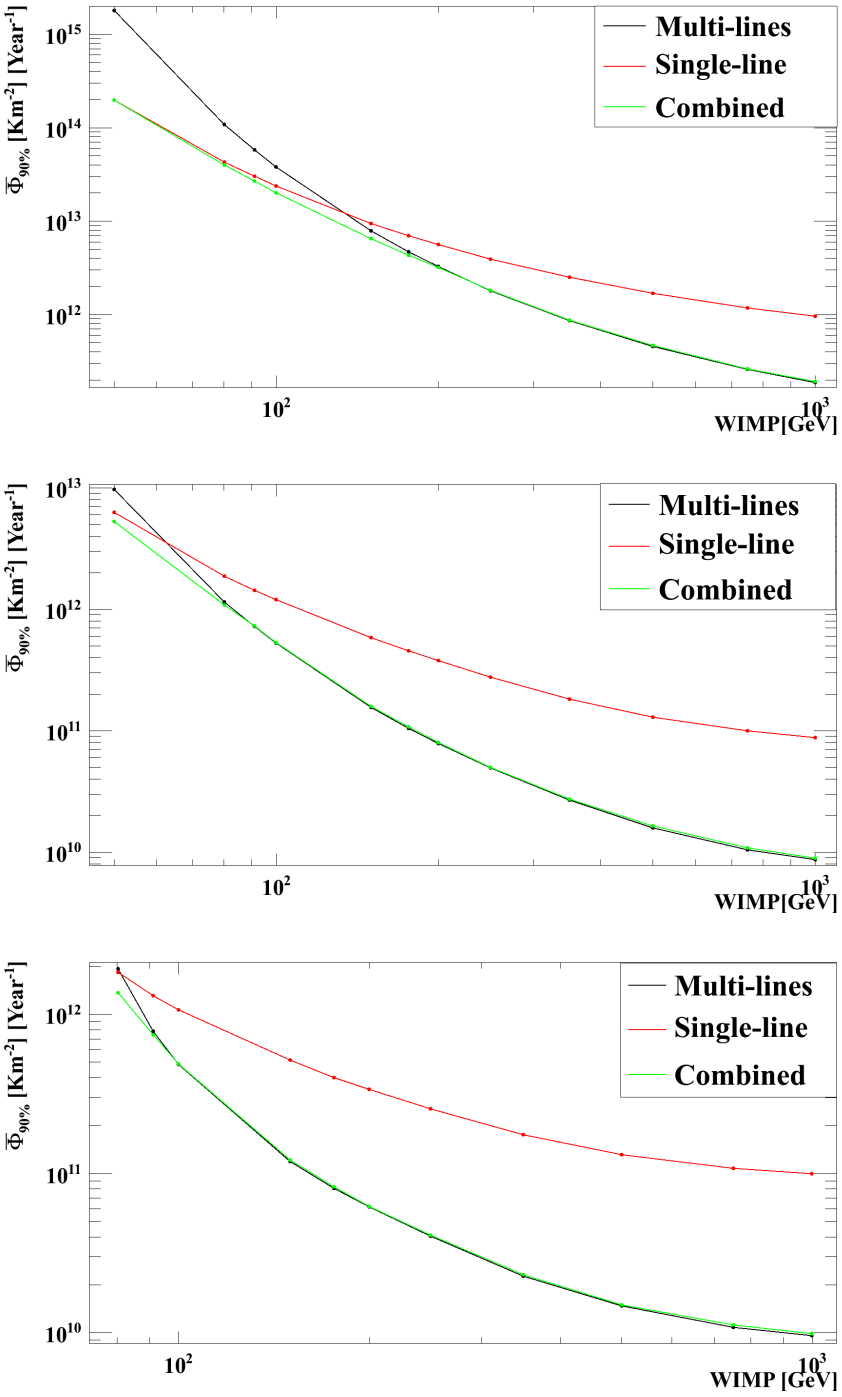

Figure 6.28: Comparison of the multi-lines, single-line and combined sensitivities to neutrino flux coming from dark matter annihilation inside the Sun as a function of WIMP mass and the annihilation channel. Top plot is for the soft b^+b^-, middle is for $\tau^+\tau^-$, while to bottom is for W^+W^-.

6.5 Dark matter search with AAFit reconstruction strategy

In this section we will discuss the analysis using the AAFit reconstruction strategy.

6.5.1 Data Monte Carlo comparison

Similarly to the two previous analyzes, before going on with our analysis we should first test our data Monte Carlo agreement. In this case no set of preliminary cuts are proposed, so we will go right ahead with the comparison.
Figure 6.29 shows us the Λ distribution of data, our MC (atm_μ & atm_ν) and two dark matter models which have been normalized to the number of events of atm_ν. The agreement between data and atm_ν is good for values of $\Lambda >$ -5 (larger values of Λ indicates a good fit), in addition we can see that the agreement between atm_μ for $\lambda >$ -6.5 is very good as well. However, for values smaller than -6.5 we see we have a bad data Monte Carlo agreement in the region where the lambda reflects a bad fit on the muon track. Additionally, we can notice that in contrary to the χ^2 variable in BBFit where we saw the dark matter models behave similarly to atm_ν here with Λ variable this is not the case. The model 50 GeV b^+b^- seems to have a the larger portion of its events in the small values of Λ when compared to atm_ν while 1000 GeV $\tau^+\tau^-$ on the other hand seem to have more its events in the large values of Λ when compared to atm_ν.

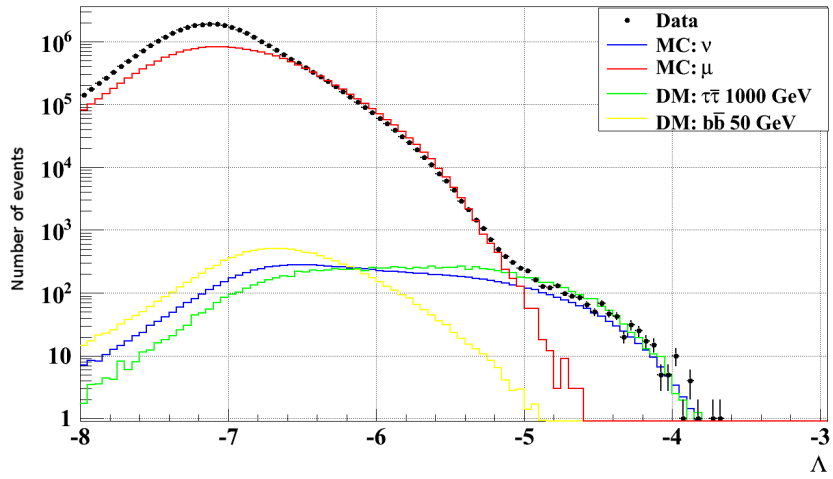

Figure 6.29: Comparison of the Λ distribution of data, MC: atm$_\mu$ and atm$_\nu$, and two dark matter models (50 GeV b^+b^- & 1000 GeV $\tau^+\tau^-$) which were normalized to the number of events of atm$_\nu$. The muon and neutrino Monte Carlo are normalized to the lifetime of the data taking.

Figure 6.30 present us the Nhit distribution with a cut of Λ >-5.6 . Here we find a very good agreement between data and our background Monte Carlo as a direct consequence of the good agreement we saw in 6.29 for high values. However, the interesting part of this distribution is the behavior of the two dark matter models we used an example. The 1000 GeV $\tau^+\tau^-$ model seems to behave for most part (up to Nhit <60) as atm$_\nu$, but the 50 GeV b^+b^- model behaves in a completely different way, the peak of the distribution is on a lower value 20 hits (low energy events → less hits), in addition there is no events for Nhit > 40. In consequence we can use Nhit as a discriminating variable as we did in the BBFit single-line analysis. However, the effect of a $Nhit_{max}$ cut will only be significant on lighter WIMPs with softer spectra.

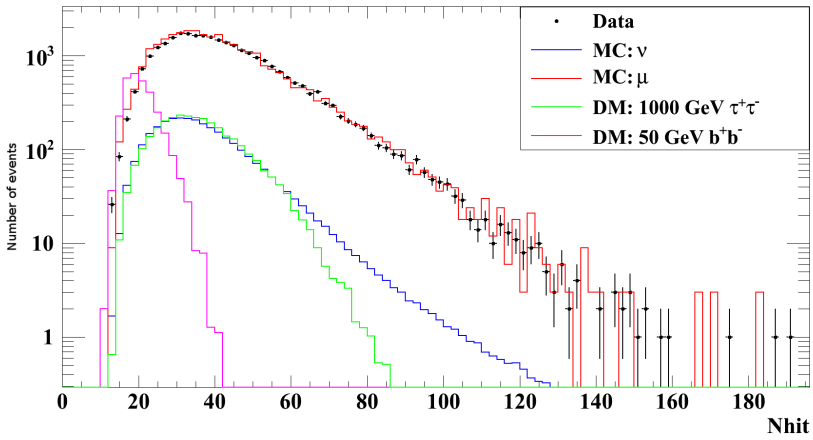

Figure 6.30: Comparison of the Nhit distribution of data, MC: atm$_\mu$&atm_ν, and two dark matter models (50 GeV b^+b^- & 1000 GeV $\tau^+\tau^-$) which were normalized to the number of events of atm$_\nu$. A cut of Λ >-5.6 was applied here. The muon and neutrino Monte Carlo are normalized to the lifetime of the data taking.XS

In figure 6.31 we can see the distribution of $\cos(\theta)$ with a cut of Λ >-5.6 . Again the agreement is pretty good between data and our background MC, the loose cut of Λ ensures that atm$_\mu$ dominates our data sample.
Finally in figure 6.32 we can see the distribution of β. This variable is an estimation on the uncertainty on the direction of the reconstructed muon. This variable is a good separator of atm$_\nu$ from atm$_\mu$. However, we can see that the distribution of this variable changes as a function of the dark matter model as well. Heavier WIMPs who have harder spectra seem to peak higher and drops quicker when compared to lighter WIMPs with softer spectra (1000 GeV $\tau^+\tau^-$ Vs. 50 GeV b^+b^-). We would expect when β is used in the optimization process to play the role of another discriminator between background and signal (in addition to Nhit and $\Delta(\psi)$) and heavier WIMPs would have a tighter cut on β when compared to lighter ones, and the same with harder when compared with softer spectra.

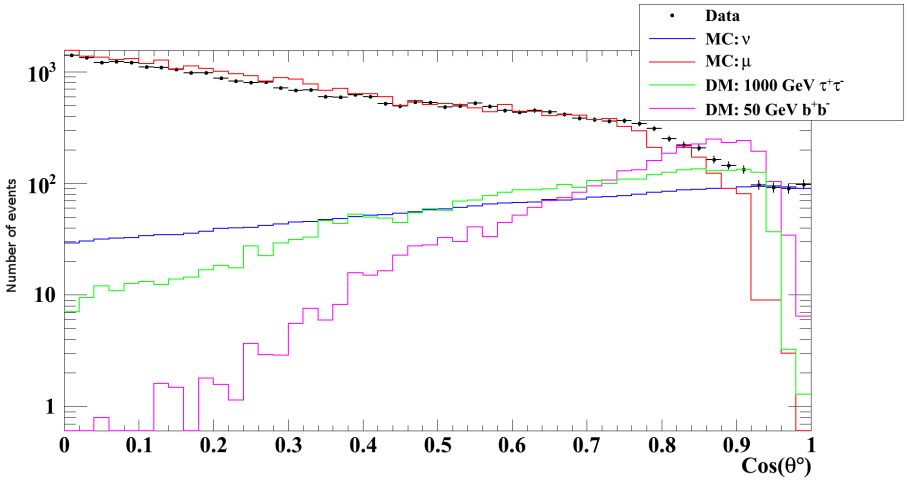

Figure 6.31: Comparison of the $\cos(\theta)$ distribution of data, MC: atm_μ & atm_ν, and two dark matter models (50 GeV b^+b^- & 1000 GeV $\tau^+\tau^-$) which were normalized to the number of events of atm_ν. A cut of Λ >-5.6 was applied here. The muon and neutrino Monte Carlo are normalized to the lifetime of the data taking.

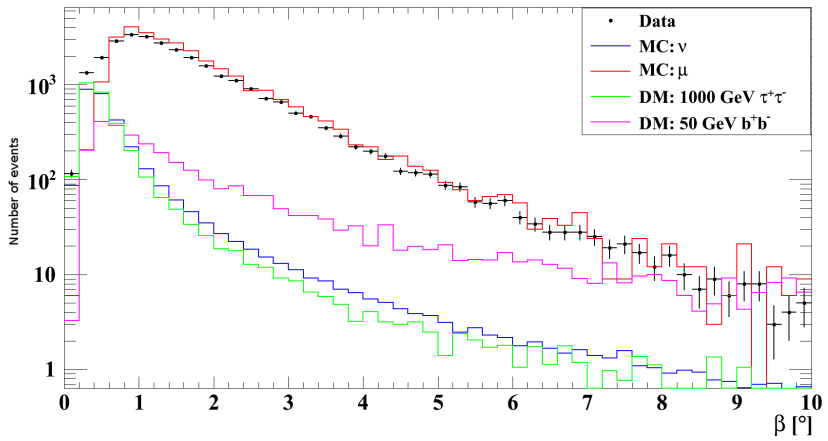

Figure 6.32: Comparison of the β distribution of data, MC: atm_μ & atm_ν, and two dark matter models (50 GeV b^+b^- & 1000 GeV $\tau^+\tau^-$) which were normalized to the number of events of atm_ν. A cut of Λ >-5.6 was applied here. The muon and neutrino Monte Carlo are normalized to the lifetime of the data taking.

6.5.2 Background estimation

As previously established, the estimation of the background in the direction of the Sun is made with $\Delta(\Psi)$ as we can see in figure 6.33. While the agreement between scrambled data and the background MC is good, we are overwhelmingly dominated by atm$_\mu$ as we are applying a loose cut on Λ and no cut on β. In figure 6.34 we can see the same distribution with the same Λ cut, but with $\beta < 1^\circ$. With β cut we are still dominated by atm$_\mu$ but the difference went down from one order of magnitude to a factor 3 while barely cutting any atm$_\nu$ events.

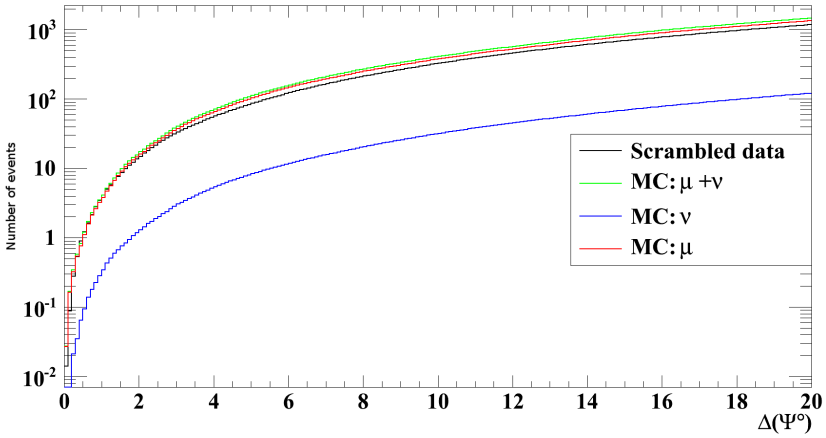

Figure 6.33: Comparison of the estimated background in the direction of the Sun from scrambled data and from background Monte Carlo (ν & μ. $\Lambda >$ -5.6 and no cut on β).

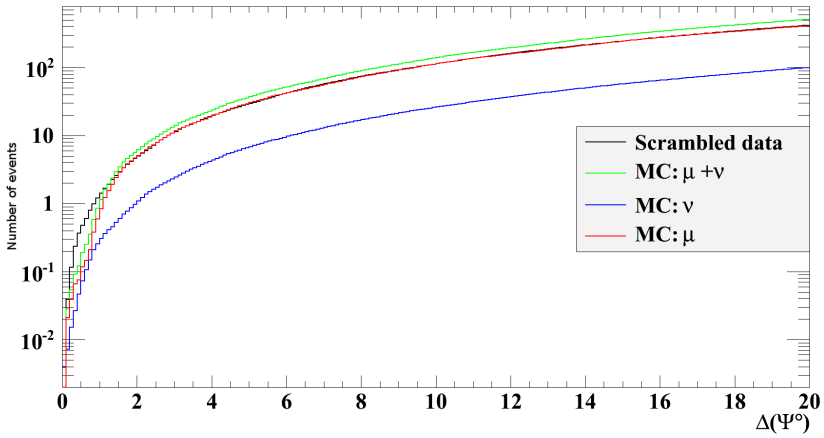

Figure 6.34: Comparison of the estimated background in the direction of the Sun from scrambled data and from background Monte Carlo (ν & μ. $\Lambda >$ -5.6 and $\beta < 1^\circ$).

6.5.3 Search variables and optimization

In addition to Λ and $\Delta(\Psi)$ variables, for the optimization process we will use the two variables $Nhit_{max}$ and β to improve our sensitivities. The Λ focus region will be [-6,-5], $\Delta(\Psi)$ [0°,10°], and for β [0.4°,1.3°]. As for $Nhit_{max}$ it will be used exactly as we did in the single-line BBFit analysis. The optimization process will be as following:

1. Fix Λ in its focus region.
2. Fix β in its focus region.
3. Extract $Nhit_{max}$ which corresponds to the maximum number of hits a specific dark matter model has.
4. Apply $Nhit_{max}$ in addition to the Λ and β cut to the data set.
5. Estimate the background and the signal in the direction of the Sun using $\Delta(\Psi)$ variable (figure 6.35).
6. Using (figure 6.35) calculate $\bar{\Phi}_{90\%}$ as a function of $\Delta(\Psi)$ (figure 6.36) and find the optimal value.
7. Iterate this process over the whole Λ and β focus region and extract best optimal $\bar{\Phi}_{90\%}$.

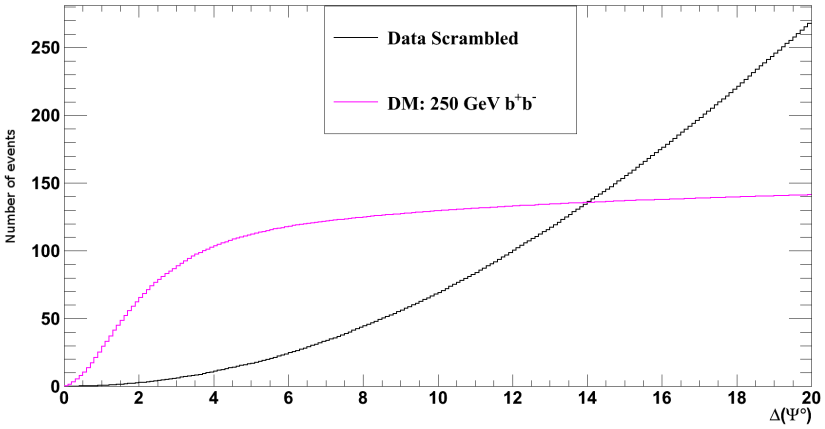

Figure 6.35: Comparison of the estimated background in the direction of the Sun from scrambled data and a dark matter model of 250 GeV b^+b^-. Following cuts were applied: $\Lambda >$ -5.6, $\beta < 0.8^\circ$, and $Nhit_{max} = 74$.

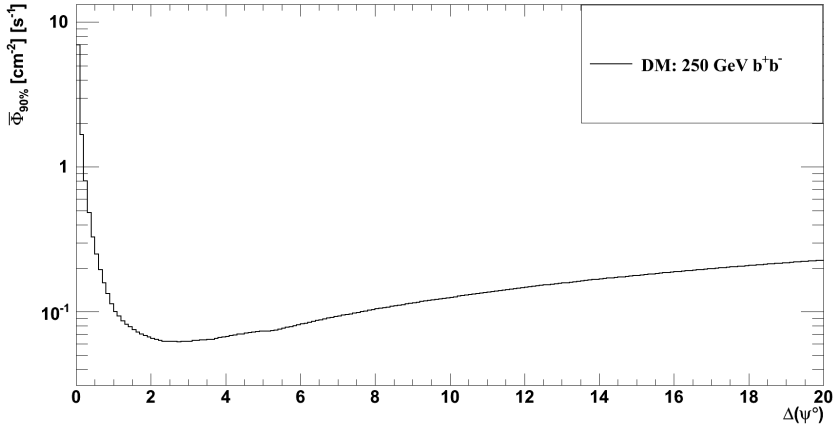

Figure 6.36: Distribution of $\bar{\Phi}_{90\%}$ $[cm^{-2}][s^{-1}]$ for dark matter model of 250 GeV b^+b^- as a function of $\Delta(\Psi)$.Following cuts were applied: $\Lambda >$ -5.6, $\beta < 0.8^\circ$, and $Nhit_{max} = 74$.

The optimal Λ cut for all dark matter models is $\Lambda > -5.6$ (with the exception of 50 GeV b^+b^- with $\Lambda > -5.9$). For $Nhit_{max}$ the range of this is from 50 (lighter WIMPS) to 90 (heavier WIMPs). The β cuts can be seen in figure 6.37. Not a lot of variation can be seen in the value of β cuts, most dark matter models have a cut of $\beta < 0.8^\circ \& \beta < 0.6^\circ$. However, the cut behaves as predicted, larger cuts belong to lighter WIMPs and softer spectra while tighter cuts belong to heavier WIMPs and harder spectra. On a side note, 50 GeV b^+b^- does not converge on a cut for β (value larger than 70°). As for the $\Delta(\Psi)$ optimal cuts we present them

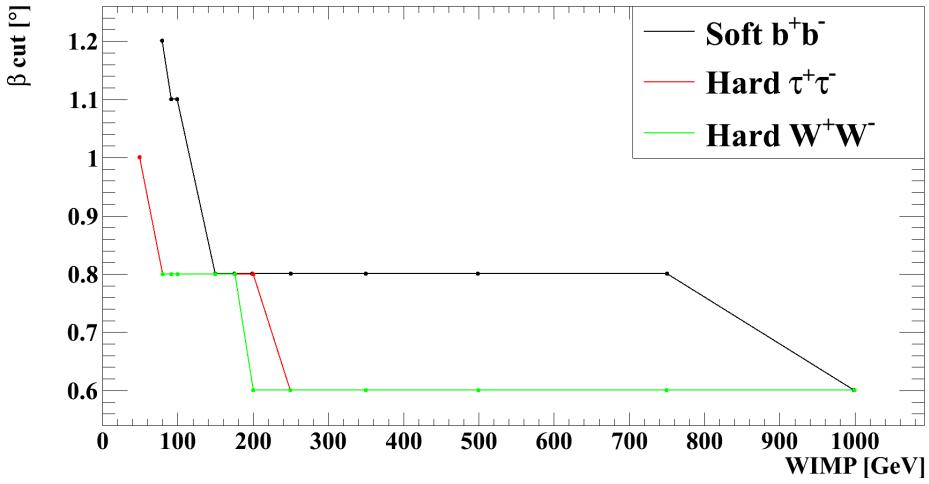

Figure 6.37: Optimal β [°] cuts as a function of WIMP mass and annihilation channel.

in figure 6.38, again we see larger $\Delta(\Psi)$ cuts for lighter WIMPs ($3.5^\circ \sim 4.5^\circ$) and tighter cuts for heavier WIMPs ($1.6^\circ \sim 2.4^\circ$). When these values are compared to those who obtained with BBFit Multi-lines analysis in figure 6.11 we see that for the cuts obtained here are between 1° and 2° tighter. This is due to the fact that the AAFit angular resolution is better than BBFit's angular resolution. This difference can be clearly seen in figure 6.39. This result should be obvious for us, as AAFit's reconstruction strategy is supposed to be more accurate than BBFit (better treatment of the detector and its geometry).

Finally figure 6.40 shows the expected sensitivities to dark matter annihilating in the Sun using AAFit reconstruction strategy. The values presented here are at the same order of magnitude of those obtained with BBFit combined analysis. However, a more detailed comparison will be presented in the following section.

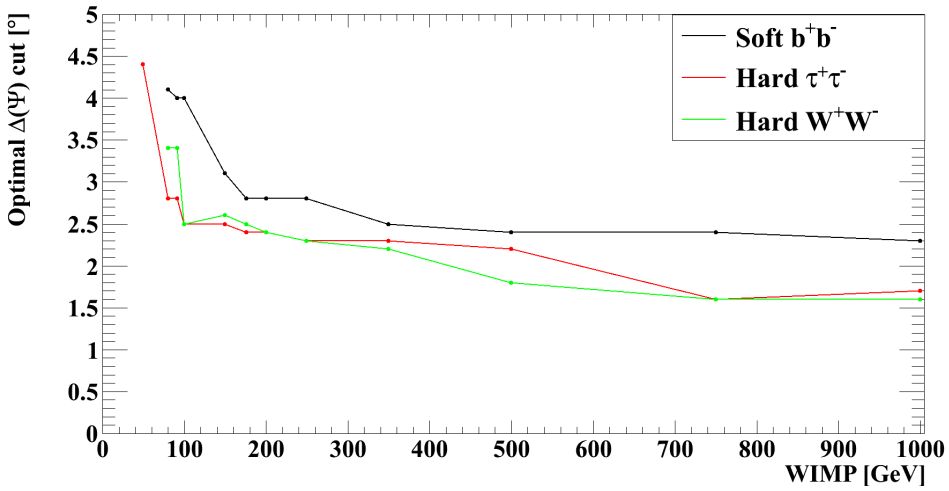

Figure 6.38: Optimal $\Delta(\Psi)$ [°] cuts as a function of WIMP mass and annihilation channel.

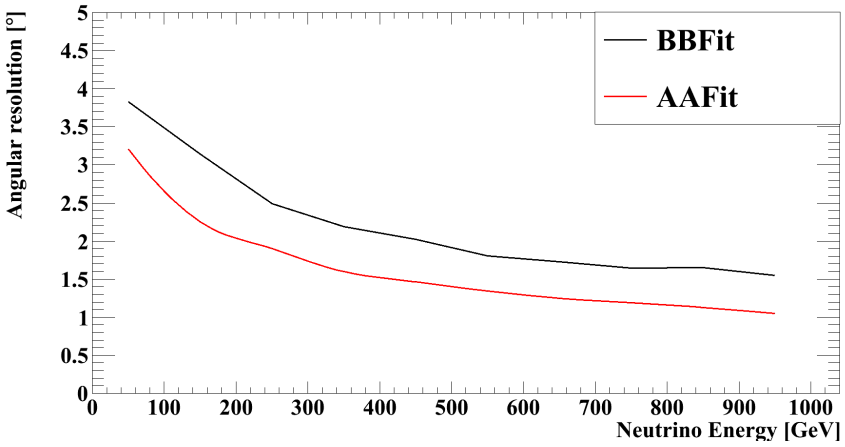

Figure 6.39: Comparison of the mean angle between the neutrino direction and the reconstructed muon direction as a function of neutrino energy.BBFit: $\chi^2 < 1.6$, AAFit: $\Lambda > -5.6$, $\beta < 0.8°$.

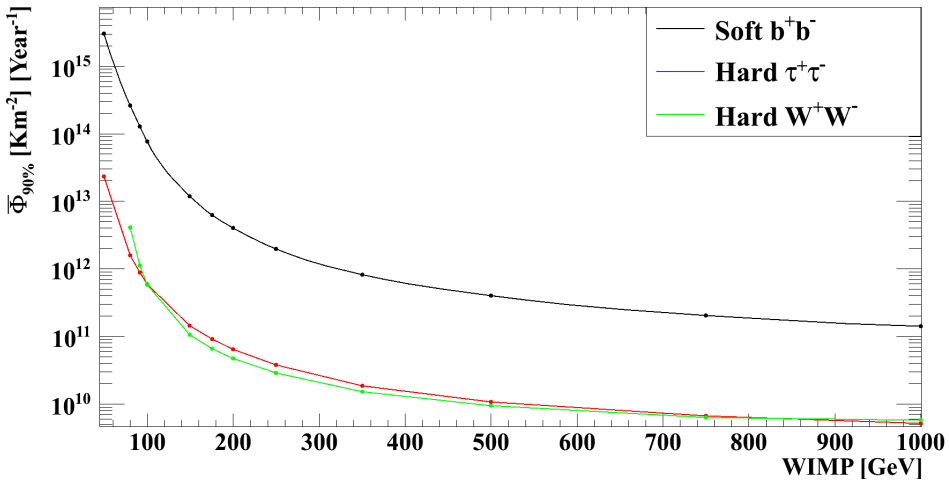

Figure 6.40: Sensitivity to neutrino flux coming from dark matter annihilation inside the Sun as a function of WIMP mass and the annihilation channel for the AAFit analysis.

6.6 Comparison of AAFit & BBFit sensitivities

Comparing the sensitivities is straightforward as we can see in figure 6.41. The first remark we can make is that there is more difference among the sensitivities obtained with AAFit, for example the ratio of 50 GeV and 1000 GeV WIMPS sensitivities for b^+b^- $\tau^+\tau^-$ and W^+W^- are 2.147×10^4, 4.521×10^3 & 7.252×10^2 respectively. While for BBFit they are 1.032×10^3, 5.943×10^2 & 1.378×10^2. So it seem AAFit favors heavier and harder dark matter models while BBFit (combined) favors lighter and softer dark matter models. Additionally this can be seen by the fact that while AAFit has a better angular resolution than BBFit (figure 6.39) BBFit combined analysis outperforms AAFit for WIMP masses up to 350 GeV for the soft spectrum, but for both the two hard spectra ($\tau^+\tau^-$ & W^+W^-) AAFit start to outperforms BBFit around 130 GeV WIMP mass.

Finally, as we can not combine the sensitivities as they are produced using the same data sample, a different strategy can be employed by selecting the BBFit sensitivities for the soft spectrum below 350 GeV and AAFit for larger masses, and for the hard spectra we select BBFit for WIMP masses below 100 GeV and AAFit above that mass.

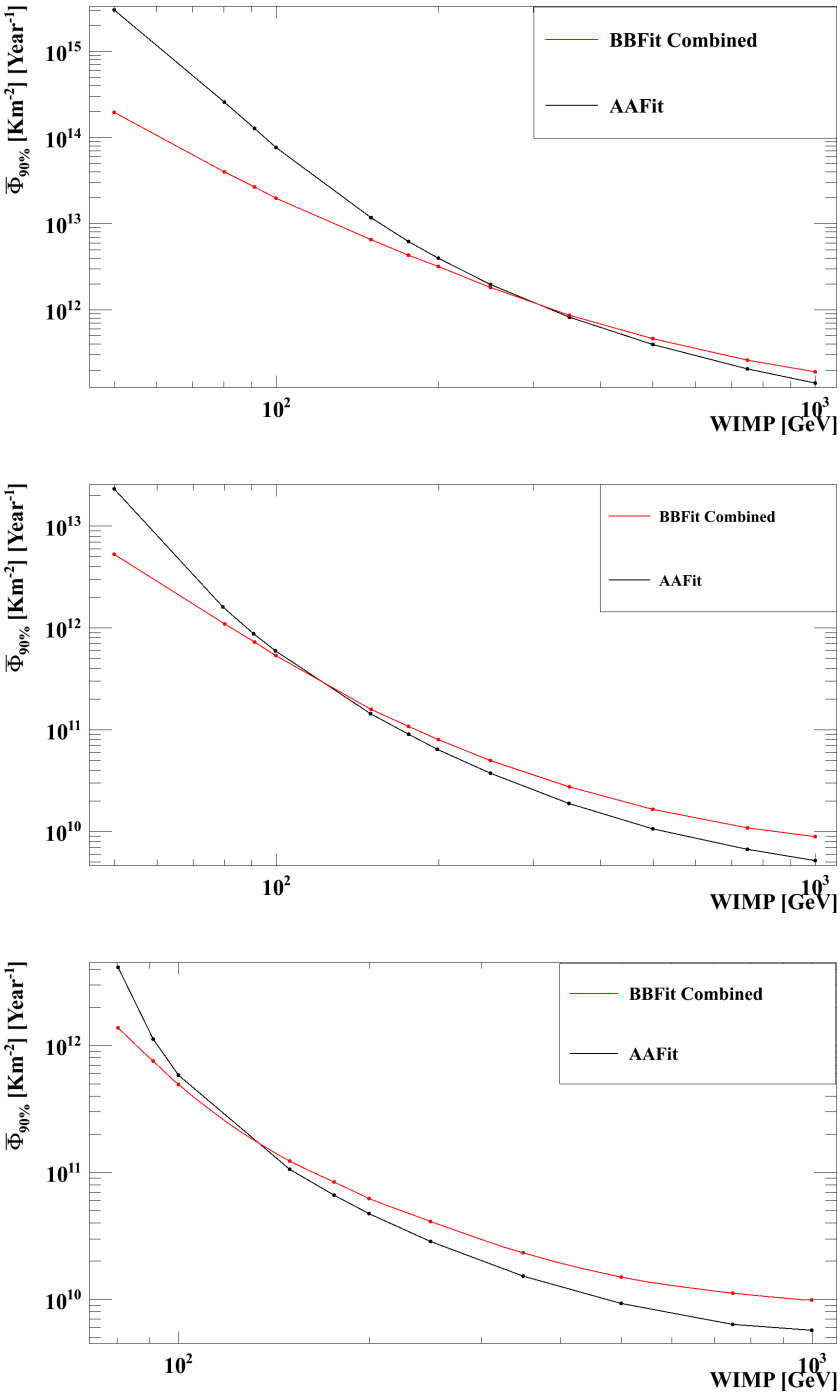

Figure 6.41: Comparison of the BBFit & AAFit analyzes sensitivities to neutrino flux coming from dark matter annihilation inside the Sun as a function of WIMP mass and the annihilation channel. Top plot is for the soft b^+b^-, middle is for $\tau^+\tau^-$, while to bottom is for W^+W^-.

6.7 Comparison with 2007-2008 analysis

While we have provided a comparison between the BBFit multi-lines 2007-2010 sensitivities and the 2007-2008 analysis, we have yet to provide a complete comparison with the BBFit combined analysis along with the results obtained with AAFit.
Figure 6.42 shows us the comparison of the different results for the soft spectrum b^+b^-, at 50 GeV if we use the sensitivities set by BBFit combined analysis we gain about a factor 35 improvement (mostly from the single lines analysis). As for 1000 GeV we have a gain about a factor 10 if we use the results from AAFit.

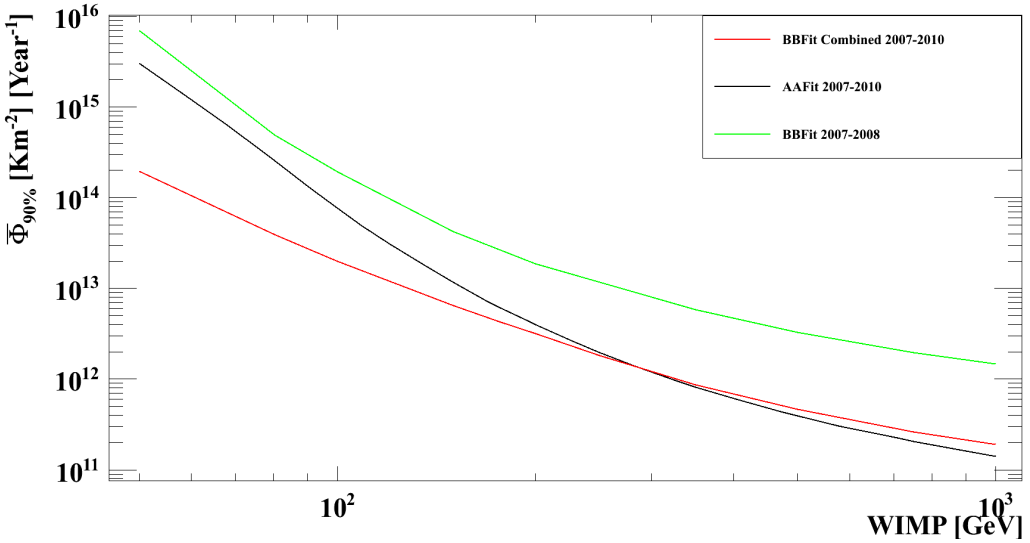

Figure 6.42: Comparison of the sensitivities set by the 2007-2008 analysis (BBFit) and 2007-2010 analysis (BBFit combined and AAFit) for the soft $b\bar{b}$ spectrum.

In figure 6.43 we see the comparison of the results for the hard spectrum $\tau^+\tau^-$, at 50 GeV the sensitivities obtained from BBFit combined analysis gives us an improvement of about a factor 10. As for 1000 GeV if we use AAFit we would gain by factor 9. In figure 6.44 we see the comparison of the results for the hard spectrum W^+W^-, at 80.3 GeV we gain a factor 7 by using BBFit combined analysis, and factor 6 at 1000 GeV if we use AAFit.
And finally figures 6.45 & 6.46 shows us the final sensitivities to the spin-dependent and independent cross-sections. While the improvement we get is visible in the case of spin-dependent, in 2007-2008 analysis (figure 5.32) the limits on spin-dependent could not probe models beyond 250 GeV with the limit set by the $\tau^+\tau^-$ channel. Additionally the lowest cross-section achieved below 250 GeV was at a

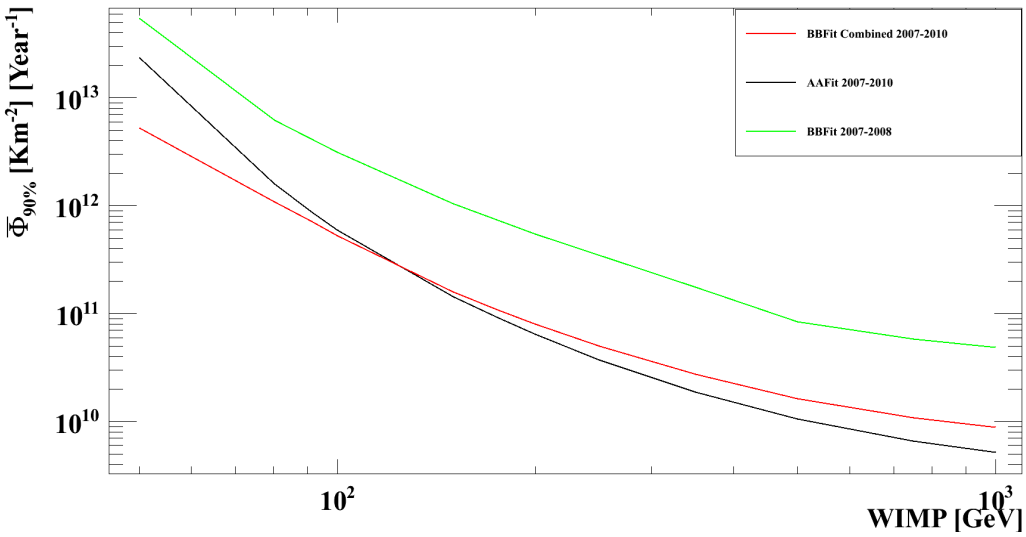

Figure 6.43: Comparison of the sensitivities set by the 2007-2008 analysis (BBFit) and 2007-2010 analysis (BBFit combined and AAFit) for the soft $\tau^+\tau^-$ spectrum.

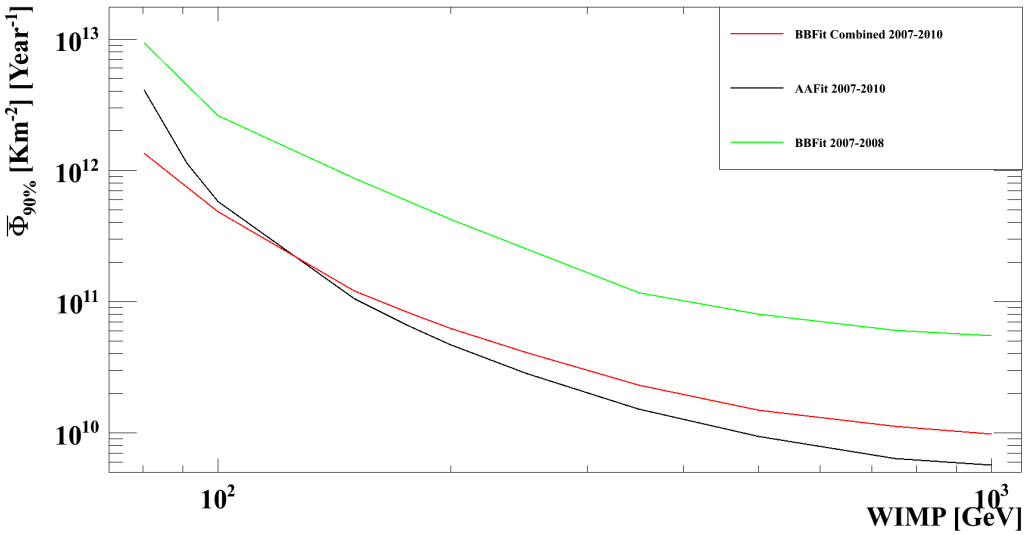

Figure 6.44: Comparison of the sensitivities set by the 2007-2008 analysis (BBFit) and 2007-2010 analysis (BBFit combined and AAFit) for the soft W^+W^- spectrum.

mass of 200 GeV and a cross-section of $2.5 \cdot 10^{-4}$pb. With the 2007-2010 analysis probed mass region is extended to 450 GeV and the lowest achieved cross-section is $6 \cdot 10^{-5}$ pb at 330 GeV GeV using the AAFit analysis. On the other hand the BBFit combined analysis clearly offers us better cross-section sensitivities below 150 GeV.

As for the spin-independent cross-section sensitivities we are just starting to probe some models. However, even as we are not expected to put significant limits on the cross-section the improvement is clear. However, these new results in spin-dependent cross-section outperforms those of Super-K presented in figure 5.32 in the low WIMP mass area (below 100 GeV) and if we add to that now between 250 GeV and 500 GeV the results also outperform those by ICECUBE.

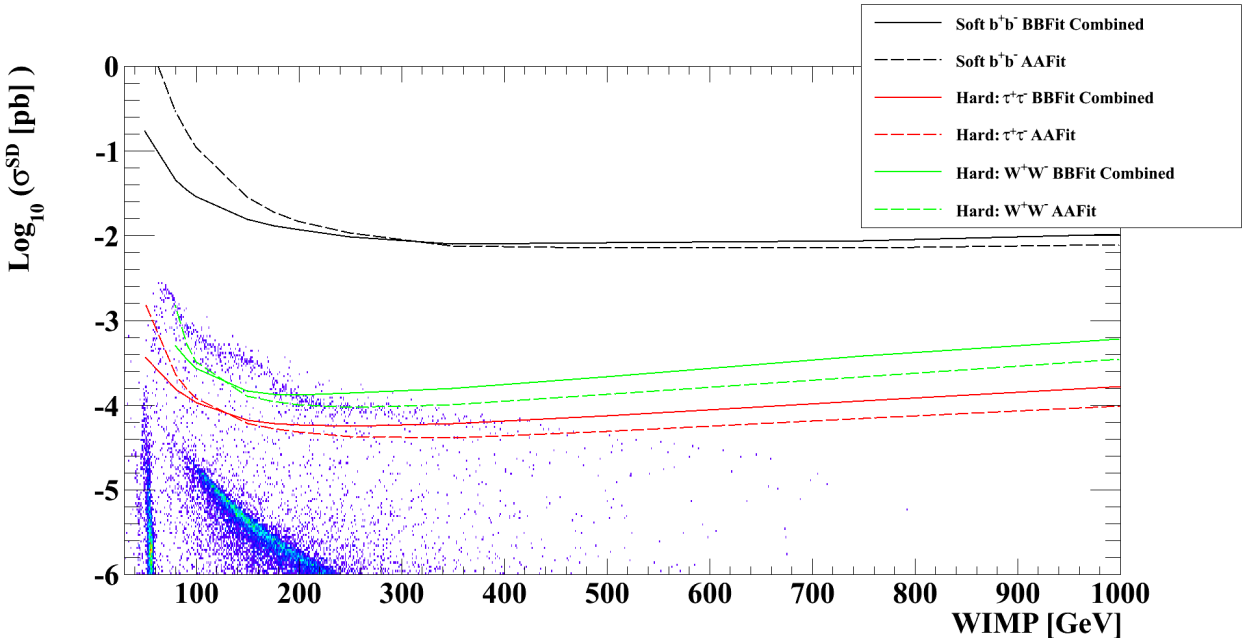

Figure 6.45: Sensitivities to spin-dependent cross-section for BBFit-combined and AAFit analyzes as a function of WIMP mass and annihilation channel.

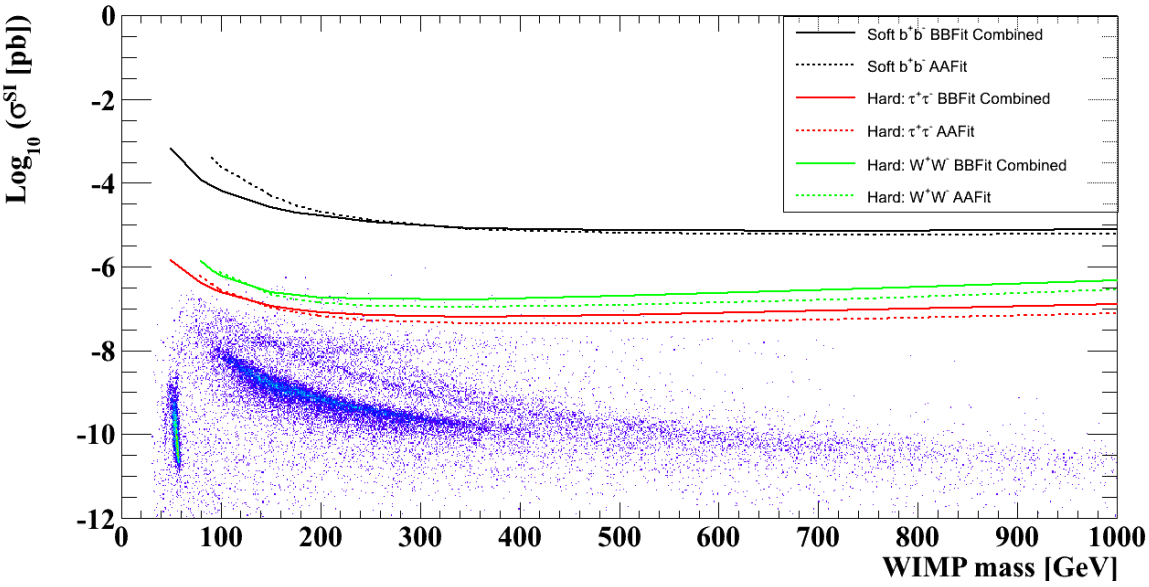

Figure 6.46: Sensitivities to spin-independent cross-section for BBFit-combined and AAFit analyzes as a function of WIMP mass and annihilation channel.

Chapter 7

Conclusions

The limits presented in figure 5.32 for the 2007-2008 data analysis are not yet competitive with other experiments (due to life-time). However, they have shown the potential to be make ANTARES competitive if we introduce improvements to the analysis. This was done with the analysis introduced in Chapter 6. We saw that by increasing the livetime of the data (a natural evolution of the analysis) we immediately gain an important factor that allows us to be competitive (BB-Fit Multi-lines analysis). Moreover, the introduction of the single-line data set showed us that we can further improve our sensitivities specially for light WIMPs. On the other hand the use of the AAFit reconstruction strategy also showed us that the sensitivities can also be improved for heavier WIMPs while sacrificing those for lighter ones. What we can conclude from this is that with the amelioration introduced in 2007-2010 analysis such as the increased livetime, extra optimization variables, and a new reconstruction strategy, can put ANTARES in a place where it is competitive with other experiments. All of this is accomplished by using a simple analysis strategy focusing on cutting on variables and counting remaining events. The cuts optimization also ignored (for computational time-scale reasons) two promising variables such as Nhit (figures 6.17 & 6.30) and $\cos(\theta)$ (figure 6.31). These two variables can be used to further discriminate the dark matter signal from the background. The problem posed by repeating the same analysis using these two extra variables, with each yielding two cuts (a minimum value and a maximum value), is that not we will be left optimizing for at least six variables which is an extremely time consuming process. A better way to fully use the effects of these two variable (and the original ones) is to do it with the help of new methods. One is use a likelihood-ratio method. Another is to use Artificial Neutral Networks (tests on the 2007-2008 analysis showed an improvement of sensitivities by 15% to 30%).
It is important to note that the work presented in this thesis shows that indirect detection is complementary to direct detection techniques and the LHC in search

for dark matter. Additionally ANTARES is still collecting data (and it will up to 2015), henceforth finding a dark matter signal remains a possibility, specially with the fact that other types of analysis can be done. Analysis such as finding signal of dark matter WIMPs annihilating in the Galactic Center, Galactic Halo, and in Dwarf galaxies.

Bibliography

[1] Volders, L. M. J. S., "Neutral hydrogen in M 33 and M 101," *Bulletin of the Astronomical Institutes of the Netherlands, Vol. 14, p.323*, 09/1959.

[2] W. K. J. Rubin, Vera C.; Ford, "Rotation of the Andromeda Nebula from a Spectroscopic Survey of Emission Regions," *Astrophysical Journal, vol. 159, p.379*, 02/1970.

[3] A. Bosma, "The distribution and kinematics of neutral hydrogen in spiral galaxies of various morphological types," *PhD Thesis, Groningen Univ*, 1978.

[4] W. K. J. T. N. Rubin, V. C.; Ford, "Rotational properties of 21 SC galaxies with a large range of luminosities and radii, from NGC 4605 /R = 4kpc/ to UGC 2885 /R = 122 kpc/," *Astrophysical Journal, Part 1, vol. 238, June 1, 1980, p. 471-487*.

[5] Van Albada, T. S.; Bahcall, J. N.; Begeman, K.; Sancisi, R., "Distribution of dark matter in the spiral galaxy NGC 3198," *Astrophysical Journal, Part 1 (ISSN 0004-637X), vol. 295, Aug. 15, 1985, p. 305-313*.

[6] A. Vikhlinin, A. Kravtsov, W. Forman, C. Jones, M. Markevitch, *et al.*, "Chandra sample of nearby relaxed galaxy clusters: Mass, gas fraction, and mass-temperature relation," *Astrophys.J.*, vol. 640, pp. 691–709, 2006.

[7] D. Walsh, R. F. Carswell & R. J, Weymann, "0957 + 561 A, B: twin quasistellar objects or gravitational lens," *Nature 279, 381-384 (31 May 1979)*.

[8] A. Taylor, S. Dye, T. J. Broadhurst, N. Benitez, and E. van Kampen, "Gravitational lens magnification and the mass of abell 1689," *astro-ph/9801158*, 1998.

[9] A. Refregier, "Weak gravitational lensing by large scale structure," *Ann.Rev.Astron.Astrophys.*, vol. 41, pp. 645–668, 2003.

[10] D. Clowe, M. Bradac, A. H. Gonzalez, M. Markevitch, S. W. Randall, *et al.*, "A direct empirical proof of the existence of dark matter," *Astrophys.J.*, vol. 648, pp. L109–L113, 2006.

[11] D. Clowe, A. Gonzalez, and M. Markevitch, "Weak lensing mass reconstruction of the interacting cluster 1E0657-558: Direct evidence for the existence of dark matter," *Astrophys.J.*, vol. 604, pp. 596–603, 2004.

[12] M. Milgrom, "A modification of the newtonian dynamics as a possible alternative to the hidden mass hypothesis," *Astrophysical Journal, Part 1 (ISSN 0004-637X), vol. 270, July 15, 1983, p. 365-370.*

[13] R. E. Faber, S. M.; Jackson, "Velocity dispersions and mass-to-light ratios for elliptical galaxies," *Astrophysical Journal*, vol. 204, pp. 668–683, 03/1976.

[14] A. Faber, S. M. & Dressler, "Radial velocities for galaxies in 11 clusters," *Astronomical Journal, Vol. 82, p. 187 - 192, 241 - 247 = Lick Obs. Bull., No. 753*.

[15] "Cosmic background explorer," *http://lambda.gsfc.nasa.gov/product/cobe/*.

[16] C. Bennett *et al.*, "The Microwave Anisotropy Probe (MAP) mission," *Astrophys.J.*, vol. 583, pp. 1–23, 2003.

[17] "The Scientific programme of planck," 2006.

[18] W. J. Percival, S. Cole, D. J. Eisenstein, R. C. Nichol, J. A. Peacock, *et al.*, "Measuring the Baryon Acoustic Oscillation scale using the SDSS and 2dFGRS," *Mon.Not.Roy.Astron.Soc.*, vol. 381, pp. 1053–1066, 2007.

[19] M. Kowalski *et al.*, "Improved Cosmological Constraints from New, Old and Combined Supernova Datasets," *Astrophys.J.*, vol. 686, pp. 749–778, 2008.

[20] M. Viel, J. Bolton, and M. Haehnelt, "Cosmological and astrophysical constraints from the Lyman-alpha forest flux probability distribution function," *arXiv:0907.2927v1*, 2009.

[21] N. Jarosik, C. Bennett, J. Dunkley, B. Gold, M. Greason, *et al.*, "Seven-Year Wilkinson Microwave Anisotropy Probe (WMAP) Observations: Sky Maps, Systematic Errors, and Basic Results," *Astrophys.J.Suppl.*, vol. 192, p. 14, 2011.

[22] S. Burles et al., "Big bang nucleosynthesis predictions for precision cosmology," *The Astrophysical Journal Letters 552, 1 (2001)*.

[23] P. T. et al. (EROS Collaboration), "Limits on the macho content of the galactic halo from the eros-2 survey of the magellanic clouds," *Astronomy & Astrophysics 469, 387 (2007)*.

[24] B. Carr, K. Kohri, Y. Sendouda, and J. Yokoyama, "New cosmological constraints on primordial black holes," *Phys.Rev.*, vol. D81, p. 104019, 2010.

[25] G. Bertone, D. Hooper, and J. Silk, "Particle dark matter: Evidence, candidates and constraints," *Phys.Rept.*, vol. 405, pp. 279–390, 2005.

[26] Springel, Volker; White, Simon D. M.; Jenkins, Adrian; Frenk, Carlos S.; Yoshida, Naoki; Gao, Liang; Navarro, Julio; Thacker, Robert; Croton, Darren; Helly, John; Peacock, John A.; Cole, Shaun; Thomas, Peter; Couchman, Hugh; Evrard, August; Colberg, Jorg; Pearce, Frazer, "Simulations of the formation, evolution and clustering of galaxies and quasars," *Nature, Volume 435, Issue 7042, pp. 629-636 (2005)*.

[27] G. Servant and T. M. Tait, "Is the lightest Kaluza-Klein particle a viable dark matter candidate?," *Nucl.Phys.*, vol. B650, pp. 391–419, 2003.

[28] T. Bringmann, "Cosmological aspects of universal extra dimensions," *PhD thesis, Stockholm University. Department of Physics. August 2005*.

[29] W. F. H. Amaldi, Ugo; de Boer, "Comparison of grand unified theories with electroweak and strong coupling constants measured at lep," *Physics Letters B, Volume 260, Issue 3-4, p. 447-455*.

[30] S. P. Martin, "A Supersymmetry primer," 1997.

[31] G. Aad *et al.*, "Observation of a new particle in the search for the Standard Model Higgs boson with the ATLAS detector at the LHC," *Phys.Lett.B*, 2012.

[32] K. S. D. N. Drukier, Andrzej K.; Freese, "Detecting cold dark-matter candidates," *Physical Review D (Particles and Fields), Volume 33, Issue 12, 15 June 1986, pp.3495-3508*.

[33] R. Lemrani, "Search for dark matter with EDELWEISS: Status and future," *Phys.Atom.Nucl.*, vol. 69, pp. 1967–1969, 2006.

[34] D. Akerib, P. Barnes, P. Brink, B. Cabrera, R. Clarke, *et al.*, "Design and performance of a modular low-radioactivity readout system for cryogenic detectors in the CDMS experiment," *Nucl.Instrum.Meth.*, vol. A591, pp. 476–489, 2008.

[35] E. Aprile *et al.*, "First Dark Matter Results from the XENON100 Experiment," *Phys.Rev.Lett.*, vol. 105, p. 131302, 2010.

[36] E. Behnke *et al.*, "Improved Spin-Dependent WIMP Limits from a Bubble Chamber," *Science*, vol. 319, pp. 933–936, 2008.

[37] T. Morlat, F. Giuliani, M. F. da Costa, T. Girard, A. Ramos, *et al.*, "First Results from a Prototype CF-3-I SIMPLE Dark Matter Search Detector," 2007.

[38] B. Ahmed, G. Alner, H. Araujo, J. Barton, A. Bewick, *et al.*, "The NAIAD experiment for WIMP searches at Boulby mine and recent results," *Astropart.Phys.*, vol. 19, pp. 691–702, 2003.

[39] K. P. Modak and D. Majumdar, "Gamma Ray and Neutrino Flux from Annihilation of Neutralino Dark Matter at Galactic Halo Region in mAMSB Model," 2012.

[40] R. Bernabei *et al.*, "First results from DAMA/LIBRA and the combined results with DAMA/NaI," *Eur.Phys.J.*, vol. C56, pp. 333–355, 2008.

[41] E. Aprile *et al.*, "Dark Matter Results from 100 Live Days of XENON100 Data," *Phys.Rev.Lett.*, vol. 107, p. 131302, 2011.

[42] B. Allanach, "Softsusy: a program for calculating supersymmetric spectra," *Comput. Phys. Commun.*, vol. 143, p. 305, 2002.

[43] P. Gondolo, J. Edsjo, P. Ullio, L. Bergstrom, and M. Schelke, "Darksusy: Computing supersymmetric dark matter properties numerically," *JCAP*, vol. 07, p. 008, 2004.

[44] S. Heinemeyer, W. Hollik, and G. Weiglein, "The masses of the neutral cp-even higgs bosons in the mssm: Accurate analysis at the two-loop level," *Eur. Phys. J.*, vol. C29, p. 343, 1999.

[45] S. Heinemeyer, W. Hollik, and G. Weiglein, "Feynhiggs: a program for the calculation of the masses of the neutral cp-even higgs bosons in the mssm," *Comput. Phys. Commun.*, vol. 124, p. 76, 2000.

[46] G. Debrassi, S. Heinemeyer, W. Hollik, P. Slavich, and G. Weiglein, "Towards high-precision predictions for the mssm higgs sector," *Eur. Phys. J.*, vol. C28, p. 133, 2003.

[47] M. Frank, T. Hahn, S. Heinemeyer, W. Hollik, H. Rzehak, and G. Weiglein, "The higgs boson masses and mixings of the complex mssm in the feynman-diagrammatic approach," *JHEP*, vol. 02, p. 047, 2007.

[48] L. Roszkowski, R. Ruiz de Austri, R. Trotta, and J. Silk, "On prospects for dark matter indirect detection in the constrained mssm," 2007.

[49] L. Roszkowski, R. R. de Austri, and R. Trotta, "On the detectability of the cmssm light higgs boson at the tevatron," *JHEP*, vol. 04, p. 084, 2007.

[50] R. Trotta, R. R. de Austri, and L. Roszkowski, "Prospects for direct dark matter detection in the constrained mssm," *New Astron. Rev.*, vol. 51, pp. 316–320, 2007.

[51] R. R. de Austri, R. Trotta, and L. Roszkowski, "A markov chain monte carlo analysis of the cmssm," *JHEP*, vol. 05, p. 002, 2006.

[52] F. Feroz, M. P. Hobson, and M. Bridges, "MultiNest: an efficient and robust Bayesian inference tool for cosmology and particle physics," 2008.

[53] R. T. et al, "The impact of priors and observables on parameter inferences in the constrained mssm," 2008.

[54] S. Piccardi, "The PAMELA experiment," 1999.

[55] J. Beatty, A. Bhattacharyya, C. Bower, S. Coutu, M. DuVernois, *et al.*, "New measurement of the cosmic-ray positron fraction from 5 to 15-GeV," *Phys.Rev.Lett.*, vol. 93, p. 241102, 2004.

[56] M. Aguilar *et al.*, "Cosmic-ray positron fraction measurement from 1 to 30-GeV with AMS-01," *Phys.Lett.*, vol. B646, pp. 145–154, 2007.

[57] A. A. Abdo *et al.*, "Measurement of the Cosmic Ray e+ plus e- spectrum from 20 GeV to 1 TeV with the Fermi Large Area Telescope," *Phys.Rev.Lett.*, vol. 102, p. 181101, 2009.

[58] J. Chang, J. Adams, H. Ahn, G. Bashindzhagyan, M. Christl, *et al.*, "An excess of cosmic ray electrons at energies of 300-800 GeV," *Nature*, vol. 456, pp. 362–365, 2008.

[59] L. Goodenough and D. Hooper, "Possible Evidence For Dark Matter Annihilation In The Inner Milky Way From The Fermi Gamma Ray Space Telescope," 2009.

[60] C. Weniger, "A Tentative Gamma-Ray Line from Dark Matter Annihilation at the Fermi Large Area Telescope," *JCAP*, vol. 1208, p. 007, 2012.

[61] E. Tempel, A. Hektor, and M. Raidal, "Fermi 130 GeV gamma-ray excess and dark matter annihilation in sub-haloes and in the Galactic centre," 2012.

[62] F. Aharonian *et al.*, "Discovery of very-high-energy gamma-rays from the galactic centre ridge," *Nature*, vol. 439, pp. 695–698, 2006.

[63] D. Elsaesser and K. Mannheim, "MAGIC and the search for signatures of supersymmetric dark matter," *New Astron.Rev.*, vol. 49, pp. 297–301, 2005.

[64] R. G. Wagner, "Indirect Dark Matter Searches with VERITAS," 2009.

[65] M. Vivier, "Indirect searches for dark matter annihilations toward dwarf spheroidal galaxies with VERITAS," 2011.

[66] T. Bringmann, "Antiproton and Radio Constraints on the Dark Matter Interpretation of the Fermi Gamma Ray Observations of the Galactic Center," 2009.

[67] M. Ageron, J. Aguilar, I. Al Samarai, A. Albert, F. Ameli, *et al.*, "ANTARES: the first undersea neutrino telescope," *Nucl.Instrum.Meth.*, vol. A656, pp. 11–38, 2011.

[68] R. Abbasi *et al.*, "The IceCube Neutrino Observatory IV: Searches for Dark Matter and Exotic Particles," 2011.

[69] R. Abbasi *et al.*, "Multi-year search for dark matter annihilations in the Sun with the AMANDA-II and IceCube detectors," *Phys.Rev.*, vol. D85, p. 042002, 2012.

[70] S. Desai *et al.*, "Search for dark matter WIMPs using upward through-going muons in Super-Kamiokande," *Phys.Rev.*, vol. D70, p. 083523, 2004.

[71] R. Abbasi *et al.*, "Search for Dark Matter from the Galactic Halo with the IceCube Neutrino Observatory," *Phys.Rev.*, vol. D84, p. 022004, 2011.

[72] G. J. et al., "Supersymmetric dark matter," *Physics Reports 267, 195*.

[73] D. L.-B. F. J. Kerr, "Review of galactic constants," *Royal Astronomical Society, Monthly Notices 221, 1023 (1986)*.

[74] C. Hettlage, K. Mannheim, and J. G. Learned, "The Sun as a high-energy neutrino source," *Astropart.Phys.*, vol. 13, pp. 45–50, 2000.

[75] G. Wikstrom and J. Edsjo, "Limits on the WIMP-nucleon scattering cross-section from neutrino telescopes," *JCAP*, vol. 0904, p. 009, 2009.

[76] J. Edsjo, "Wimpsim web tool," *http://www.physto.se/~edsjo/wimpsim/scripts.html*.

[77] T. Sjostrand, S. Mrenna, and P. Z. Skands, "PYTHIA 6.4 Physics and Manual," *JHEP*, vol. 0605, p. 026, 2006.

[78] S. Fukuda *et al.*, "Determination of solar neutrino oscillation parameters using 1496 days of Super-Kamiokande I data," *Phys.Lett.*, vol. B539, pp. 179–187, 2002.

[79] Y. Ashie *et al.*, "Evidence for an oscillatory signature in atmospheric neutrino oscillation," *Phys.Rev.Lett.*, vol. 93, p. 101801, 2004.

[80] Q. Ahmad *et al.*, "Direct evidence for neutrino flavor transformation from neutral current interactions in the Sudbury Neutrino Observatory," *Phys.Rev.Lett.*, vol. 89, p. 011301, 2002.

[81] E. Aliu *et al.*, "Evidence for muon neutrino oscillation in an accelerator-based experiment," *Phys.Rev.Lett.*, vol. 94, p. 081802, 2005.

[82] Yao, W.-M. et al., "Review of Particle Physics," *Journal of Physics G*, vol. 33, pp. 1+, 2006.

[83] L. Wolfenstein, "Neutrino oscillations in matter," *Physical Review D 17, 2369 (1978)*.

[84] A. Y. S. S. P. Mikheyev, "Resonance amplification of oscillations in matter and spectroscopy of solar neutrinos," *Soviet Journal of Nuclear Physics 42,913 (1985)*.

[85] M. Maltoni, T. Schwetz, M. Tortola, and J. Valle, "Status of global fits to neutrino oscillations," *New J.Phys.*, vol. 6, p. 122, 2004.

[86] M. Blennow, J. Edsjo, and T. Ohlsson, "Neutrinos from WIMP annihilations using a full three-flavor Monte Carlo," *JCAP*, vol. 0801, p. 021, 2008.

[87] D. J. Griffiths, "Introduction to Electrodynamics," *PHI learning*.

[88] D. J. Bailey, "Dark Matter, the deep ocean and neutrinos from heaven: Monte Carlo tools and analysis methods for understanding the ANTARES experiment and predicting its sensitivity to Dark Matter," *Ph.D. thesis, wolfson college, University of Oxford*.

[89] P. Amram *et al.*, "The ANTARES optical module," *Nucl.Instrum.Meth.*, vol. A484, pp. 369–383, 2002.

[90] J. Aguilar *et al.*, "AMADEUS - The Acoustic Neutrino Detection Test System of the ANTARES Deep-Sea Neutrino Telescope," 2010.

[91] M. Ardid, "Positioning system of the ANTARES neutrino telescope," *Nucl.Instrum.Meth.*, vol. A602, pp. 174–176, 2009.

[92] J. Aguilar *et al.*, "Time Calibration of the ANTARES Neutrino Telescope," *Astropart.Phys.*, vol. 34, pp. 539–549, 2011.

[93] M. Ageron *et al.*, "The ANTARES Optical Beacon System," *Nucl.Instrum.Meth.*, vol. A578, pp. 498–509, 2007.

[94] J. Aguilar *et al.*, "The data acquisition system for the ANTARES Neutrino Telescope," *Nucl.Instrum.Meth.*, vol. A570, pp. 107–116, 2007.

[95] P. Amram *et al.*, "Background light in potential sites for the ANTARES undersea neutrino telescope," *Astropart.Phys.*, vol. 13, pp. 127–136, 2000.

[96] D. Zaborov, "Coincidence analysis in ANTARES: Potassium-40 and muons," *Phys.Atom.Nucl.*, vol. 72, pp. 1537–1542, 2009.

[97] J. Aguilar *et al.*, "A fast algorithm for muon track reconstruction and its application to the ANTARES neutrino telescope," *Astropart.Phys.*, vol. 34, pp. 652–662, 2011.

[98] A. Heijboer, "Reconstruction of Atmospheric Neutrinos in Antares," *arXiv:0908.0816*, 2009.

[99] A. Labbate et al., "Genhen v6: ANTARES neutrino generator extension to all neutrino flavors and inclusion of propagation through the earth," *ANTARES internal note, ANTARES-SOFT-2004-010*.

[100] J. Brunner, "Cherenkov Light from HE Electromagnetic and Hadronic Showers," *ANTARES internal note, ANTARES-SOFT-2002-015*.

[101] G. Carminati, M. Bazzotti, S. Biagi, S. Cecchini, T. Chiarusi, *et al.*, "MUPAGE: a fast atmospheric MUon GEnerator for neutrino telescopes based on PArametric formulas," 2009.

[102] D. Heck and J. Knapp, "Forschungszentrum Karlsruhe Report FZKA 6097 (1998)," *http://www-ik.fzk.de/corsika*.

[103] G. J. Feldman and R. D. Cousins, "A Unified approach to the classical statistical analysis of small signals," *Phys.Rev.*, vol. D57, pp. 3873–3889, 1998.

[104] S. Loucatos, "Systematics of the indirect DM search," *ANTARES-PHYS-2011-015, Internal Note*.

[105] e. a. C.Bogazzi, "Point Source Search with 2007 and 2008 data," *ANTARES-PHYS-2010-008, Internal Note*.

[106] G. Halladjian, "Search for high energy neutrinos from point sources with ANTARES," *Dec2010, Ph.D thesis*.

[107] J. C. et al., "Discovery and Upper Limits in Search for Exotic Physics with Neutrino Telescopes," *Phys. Rev. D 67 (2003) 012002*.

[108] G. Lim, "Searching for Dark Matter with the Antares Neutrino Telescope," *Ph.D. thesis, Faculteit der Natuurwetenschappen, Wiskunde en Informatica.*

[109] T. Tanaka *et al.*, "An Indirect Search for WIMPs in the Sun using 3109.6 days of upward-going muons in Super-Kamiokande," *Astrophys.J.*, vol. 742, p. 78, 2011.

[110] C. Riviere, "Run-by-run Monte Carlo simulation for ANTARES: v2," *ANTARES internal note, ANTARES-PHYS-2012-001*.

[111] Adrian-Martinez, S. and others, "Measurement of Atmospheric Neutrino Oscillations with the ANTARES Neutrino Telescope," *Phys.Lett.*, vol. B714, pp. 224–230, 2012.